Strain relaxation in InGaN/GaN herostructures

Quantong Li

To cite this version:

Quantong Li. Strain relaxation in InGaN/GaN herostructures. Theoretical and/or physical chemistry. Normandie Université, 2018. English. NNT : 2018NORMC204 . tel-01775272

HAL Id: tel-01775272

https://theses.hal.science/tel-01775272

Submitted on 24 Apr 2018

THESE

Pour obtenir le diplôme de doctorat

Spécialité *CHIMIE*

Préparée au sein de l'ENSICAEN et l'UNICAEN

Strain relaxation in InGaN/GaN heterostuctures

Présentée et soutenue par

Quantong LI

Thèse soutenue publiquement le 20/03/2018 devant le jury composé de		
Madame Sabine LAY	Directeur de Recherche CNRS Université Grenoble Alpes	Rapporteur
Monsieur Ludovic DESPLANQUE	Maitre de Conférences HDR Université Lille 1	Rapporteur
Monsieur Olivier PEREZ	Directeur de Recherche CNRS ENSICAEN	Examinateur
Monsieur Piero GAMARRA	Ingénieur, Thales research and technology	Examinateur
Monsieur Jun CHEN	Professeur des Universités Université de Caen Normandie	Co-Directeur de thèse
Monsieur Pierre RUTERANA	Directeur de Recherche CNRS ENSICAEN	Directeur de thèse

Thèse dirigée par Dr. RUTERANA Pierre et Prof. CHEN Jun, Laboratoire CIMAP

Acknowledgements

The work has been carried out at CIMAP laboratory along these three years. Behind this achievement, there are a great many people, who gave me help, support and inspiration so that make it possible and therefore I take this opportunity to express my special gratitude to all of you for contributing to my thesis.

I first express deep gratitude to my supervisor Dr. Pierre Ruterana for giving me the opportunity to carry out my PhD Research work and for leading me into the field of transmission electron microscopy and defects. Over the past three years, he has given me guidance, support, and encouragements for my research. I express greatest thanks to Prof. Jun Chen, my co-supervisor for encouraging me to spend more time in my research. It is a pleasure for me to thank Dr. Sabine Lay and Dr. Ludovic Desplanque for having accepted to review my manuscript. In the same vein, my acknowledgements go also to Dr. Olivier Perez and Dr. Piero Gamarra for having accepted to judge my work as members of the examination committee.

I am very much grateful to Dr. Albert Minj for rekindling my interests in crystallography, semiconductor physics, nanotechnology and proving that learning can be fun, and he has always been a source of encouragement.

Finally, my gratitude goes to my colleagues in PM2E TEM, Marie-Pierre Chauvat for teaching and helping me with sample preparation and Hichem Ben Ammar for all the good discussions in research and life.

To all my friends in Caen for making my life colorful all along these three years.

And above all to my parents, for endless love and support.

During this work, I benefited from a financial grant provided by the China Scholarship Council

Quantong LI

CONTENTS

Résumé I

Introduction VII

Chapter 1 1

The III-nitride semiconductors 1

- 1. 1 Introduction 2
- 1. 2 Properties of group III nitrides 4
  - 1. 2. 1 Crystalline structure 4
  - 1. 2. 2 Crystal polarity 7
  - 1. 2. 3 Dislocations 8
- 1. 3 Group III nitrides epitaxy 10
  - 1. 3. 1 Substrates for group III nitrides 11
  - 1. 3. 2 Sapphire substrate 12
  - 1. 3. 3 SiC 12
  - 1. 3. 4 Si 13
- 1. 4 Slip systems in hexagonal materials 13
- 1. 5 Applications of group III nitrides 15
  - 1. 5. 1 Optical applications 16
  - 1. 5. 2 Electronic applications 18

Chapter 2 25

Experimental techniques 25

2. 1 Metal Organic Vapor Phase Epitaxy (MOVPE) 26

2. 2 Molecular Beam Epitaxy (MBE) 28

2. 3 The investigated samples 29

2. 4 Microscopy techniques 30

2. 4. 1 Atomic Force Microscopy (AFM) 30

2. 4. 2 Transmission Electron Microscopy (TEM) 33

2. 5 TEM specimen preparation 39

2. 5. 1 Shaping the samples 40

2. 5. 2 Thickness reduction by mechanical polishing 41

2. 5. 3 Ion polishing 42

Chapter 3 45

Metal Organic Vapor Phase Epitaxy of InGaN/GaN heterostructures 45

3. 1 Introduction 46

3. 2 The samples 47

3. 3 Structural analysis of MOVPE layers 48

3. 3. 1 The surface morphology by AFM 48

3. 3. 2 Microstructural analysis 52

3.4 Summary and conclusions 60

Chapter 4............65

Plasma Assisted Molecular Beam Epitaxy of In-rich InGaN/GaN heterostructures............65

4. 1 Introduction............66

4. 2 PAMBE growth of InGaN layers............67

4. 3 The surface morphology............68

4. 4 The microstructure analysis............70

4. 5 Discussion and Conclusion............78

Chapter 5............81

The interface dislocations in the InGaN/GaN heterostructures............81

5. 1 Introduction............82

5. 2 Low misfit (In < 10%)............83

5. 3 Intermediate (In ~ 13%)............84

5. 4 Medium misfit (In ≥ 18%)............86

5. 5 High misfit (In ~ 30%)............86

5. 6 Discussion............88

5. 7 Summary............92

Chapter 6............95

Conclusions and perspectives............95

Résumé

Les semi-conducteurs nitrures (AlN, GaN, InN) et leurs alliages font l'objet d'intenses recherches depuis bientôt 30 ans. Les propriétés physiques des composés binaires et des alliages de nitrures du groupe III les rendent tout à fait indispensables dans les domaines de l'électronique et de l'optoélectronique. Par exemple, les alliages InGaN sont utilisés pour fabriquer des diodes électroluminescentes, des diodes laser, des transistors et des cellules solaires. Cependant, en raison de la décomposition spinodale susceptible de se produire dans l'alliage InGaN, des phénomènes induits chimiquement, tels que la séparation des phases, la mise en ordre à longue distance ont été rapportés, cela conduit à des couches affichant des microstructures avec défauts complexes. L'autre défi avec l'hétérostructure InGaN/GaN est la relaxation de la contrainte à l'hétérointerface. En raison du décalage paramétrique entre la couche épitaxiale InGaN et le GaN, de nombreux défauts sont présents dans la couche InGaN, par exemple des défauts en V, des dislocations et des fautes d'empilement, mais aussi des dislocations dans l'interface pendant la croissance. Comme les défauts se forment en fonction de la composition en l'indium et de l'épaisseur de la couche, le but de ce travail a été de comprendre les mécanismes de relaxation des contraintes présentes afin d'aider à la croissance des couches de meilleure qualité cristalline pour la possible fabrication de dispositifs performants.

Cette thèse porte sur une étude détaillée de la morphologie de surface et de la microstructure des couches InGaN/GaN obtenues par épitaxie en phase vapeur aux organométalliques (EPVOM) et aussi par l'épitaxie aux jets moléculaires assistée par plasma (EJM) en utilisant la microscopie à force atomique (AFM) et ensuite la microscopie électronique à transmission (MET). Le but est de mettre en évidence la relation entre le type de défaut et la relaxation des contraintes dans les hétérostructures InGaN/GaN.

Ce manuscrit se décline en 6 chapitres:

Chapitre 1 : Les semi-conducteurs nitrures de métaux du groupe III

Dans le chapitre 1, nous présentons les semi-conducteurs de nitrure, leur structure cristalline, la polarité, les défauts cristallins, les substrats de croissance des nitrures du groupe III, la relaxation de la contrainte aux interfaces ainsi que leurs applications dans l'électronique et l'optoélectronique.

Chapitre 2 :Techniques expérimentales

Au cours du chapitre 2, nous avons décrit les techniques de croissance EPVOM et EJM utilisées pour croître les couches analysées au cours de ce travail de thèse. Les échantillons d'InGaN/GaN/saphir ont été obtenus par EPVOM grâce à nos collaborations avec AIXTRON et l'École Polytechnique Fédérale de Lausanne, Suisse. Les couches EJM ont été fabriquées à l'INAC, Grenoble. Les informations quantitatives sur la morphologie de surface des échantillons en termes de rugosité ont été obtenues par AFM. Dans cette étude, la partie la plus importante de MET a été réalisée sur un microscope JEOL JEM-2010 fonctionnant à une tension d'accélération de 200 kV en utilisant une source thermoionique d'hexaborure de lanthane (L_aB_6). Un MET à haute résolution de 200 kV avec une résolution maximale de 0.19 nm (C_s = 1.4 mm pour HAADF) a également été utilisé dans notre étude pour l'imagerie à haute résolution et l'analyse locale par spectroscopie aux rayons X (EDS). La diffraction X a été aussi utilisée dans cette étude pour une analyse de la qualité cristalline des couches principalement riches en indium obtenues par EPVOM.

Chapitre 3 : Couches d'InGaN par EPVOM

Ce chapitre est focalisé sur la détermination du rôle de la concentration d'indium que nous avons fait varier entre 4% et 100% sur la relaxation des contraintes. Nous avons étudié la morphologie de surface et la microstructure des couches InGaN obtenues par MOVPE en utilisant d'abord l'AFM et ensuite la MET. Nous avons trouvé que la morphologie de surface dépend fortement de la composition en In. Pour $x < 0.13$, les surfaces présentent des marches atomiques, avec une très faible densité de défauts en V. Entre $0.13 \leq x \leq 0.18$, les surfaces contiennent un réseau plus ou moins hexagonal de défauts linéaires dont la densité croît avec la concentration en indium. Au-delà d'une composition de 25%, le mode de croissance 3D devient prédominant. Par MET, les résultats montrent qu'il n'y a pas de dislocations dans les hétérostructures InGaN/GaN pour la plus faible concentration en In. Pour $0.13 \leq x \leq 0.25$, les dislocations traversantes et les défauts en V sont systématiquement présents dans InGaN, les dislocations de décalage paramétrique en grande densité sont observées lorsque la concentration en In devient supérieure à 0.18. On peut de plus avoir formation des défauts d'empilement dans les couches pour In = 25% en étroite interaction avec les défauts en V. Au-delà de 40% en In, il y a une forte croissance 3D, et une dégradation très rapide de la qualité cristalline des couches d'InGaN jusqu'à contenir une forte porosité.

Chapitre 4 : Couches d'InGaN obtenues par EJM

Le principal avantage de la croissance par EJM est que nous avons pu avoir des couches de InGaN épaisses (jusqu'à 500 nm) ayant une faible rugosité de surface. Nous avons donc pu nous attacher à étudier en détail les mécanismes qui peuvent intervenir pour la relaxation de la contrainte, en effet, le seul paramètre qui était censé varier d'un échantillon à l'autre était l'épaisseur, la composition nominale ayant été voulu constante à 30% d'indium. Ainsi, à l'épaisseur la plus faible de la couche d'InGaN, il n'y pas de formation de défauts, ni dans la couche, ni dans l'interface, elle est donc contrainte sur le GaN. Cependant, dès 30 nm d'épaisseur, la couche montre une formation de fautes d'empilement au niveau de l'interface, avec certaines qui peuvent aller jusqu'en surface. Lorsque l'épaisseur de la couche est supérieure à 80 nm, les dislocations de décalage paramétrique sont déjà en forte densité dans l'interface, des demi-boucles de dislocation partent alors de la surface vers l'interface, et la couche contient de nombreuses fautes d'empilement. A l'épaisseur la plus grande étudiée (500 nm), l'interface InGaN contient les dislocations de décalage paramétrique, qui, bien que très nombreuses, ne sont pas suffisantes pour relâcher toute la contrainte. En effet, de très fortes densités de dislocations traversantes sont présentes ainsi que des demi-boucles de dislocations qui descendent de plus en plus auprès de l'interface. De plus, la couche de surface est très perturbée : les séquences de l'empilement hexagonal ont été perdues, et la composition en surface s'est enrichie en indium par rapport au volume.

Chapitre 5 Formation de dislocations dans l'interface InGaN/GaN

Dans nos échantillons, la composition en In varie de 4 à 100%, et donc le décalage paramétrique lors de la croissance sur (0001) GaN est compris entre 1 et 11.3%. Dans ces matériaux hexagonaux, la relaxation de la contrainte d'interface durant la croissance épitaxiale n'est pas bien connue et on s'attend à ce qu'elle se déroule de manière différente de ce qui se passe dans le système cubique. En particulier, la croissance le long de la direction [0001] limite le glissement des dislocations sur seulement quelques familles de plans atomiques. Fait intéressant, ce travail permet de montrer que cette relaxation suit plusieurs chemins. En effet, lorsque la composition en indium est de l'ordre de 10%, aux épaisseurs des couches que nous avons étudiées, on s'attendrait déjà à la formation de dislocations de décalage paramétrique. Cependant, notre étude montre que ce sont des dislocations vis qui sont présentes à l'interface InGaN/GaN. De plus, en dessous de 18% de composition d'indium, ces dislocations vis coexistent avec des dislocations coins de décalage paramétrique. Outre les dislocations de rattrapage du décalage paramétrique, d'autres mécanismes ont été mis en évidence pour la relaxation des contraintes. En effet, au-dessus d'une composition d'indium supérieure à 25%, de nombreux phénomènes se produisent simultanément : (1) formation des dislocations coins à l'interface; (2) enrichissement en indium en surface par rapport au volume de la couche d'InGaN;

(3) disparition de la séquence hexagonale vers la surface conduisant à un empilement aléatoire; (4) croissance 3D pouvant même conduire à des couches poreuses lorsque la composition en indium est comprise entre 40% et 85%.

Chapitre 6 Conclusion générale et perspective

Ce chapitre résume les principaux résultats obtenus et discutés dans les chapitres 3 à 5 en soulignant les contributions originales que l'étude comparative de matériaux obtenus par deux méthodes de croissance différentes nous ont permis de faire sur une connaissance des mécanismes de relaxation des hétérostructures InGaN/GaN. L'analyse des couches obtenues par EJM jusqu'à de fortes épaisseurs nous a montré pour la première fois la forte contribution des dislocations mixtes '***a*** + ***c***' dans la formation des dislocations ***a*** coins de décalage paramétrique. Les analyses en section plane du chapitre 5 montrent aussi la présence de dislocations ***a*** vis aux faibles teneurs en indium. Ces deux résultats très intéressants demandent un travail encore plus approfondi pour bien comprendre les mécanismes sous-jacents. En effet, si le réseau de dislocations vis apparait d'abord, comment se transforme-t-il en dislocations coins qui seules peuvent aider à relâcher la contrainte due au décalage paramétrique. En ce qui concerne le glissement des dislocations mixtes, nos analyses menées en section plane ne permettent pas d'indiquer ce que devient la composante ***c*** lorsque la demi boucle atteint l'interface InGaN/GaN pour donner naissance à la dislocation ***a*** coin, il faut donc poursuivre les travaux pour pouvoir conclure.

Introduction

The nitride semiconductors (AlN, GaN, InN) and their alloys have become a subject of intense investigation during the last 30 years. Their properties make them exclusive for applications in the fields of electronics and optoelectronics, for instance, InGaN-based alloys are used to fabricate light-emitting diodes (LEDs), laser diodes (LDs), transistors as well as solar cells. These applications are based on heterostructures of these compounds and their ternary alloys. Still, the fabrication of optimized devices remains a challenge due to many yet non-solved issues. Indeed, the three compounds exhibit substantial differences in physical properties such as lattice and thermal mismatch, growth temperature, etc. This is at the origin of possible spinodal decomposition of some of the ternary alloys which leads to chemically induced phenomena, such as phase separation, ordering and compositional pulling, which have been reported depending on the growth conditions. The other challenge for the InGaN/GaN heterostructures, where the lattice mismatch between GaN and InN is up to 11%, is the relaxation of the strain at the heterointerface. As a consequence, high densities of defects can be generated in the InGaN layers, depending on the growth conditions, for example, V-shaped defects, dislocations, stacking faults, with the inherent subsequent degradation of the devices. At the heterointerface, it is expected that misfit dislocations form depending on the indium composition and the layer thickness. The objective of this work has been to determine the strain relaxation mechanisms of the InGaN alloys grown on GaN in order to assist in the growth of best crystalline quality layers for device applications.

This thesis relates a detailed research on the surface morphology and the strain relaxation of the InGaN layers on GaN templates grown by Metalorganic Vapour Phase Epitaxy (MOVPE) as well as Plasma Assisted Molecular Beam Epitaxy (PAMBE), the purpose is to point out the relationship between the defect type and the strain relaxation.

Chapter 1 presents a brief overview of the properties and applications of group III nitride semiconductors.

Chapter 2 gives a description of the growth, the preparation as well as the characterization techniques used for investigating the samples.

Chapter 3 details the results of our systematical study of the surface morphology and the cross-sectional microstructure of the InGaN layers grown by MOVPE using Atomic Force Microscopy (AFM) as well as Transmission Electron Microscopy (TEM).

Chapter 4 focuses on investigating the influence of varying layer thickness on strain relaxation. We analyzed the surface morphology and the cross-sectional microstructure of the InGaN layers grown by PAMBE respectively using AFM and TEM. The main results obtained in this study allow determining the dominant strain relaxation processed in InGaN layers grown on GaN, they include composition fluctuation, composition pulling at large thicknesses and the hexagonal stacking disruption during the growth.

Chapter 5 reports our detailed analysis of the relaxation of the heterostructures as a function of indium composition by the generation of misfit dislocations. It is shown that the formation of dislocations could start at an indium concentration of around 10% with the generation of screw dislocations, by 13%, we point out a mixed network of edge and screw dislocations up to 17%, and past 18%, only a dense network of ***a*** type edge dislocations are generated with their lines along <$10\bar{1}0$> directions.

Chapter 6 summarizes the general conclusion of this work and discusses some of the open questions.

Chapter 1

The III-nitride semiconductors

1. 1 Introduction

Semiconductor-based devices have been successfully used in microelectronics, optoelectronics as well as chemical sensors. The nitride semiconductors, aluminum nitride (AlN), gallium nitride (GaN), and indium nitride (InN) as well as their alloys have become a subject of intense research during the last 30 years. For one material family, the have unique properties i.e., a wide direct bandgap, strong chemical bonds that make them suitable for the production of optoelectronic devices (both emitters and detectors) and high-power/temperature electronic devices, as have been reviewed many times in the literature [1-7].

It is now more than 100 years that the investigation of these materials started: the first synthesis of AlN, GaN as well as InN was reported in 1907 [8], 1910 [9], and 1932 [10], respectively. As these compounds do not exist as bulk materials, they need to be synthetized on various substrates. Although GaN was first synthesized a long time ago, the interest in this group of semiconductors was limited because of the extreme difficulties of growing them in single-crystalline form. This latter fact was attributed to their thermodynamic properties, for example, in the case of GaN, the melting temperature of 2500 °C is quite high and is accompanied by a high equilibrium nitrogen pressure of ~45000 bar. In the period 1965-1975, Jacques Pankove and his students did pioneering work in growing as well as characterizing GaN [11]. Therefore, it took many decades to attain significant progress for the growth of GaN epitaxial layers on sapphire substrates using Hydride Vapor Phase Epitaxy (HVPE) [12], Metalorganic Vapor Phase Epitaxy (MOVPE) [13] or Molecular Beam Epitaxy (MBE) [14].

The breakthrough of nitrides took place in 1989 thanks to the Japanese scientists Amano, Akasaki, and Nakamura, who overcame the issues of growth and p-type doping [15, 16] which initiated the advent of violet to yellow light emitting diodes (LEDs) [17-19], laser diodes (LDs)

[18], UV LEDs [19, 20]. They used the MOVPE technique to grow nitride layers on sapphire substrates. They also used a post-growth activation process to achieve p-type material. From this time onwards, the development of this material was strongly driven by the industrial demand for LEDs and lasers. At present, blue and green LEDs as well as blue LDs are commercially available [21]. This was mainly because of their direct energy gaps covering the whole visible spectrum as well as a large part of the ultraviolet (UV) spectral region [22], extending from InN (0.7 ± 0.05 eV, near infrared) [23], to GaN (3.4 eV, mid UV), finally to AlN (6.2 eV, deep UV) [24]. Specifically, nitrides are suitable for such applications as surface acoustic wave devices [25], UV detectors [26, 27], Bragg reflectors [28], waveguides, UV and visible LEDs [29-31] as well as LDs [32] for digital data read-write applications.

From then, GaN and its alloys with AlN and InN have become the second important family of semiconductor materials just after silicon because they should allow the design and production of devices with unique electronic and optoelectronic properties [33-37]. The development of indium gallium nitride (InGaN) is one of the emerging field of research in III-nitrides [38]. The direct band gap of $In_xGa_{1-x}N$ can be designed to emit light all over the visible spectrum depending on the indium content (x) of the film. InGaN-based alloys are therefore used to fabricate LEDs, LDs [39, 40] as well as solar cells [41, 42]. InGaN alloys are excellent candidates for the light-absorption layers in solar cell applications due to their high-energy radiation resistance [41], and because InGaN alloys across the range of indium compositions absorb light over the whole solar spectrum in a multijunction solar cell [43]. On the other hand, however, the development of GaN-based technology was, and still is, strongly limited by difficulties in obtaining large, high quality GaN crystals. This is a direct consequence of thermodynamic properties of GaN [44] (and also AlN [45]). An additional effort has been made towards High Electron Mobility Transistors (HEMTs) based on nitride heterostructures [46], and intense research has been dedicated towards the application of group III nitride materials in high power, microwave frequency electronic devices [47, 48]. GaN's wide band gap, large dielectric breakdown field, and fortuitously good electron transport properties [49-51] as well as good thermal conductivity are trademarks of high-power/temperature electronic devices [52]. Several groups have reported on the superior performance of GaN-based modulation-doped FETs (MODFETs) on silicon carbide (SiC) and sapphire substrates with respect to competing materials, especially at X band and higher frequencies [53-56]. Applications of high-power GaN-based MODFETs include amplifiers operative at high power levels, high temperatures as well as in unfriendly environments such as radars, missiles, satellites, and in low-cost compact amplifiers for wire-less base stations.

1. 2 Properties of group III nitrides

1. 2. 1 Crystalline structure

The three (Al, Ga, In) nitride compounds and their alloys are most stable in the wurtzite structure Figure 1.1 [57, 58], which consists of two hexagonal close packed sublattices of group III metal and nitrogen atoms, respectively, the corresponding space group is $P6_3mc$. The two sublattices should be ideally related by a translation u = 3c/8 along [0001] ***c***-axis and each atom is surrounded by four atoms of the other kind at the edges of a tetrahedron.

In a hexagonal system, the notation for the four indices (h k i l) is assigned to the three base vectors $\boldsymbol{a_1}$, $\boldsymbol{a_2}$, $\boldsymbol{a_3}$ and ***c*** respectively. The third index i is defined as, i = – (h + k) and the three $\boldsymbol{a_i}$ vectors lie at a 120° angle.

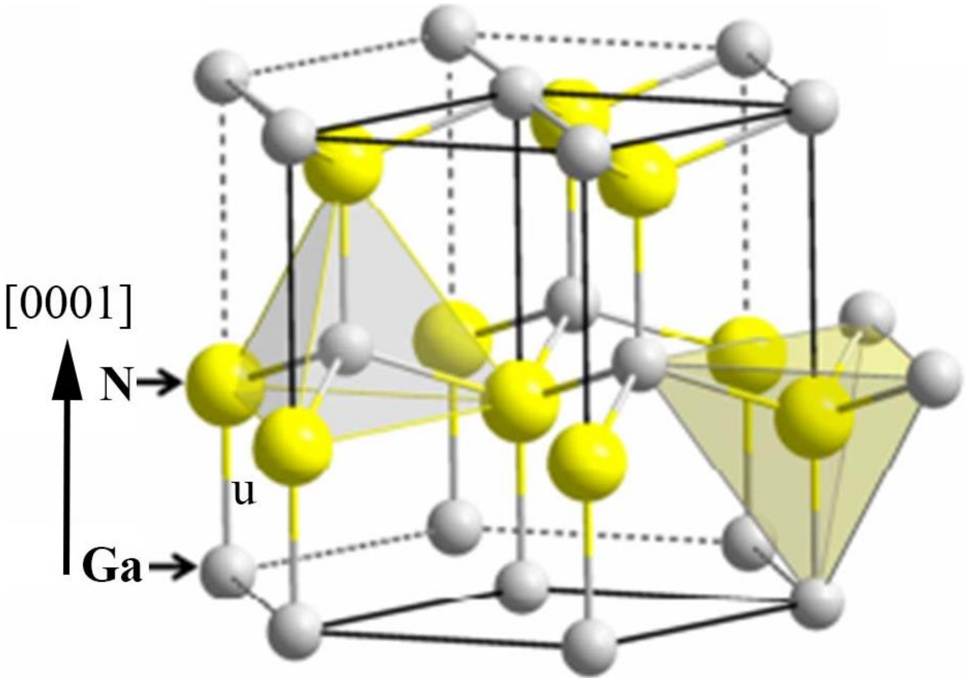

Figure 1.1 Illustration of atomic distribution in wurtzite lattice.

As can be seen in Figure 1.2, the band gap of group III nitride semiconductors can be adjusted in a wide range from near infrared (IR) to deep UV spectral region.

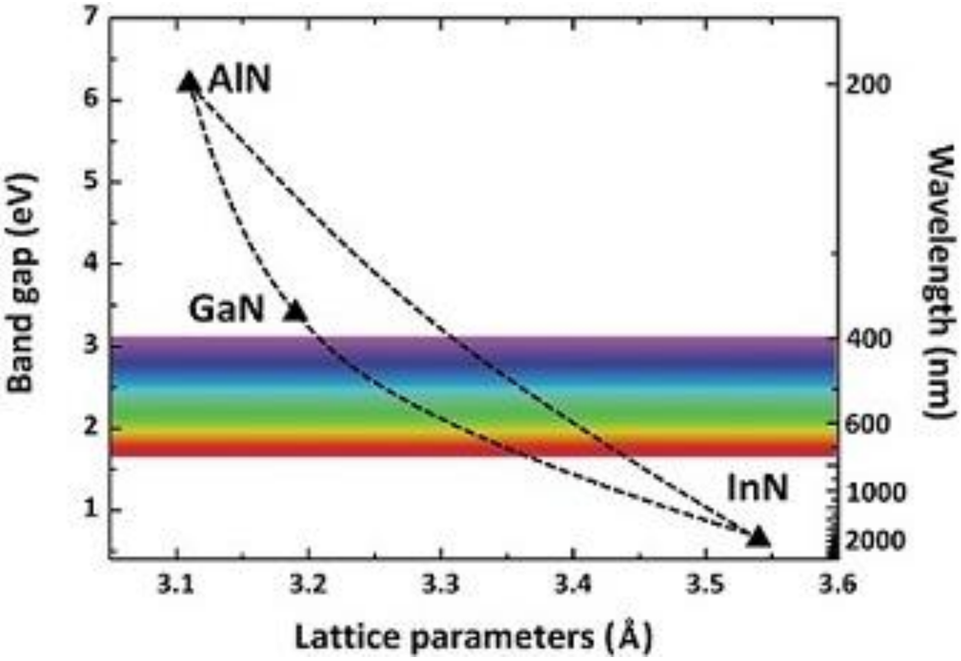

Figure 1.2 Energy band gap and wavelength versus lattice parameters.

In the first approximation which is called “the Vegard law”, many properties (lattice parameters, band gaps, etc.) may be deduced from those of the end binary compounds. For instance, the band gap of a ternary alloy (e. g. $A_xB_{1-x}N$) may be deduced as:

$$a_{AB} = xa_A + (1 - x)a_B \quad (1.\ 1)$$

As the materials are grown as thin layers on substrates such as sapphire, SiC, Si, etc., residual strain build up as due to lattice, and thermal mismatch. The lattice mismatch is defined as:

$$\varepsilon = (a_s - a_l) / a_s \quad (1.\ 2)$$

where a_s is the lattice parameter of the substrate, and a_l is the corresponding one for the epitaxial layer. As can be seen in table 1.1, which exhibits the lattice parameters, important differences exist for the three nitride binary compounds in the wurtzite structure.

Table 1.1 Lattice parameters and mismatch of bulk InN, GaN and AlN at room temperature [58].

Parameters (Å)	**InN**	**GaN**	**AlN**	**Heterostructure**	**Lattice mismatch along *a* parameter**
a	3.54	3.189	3.112	InN/GaN	11 %
c	5.705	5.185	4.982	GaN/AlN	2.3 %
u	0.377	0.376	0.380	InN/AlN	13.7%

The other properties of wurtzite AlN, GaN and InN (electronic, thermal and optical, etc.) are also quite different (Table 1.2). In many instances, the growth of their heterostructures as well as alloys may not lead to good quality layers due to such large mismatch.

Table 1.2 Physical properties of III nitride materials [59-62].

Parameter	**AlN**	**GaN**	**InN**
Mass density (gcm^{-3})	3.23	6.15	6.81
Thermal conductivity (W/cm K)	2.85	2.06-2.1	0.8
Thermal expansion (X 10^{-6} K^{-1})	$\Delta a/a$ =4.2 $\Delta c/c$ =5.3	$\Delta a/a$ =5.59 $\Delta c/c$ =3.17	$\Delta a/a$ =3 $\Delta c/c$ =4
Refractive index	2.15 ± 0.05	2.33	2.8-3.05
Dielectric constant	€$_0$ = 8.5 ± 0.2 €$_\infty$ = 4.68 - 4.84	€$_0$ = 9.5 €$_\infty$ = 5.35	€$_0$ = 15.3 €$_\infty$ = 8.4
Electron effective mass (m$_e$)	0.48	0.2	0.06
Electron concentration (cm^{-3})	$< 10^{16}$	$\sim 10^{17}$	10^{16}- 10^{20}
Electron mobility (cm^{2}V^{-1}S^{-1})	300(Theoretical) 426(Experimental)	1000(Theoretical) 900(Experimental)	4400(Theoretical) 3980(Experimental)
Peak drift velocity (X 10^7 cms^{-1})	1.7	2.9	4.2

1. 2. 2 Crystal polarity

The group III nitrides are not centrosymmetric crystal structures, as a result, the two crystallographic directions [0001] and [000-1] are not equivalent. Conventionally, the [0001] polarity is defined by the direction of the vector pointing from the metal (Al/Ga/In) atom to nitrogen (N) along the <0001> axis as shown in Figure 1.3. An epitaxial layer grown along this direction is called metal polar and the material grown in the opposite direction is called nitrogen polar. The two different polar materials possess distinct properties in terms of surface morphology, chemical reactivity, thermal stability and even the growth conditions. For instance, metal-polar surfaces have been reported to present a higher chemically stability than nitrogen polar surfaces [63, 64].

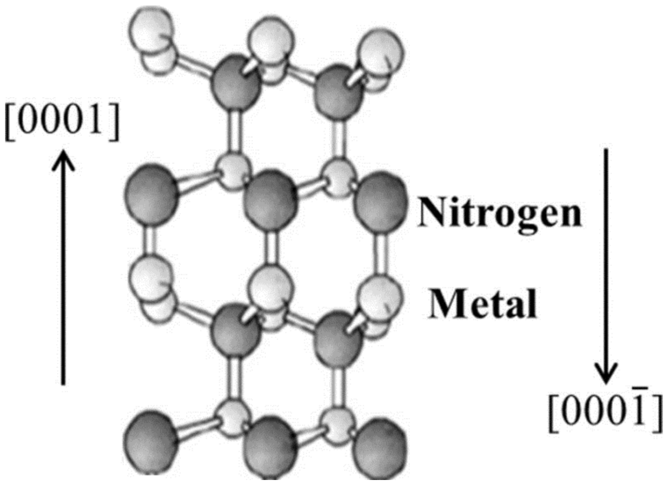

Figure 1.3 Metal polar surface of wurtzite nitrides are mainly terminated by metallic atoms [65].

The selection between the two polarities during the epitaxial growth of this Group III nitride system i.e. metal polar or N-polar, depends on the used substrate material and the growth conditions [66]. The polarity of the films can be probed by various techniques like wet chemical etching, electron microscopic techniques such as Convergent Beam Electron Diffraction (CBED), Co-Axial Impact Collision Ion Scattering Spectroscopy (CAICISS). More recently hydrogen irradiation has also been proposed to be effectively sensitive to the polarity [63].

1. 2. 3 Dislocations

Dislocations are linear defects which are some of the typical imperfections in the crystalline structure. They are generated to relax the stress which may arise during the growth and any other mechanical deformation in order to decrease the global energy of the material system. If formed during an epitaxial growth, they originate from the difference of lattice parameters and thermal expansion coefficients of the substrate and the epilayer. These linear defects are characterized by their Burgers vector $\boldsymbol{b}$ and dislocation line $\boldsymbol{u}$. Depending on their density inside the layers used for the fabrication of electronic components, they strongly affect the device performance [67, 68].

In group III nitride epitaxy, the most common dislocations are the threading Dislocations (TDs) [69, 70] which are generated at the interface with the substrate and propagate up to the surface of the layer, through the active part of the component. A dislocation can either be perfect or partial. A dislocation is said to be perfect, when its Burgers vector corresponds to an entire translation of the lattice; it is partial when the Burgers vector is a fraction of a translation of the lattice. In nitride layers grown along ***c***, the main defects are TDs (shown in Table 1.3), which form as edge, screw or mixed type and are distinguished by the angle made between the Burgers vector and the dislocation line.

(1) For a pure **edge** dislocation, the dislocation line is perpendicular to Burgers vector ***b***. A schematic diagram of atomic planes can be used to illustrate lattice defects such as dislocations. The "extra half-plane" concept of an edge type dislocation is shown in Figure 1.4.

(2) For a **screw** dislocation, the dislocation line is parallel to the Burgers vector as shown in Figure 1.4.

(3) For a **mixed type** dislocation, there is no defined angular relationship between the dislocation line and the Burgers vector.

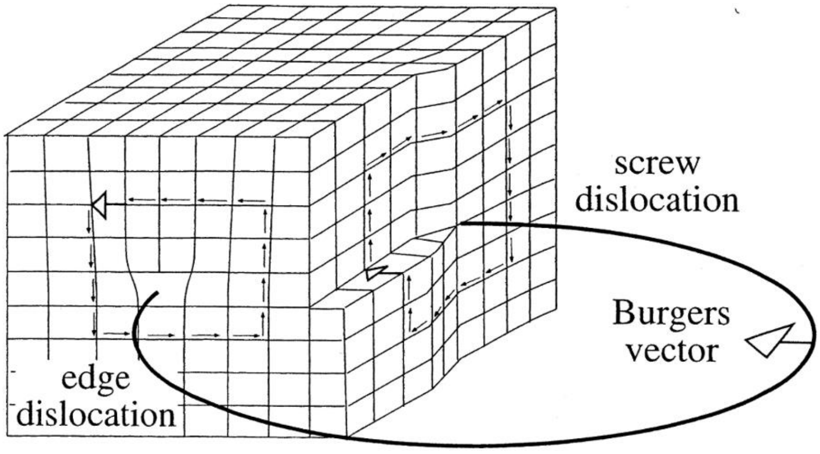

Figure 1.4 A schematic diagram showing, screw and edge dislocation [71].

Table 1.3 Perfect and partial dislocations in group III nitride epitaxial layers grown along the [0001] direction [68, 69].

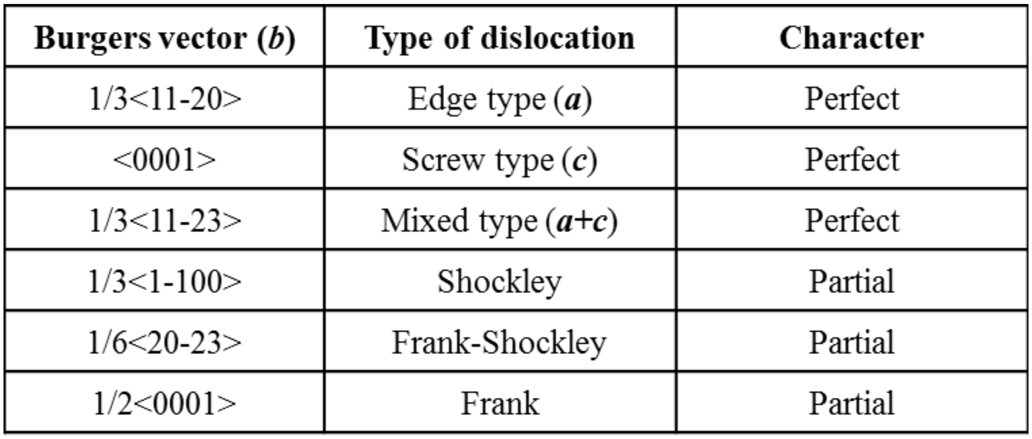

Burgers vector (*b*)	**Type of dislocation**	**Character**
1/3<11-20>	Edge type (***a***)	Perfect
<0001>	Screw type (***c***)	Perfect
1/3<11-23>	Mixed type (***a+c***)	Perfect
1/3<1-100>	Shockley	Partial
1/6<20-23>	Frank-Shockley	Partial
1/2<0001>	Frank	Partial

1. 3 Group III nitrides epitaxy

The common growth techniques for III nitrides are Hydride Vapor Phase epitaxy (HVPE), Metal organic Vapor Phase epitaxy (MOVPE), Molecular beam epitaxy (MBE). Among them MOVPE and MBE are the most used for device processing and they were employed to grow the samples which are investigated in this work.

The quality of epitaxial layers depends upon the growth technique, the epitaxial growth mode (homoepitaxial or heteroepitaxial), the substrate used and the growth conditions. The choice of growth technique depends on the desired structure and applications. For example, in case of industrial production, MBE had less success for nitrides than MOVPE. For group III nitrides growth, although bulk GaN and AlN are available, the small size and high cost prevent their wide usage. Therefore, due to the current lack of affordable bulk nitride substrates, group III nitrides are grown by heteroepitaxy. Lattice and thermal mismatch between epitaxial layers and substrates have long been the major challenge in obtaining high quality devices in the III-Nitride material system. The properties of the most commonly used substrates for group III nitrides are listed in Table 1.4, which indicates a large lattice and thermal mismatch between the III-nitrides and the substrates. Because of this mismatch the growth of good quality epilayers is challenging.

Table 1.4 Properties of substrates for III-Nitride growth [61, 62, 72].

Substrate	**Crystal symmetry**	**Lattice constant Å**		**Lattice mismatch, Δ*a*/*a* (%)**		**Thermal expansion coefficient ($10^{-6}K^{-1}$)**	
		A	*c*	GaN	InN	Δ*a*/*a*	Δc/*c*
α-Al_2O_3	Hexagonal	4.765	12.982	~16	~30	5.0	9.03
SiC	Hexagonal	3.0806	15.1173	~3.5	~14.8	4.3	4.7
Si	Cubic	a= b= c=5.431		~21	~8	3.59	

1. 3. 1 Substrates for group III nitrides

For epitaxial growth, one of the major issues is to select the suitable substrate. Generally, close matched substrates are used to reduce the film stress and dislocations in the epitaxial films. There are many factors which contribute to select the substrates for group III nitride epitaxy, and no single material possesses all of the desired qualities. The foremost important factors are the lattice parameters and the thermal expansion coefficients of the substrate and of the epitaxial film which should closely match. Furthermore, the substrates must be chemically and mechanically stable at high temperatures. A substrate should be easily available in large wafer size at relatively low cost in order to make production-scale devices. A high thermal conducting substrate increases device lifetime and allows devices to operate at higher power densities. For optoelectronic purposes, the substrate should have a wide band gap and a high refractive index, so that the photons generated in the active layers of the film are not absorbed by the substrate. A number of substrates have been used for Group III nitrides epitaxy and a complete review was reported by Liu et al. [61].

1. 3. 2 Sapphire substrate

Sapphire is the most extensively used substrate for growth of the III-nitrides despite of its large structural and thermal mismatch with GaN and InN (shown in Table 1.4). Indeed sapphire is easily available up to inches in diameter at relatively low cost. Sapphire substrates are transparent and stable at high temperatures. In general, the quality of the films grown directly (i.e., without the buffer layer) on any plane of sapphire is poor. Obtaining a good quality of nitride epilayers necessitates the nitridation of sapphire substrates and an insertion of a low temperature intermediate buffer layer. Furthermore, the optical transparency of sapphire is beneficial in back-illuminated detectors and LEDs for lack of absorption. The main drawback of sapphire, as a substrate, is the low thermal conductivity, which causes heat management, an important concern for high current density devices [73].

1. 3. 3 SiC

Extensive work has been done on the growth of III-nitrides on SiC substrates [74, 75]. SiC has several advantages over sapphire for nitride epitaxy, which includes a smaller lattice mismatch and higher thermal conductivity. Additionally, SiC has good electrical conductivity which allows to make electrical contacts to the backside of the substrates and thereby simplifies the device structure compared to sapphire substrates. Large good quality SiC substrates are commercially available. Low temperature GaN or AlN buffer layers are also deposited on the SiC substrates before growing the nitrides. The stress developed in the films grown on SiC is smaller than that grown on sapphire, because of less lattice mismatch. SiC is also a polar material which facilitates the growth of single polarity nitrides.

1. 3. 4 Si

The epitaxy on Si substrate has also been investigated due mostly to the additional possibility provided for the integration of III nitride devices with other Si based electronics. Therefore, a considerable work has been done on the growth of group III nitrides on Si substrate. The major attractive points of Si as a substrate includes high quality, low cost, availability of large size, good electrical and thermal conductivity. Although the crystal quality of GaN grown on Si is still poorer than that on sapphire and SiC, research on this is in great progress. A low temperature buffer layer of AlN is usually grown on Si before the growth of the main epilayer to avoid the formation of Si_xN_y. The growth of a polar epilayer on nonpolar substrate is more complicated due to the formation of additional defects, such as inversion domains.

1. 4 Slip systems in hexagonal materials

Table 1.5 Effective shear stress factor, cos λ, for different slip systems [76].

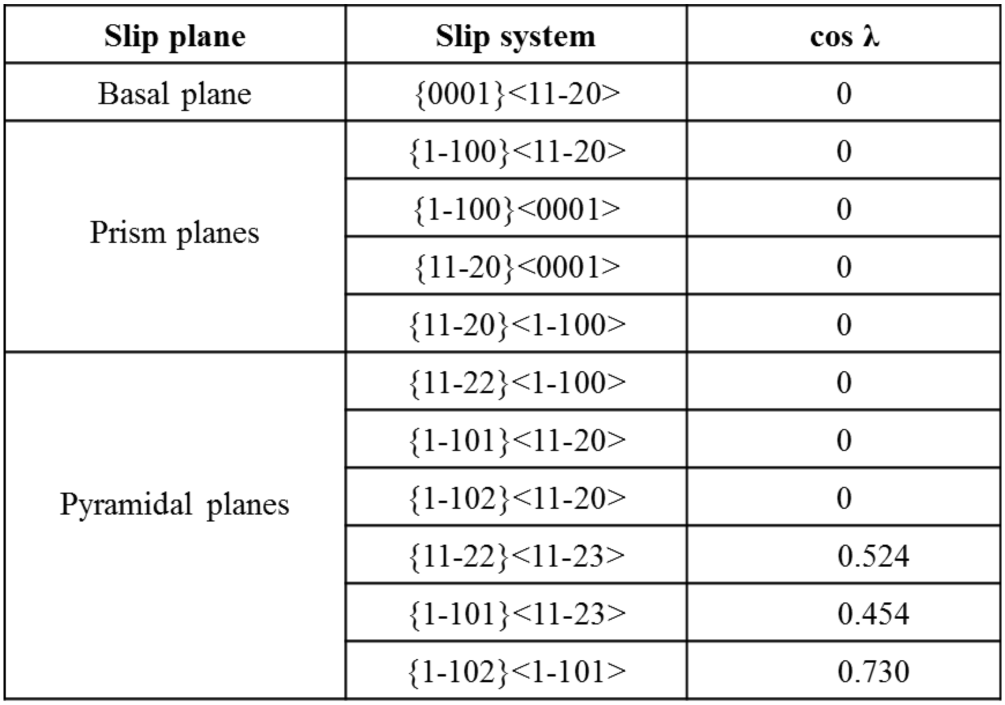

Slip plane	Slip system	cos λ
Basal plane	{0001}<11-20>	0
Prism planes	{1-100}<11-20>	0
	{1-100}<0001>	0
	{11-20}<0001>	0
	{11-20}<1-100>	0
Pyramidal planes	{11-22}<1-100>	0
	{1-101}<11-20>	0
	{1-102}<11-20>	0
	{11-22}<11-23>	0.524
	{1-101}<11-23>	0.454
	{1-102}<1-101>	0.730

In the particular geometry of growth along the [0001] direction which is used in this study, the primary slip systems involving the basal and prismatic planes, as well as some pyramidal planes (Figure 1.5) cannot be operating to the glide of the dislocations as the resolved shear factor is 0, see Table 1.5 [76]. Thus, only three of the pyramidal slip systems may have a contribution because of the corresponding shear stress factor cos λ ≠ 0, namely, {1-102}<1-101>, {11-22}<11-23> and {1-101}<11-23>.

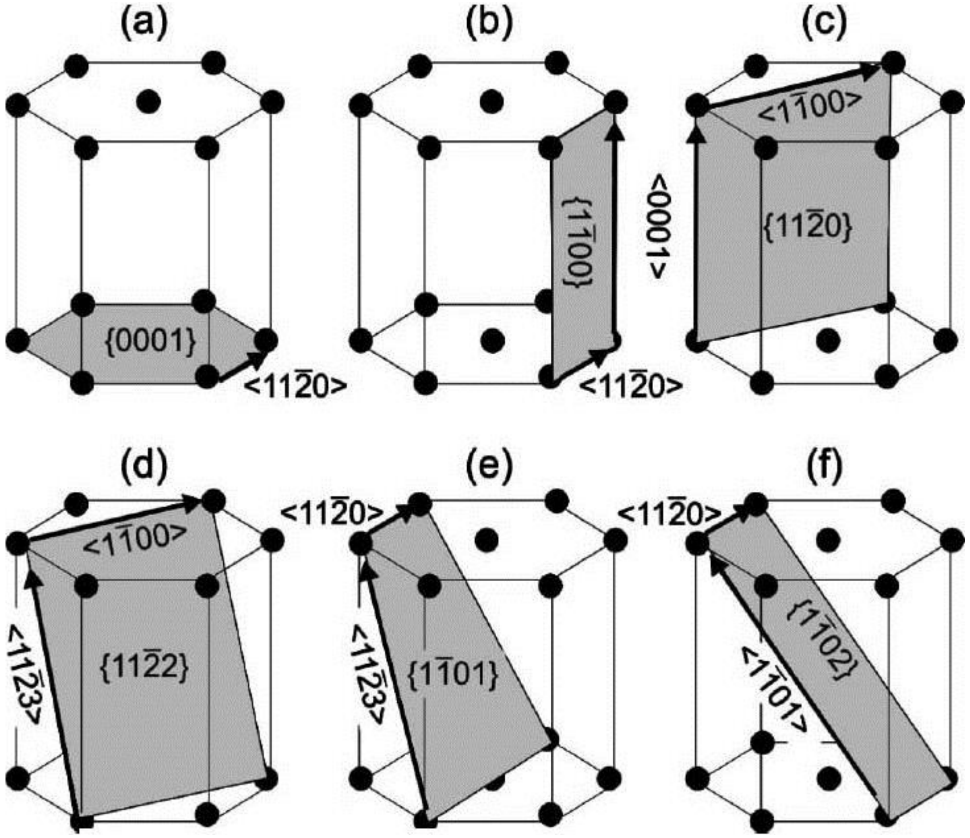

Figure 1.5 Slip systems in a hexagonal lattice. Slip planes and directions are as indicated [76].

Using the Matthews-Blakeslee model [77] and including the contribution of Peierls force [78], the net force for the glide of the dislocations was calculated for $In_{0.1}Ga_{0.9}N$ as shown in Table 1.6 [76]. As can be seen, It only two slip systems {11-22}<11-23> and {1-101}<11-23> are able to contribute to the formation of misfit dislocations during the epitaxial growth along the

[0001] direction, and most probably the {11-22}<11-23> system should be predominant. However, in these materials, it has been reported that other mechanisms such as formation of islands, pits and even undulations may occur and dominate the misfit strain relaxation process, thus hindering the formation of misfit dislocations [79]. This is also in agreement with the work of Srinivasan et al. [76] who showed that the relaxation of the InGaN layers by formation of misfit dislocations was easy only by epitaxy on GaN templates of extremely high crystalline quality obtained by epitaxial lateral overgrowth. Otherwise, the preexistence of high densities of threading dislocations in more conventional templates leads to elastic relaxation of the InGaN layers by formation of pinholes.

Table 1.6 Forces involved in the formation of misfit dislocations for the active slip systems in the case of growth of $In_{0.10}Ga_{0.90}N$ on GaN [76].

Slip system	**Force due to lattice mismatch F_a (nN)**	**Force due to Line tension F_l (nN)**	**Peierls force F_p (nN)**	**Net force F_{net} (nN)**
{11-22}<11-23>	634	92	44	499
{1-101}<11-23>	549	88	127	334
{1-102}<1-101>	1099	137	1947	0

1. 5 Applications of group III nitrides

The physical properties of group III nitride binary compounds and alloys make them exclusive for applications in the fields of electronics and optoelectronics. The quest for these applications has led to extensive research work on these materials during the last two decades. The re-evaluation of InN bandgap from 1.89 to 0.65 eV has broadened the spectrum of these applications.

1. 5. 1 Optical applications

The research aims at bringing LEDs as the next generation of light sources for general illumination, from homes to commercial applications. In this field, research on group III nitride semiconductors is realizing breakthroughs in efficiency and performance in terms of successful launching of nitride LEDs and LDs. This solid state lighting technology has the potential to cut the world lighting energy usage by 20% and could contribute significantly to climate change solutions [80].

1. 5. 1. 1 LED applications

Of group III (Al, Ga, In) N system, InN plays a major role in empowering the fabrication of high efficient LEDs by widening the spectral region with the tuning of indium composition as shown in Figure 1.6.

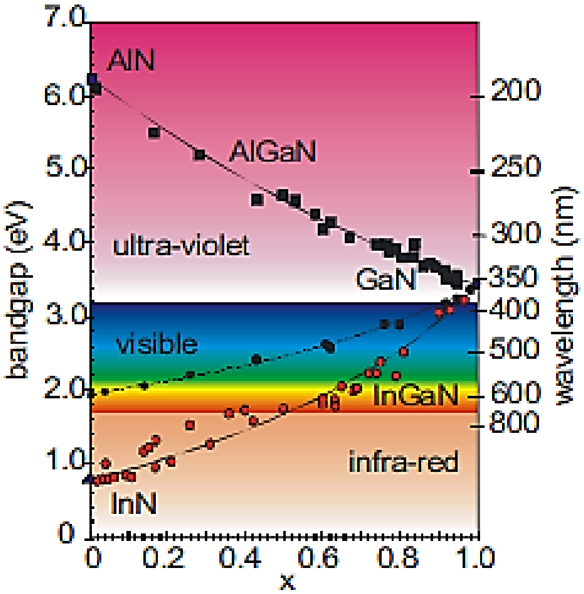

Figure 1.6 Bandgap of III nitrides as a function of In molar fraction. The solid and dashed lines were obtained using best-fit to the band gaps [81].

In other words the group III nitrides spans from near IR to deep UV region. The research on nitride based LEDs was kindled by the advent of blue/green LED based on InGaN heterostructure grown on sapphire substrate [82]. Thereafter the research in this system was reinforced towards the investigation for red LEDs with indium rich InGaN heterostructures and white LEDs which have been developed by coating blue GaN LED with phosphors [83].

1. 5. 1. 2 Laser applications

Subsequently, the fabrication of high quality materials paved the way for the realization of lasers which can operate at wavelengths from UV to green. Indeed, the blue ray disc technology has replaced the traditional DVDs as the blue LDs can allow five times higher storage capacity.

1. 5. 1. 3 Emitters and detectors

Towards the smallest wavelengths, the nitrides (Al, Ga) N binaries possess the potential for fabrication of UV emitters and detectors. UV emitters can be used in various applications such as material identification, forensic location, disinfection and material processing. They find application in UV sensing such as automobile engine combustion, high temperature flame, environmental monitoring, solar blind detectors, as well as missile plume detection, etc. The other significant application of III nitride semiconductors is for the fabrication of quantum infrared detectors. Photoconductors are the most common type of quantum infrared detectors which can be realized by nitride semiconductors. Finally, the narrow band gap of InN and its alloying with GaN makes it most adequate for photovoltaic applications. Indeed, the InGaN ternary system can be tuned to absorb the entire visible range of solar radiation and this could result in high efficiency solar cells.

1. 5. 2 Electronic applications

The unique properties of InN such as small effective mass, high electron mobilities, and high peak electron velocities make InN promising for electronic devices. InN is of great interest for realization of high speed, high performance, and high frequency devices due to its inherent unique properties. InAlN can be a good candidate for high power, high temperature microwave applications because of its higher breakdown voltages. InN is also ideal for terahertz applications.

References

[1] H. Morkoç, Nitride Semiconductors and Devices (Springer, Heidelberg, 1999).

[2] S. N. Mohammad, and H.Morkoç, Prog. Quantum. Electron. 20, 361 (1996).

[3] S. N. Mohammad, A. Salvador, and H. Morkoç, Proc. IEEE 83, 1306 (1995).

[4] H. Morkoç, S. Strite, G. B. Gao, M. E. Lin, B. Sverdlov, and M. Burns, J. Appl. Phys. 76, 1363 (1994).

[5] S. T. Strite, and H. Morkoç, J. Vac. Sci. Technol. B 10, 1237 (1992).

[6] O. Ambacher, J. Phys. D: Appl. Phys. 31, 2653, (1998).

[7] S. J. Pearton, J. C. Zolper, R. J. Shul, and F. Ren, J. Appl. Phys. 86, 1 (1999).

[8] F. Fichter, Z. Anorg. Chem. 54, 322 (1907).

[9] F. Fichter, and F. Schroter, Berichte der Deutschen Chemischen Gesellschaft, 43, 1465 (1910).

[10] V. C. Johnson, J. B. Parsons, and M. C. Crew, J. Phys. Chem. 36, 2588 (1932).

[11] J. Pankove., Optical Processes in Semiconductors (Prentice-Hall, Englewood Cliffs, NJ), (1971).

[12] H. P. Maruska, and J. J. Tietjen, Appl. Phys. Lett. 15, 327 (1969).

[13] H. M. Manasevit, F. M. Erdmann, and W. I. Simpson, J. Electrochem. Soc. 118, 1864 (1971).

[14] S. Yoshida, S. Misawa, and A. Itoh, Appl. Phys. Lett. 26, 461 (1975).

[15] H. Amano, M. Kito, K. Hiramatsu, and I. Akasaki, Jpn. J. Appl. Phys. 28, L2112 (1989).

[16] S. Nakamura, T. Mukai, M. Senoh, and N. Iwasa, Jpn. J. Appl. Phys. 31, L139 (1992).

[17] S. Nakamura, M. Senoh, and T. Mukai, Appl. Phys. Lett. 62, 2390 (1993).

[18] S. Nakamura, M. Senoh, S. Nagahama, N. Iwasa, T. Yamada, T. Mukai, T. Matsushita, Y. Sugimoto, and H. Hiyoku, Appl. Phys. Lett. 70, 868 (1997).

[19] A. Yasan, R. McClintock, K. Mayes, S. R. Darvish, H. Zhang, P. Kung, M. Razeghi, S. K. Lee, and J. Y. Han, Appl. Phys. Lett. 81, 2151 (2002).

[20] A. Yasan, R. McClintock, K. Mayes, D. Shiell, L. Gautero, S. R. Darvish, P. Kung, and M. Razeghi, Appl. Phys. Lett. 83, 4701 (2003).

[21] S. Nakamura, and G. Fasol, The blue laser diode (Springer-Verlag Berlin, 1997).

[22] S. N. Mohammad, and H. Morkoç, Prog. Quant. Electr. 20, 361 (1996).

[23] K. M. Yu, Z. Liliental-Weber, W. Walukiewicz, W. Shan, J. W. Ager III, S. X. Li, R. E. Jones, E. E. Haller, H. Lu, and W. J. Schaff, Appl. Phys. Lett. 86, 071910 (2005).

[24] S. C. Jain, M. Willander, J. Narayan, and R. V. Overstraeten, J. Appl. Phys. 87, 965 (2000).

[25] M. T. Duffy, C. C. Wang, G. D. O’Clock, S. H. McFarlane III, and P. J. Zanzucchi, J. Electron. Mater. 2, 359 (1973).

[26] M. Razeghi, and A. Rogalski, J. Appl. Phys. 79, 7433 (1996).

[27] G. Y. Xu, A. Salvador, W. Kim, Z. Fan, C. Lu, H. Tang, H. Morkoç, G. Smith, M. Estes, B. Goldenberg, W. Yang, and S. Krishnankutty, Appl. Phys. Lett. 71, 2154 (1997).

[28] I. J. Fritz, and T. J. Drummond, Electron. Lett. 31, 68 (1995).

[29] S. Nakamura, T. Mukai, and M. Senoh, Appl. Phys. Lett. 64, 1687 (1994).

[30] For a review see: H. Morkoç, and S. N. Mohammad, Sci. Mag. 267, 51-55 (1995).

[31] For a revew see: H. Morkoç, and S. N. Mohammad, Light Emitting Diodes, in Wiley Encyclopedia of Electrical Engineering and Electronics Engineering, J. Webster (ed.) (John Wiley and sons, New York 1999).

[32] S. Nakamura, M. Senoh, N. Nagahama, N. Iwara, T. Yamada, T. Matsushita, H. Kiyoku, Y. Sugimoto, T. Kozaki, H. Umemoto, M. Sano, and K. Chocho, Jpn. J. Appl. Phys. 38, L1578 (1997).

[33] S. Nakamura, T. Mukai, and M. Senoh, Appl. Phys. Lett., 64, 1687 (1994).

[34] F. A. Ponce, and D. P. Bour, Nature, 386, 351 (1997).

[35] J. Wu, W. Walukiewicz, and K. M. Yu et al., J. Appl. Phys., 94, 6477 (2003).

[36] O. Jani, I. Ferguson, C. Honsberg, and S. Kurtz, Appl. Phys. Lett., 91, 132117 (2007).

[37] S. Nakamura, S. Pearton, and G. Fasol, Emission Mecha-nisms of LEDs and LDs, The blue laser diode (Springer, Berlin, 2000), p. 279.

[38] J. Wu, J. Appl. Phys. 106, 011101 (2009).

[39] S. Nakamura, T. Mukai, and M. Senoh, Appl. Phys. Lett. 64, 1687 (1994).

[40] F. A. Ponce, and D. P. Bour, Nature 386, 351 (1997).

[41] J. Wu, W. Walukiewicz, K. M. Yu, W. Shan, J. W. Ager III, E. E. Haller, H. Lu, W. J. Schaff, W. K. Metzger, and S. Kurtz, J. Appl. Phys. 94, 6477 (2003).

[42] O. Jani, I. Ferguson, C. Honsberg, and S. Kurtz, Appl. Phys. Lett. 91, 132117 (2007).

[43] R. Singh, D. Doppalapudi, T. Moustakas, and L. Romano, Appl. Phys. Lett. 70, 1089 (1997).

[44] S. Porowski, and I. Grzegory, J. Cryst. Growth 178, 174 (1997).

[45] G. A. Slack, and T. F. McNelly, J. Cryst. Growth 34, 263 (1976).

[46] A. J. Sierakowskia, and L. F. Eastman, J. Appl. Phys. 86, 3398 (1999).

[47] Y. F. Wu, B. P. Keller, P. Fini, S. Keller, T. J. Jenkins, L. T. Kehias, S. P. DenBaars, and U. K. Mishra, IEEE Electron Device Lett. 19, 50 (1998).

[48] S. T. Sheppard, K. Doverspike, W. L. Pribble, S. T. Allen, J. W. Palmour, L. T. Kehias, and T. J. Jenkins, IEEE Electron Device Lett. 20, 161 (1999).

[49] B. K. Ridley, J. Appl. Phys. 84, 4020 (1998).

[50] U. V. Bhapkar, and M. S. Shur, J. Appl. Phys. 82, 1649 (1997).

[51] J. Kolnik, I. H. Oguzman, K. F. Brennan, R. Wang, P. P. Ruden, and Y. Wang, J. Appl. Phys. 78, 1033 (1995).

[52] H. Morkoç, Beyond SiC! III-V Nitride Based Heterostuctures and Devices, in SiC Materials and Devices, Y. S. Park (ed.), Willardson and Beer Series, Willardson and Weber (eds.) 52, Chap. 8, pp. 307-394 (Academic Press, 1998).

[53] Y. F. Wu, B. P. Keller, P. Fini, S. Keller, T. J. Jenkins, L. T. Kehias, S. P. Denbaars, and U. K. Mishra, IEEE Electron. Dev. Lett. 19, 50 (1998).

[54] A. T. Ping, Q. Chen, J. W. Yang, M. A. Khan, and I. Adesida, IEEE Electron. Dev. Lett. 19, 54 (1998).

[55] G. J. Sullivan, M. Y. Chen, J. A. Higgins, J. W. Yang, Q. Chen, R. L. Pierson, and B. T. McDermott, IEEE Electron. Dev. Lett. 19, 198 (1998).

[56] S. Binari, J. M. Redwing, G. Kelner, and W. Kruppa, Electron. Lett. 33, 242 (1997).

[57] C. Y. Yeh, Z. W. Lu, S. Froyen, and A. Zunger, Phys. Rev. B 46, 10086 (1992).

[58] H. Morkoç, S. Strite , G. B. Gao, M. E. Lin, B. Sverdlov, and M. Burns, J. Appl. Phys. 76, 1363 (1994).

[59] S. C. Jain, M. Willander, J. Narayan, and R. V. Overstraeten, J. Appl. Phys. 87, 965 (2000).

[60] S. N. Mohammad, and H. Morkoç, Prog. Quant. Electr. 20, 361 (1996).

[61] L. Liu, and J. H. Edgar, Mat. Sci. and Eng. R 37, 61 (2002).

[62] B. Gil, Physics and applications, Clarendon Press (1998).

[63] M. A. Mastro, O. M. Kryliouk, T. J. Anderson, A. Davydov, and A. Shapiro, J. Cryst. Growth 274, 38 (2005).

[64] J. Rouviére, J. Weyher, M. Seelman-Eggebert, and S. Porowski, Appl. Phys. Lett. 73, 668 (1998).

[65] O. Ambacher, Journal of Physics D: Applied Physics 31, 2653 (1998).

[66] T. D. Veal, C. F. McConville, and W. J. Schaff, CRC Press Taylor & Francis Group, Chapter 2 (2010).

[67] T. Sugahara, H. Sato, M. Hao, Y. Naoi, S. Kurai, S. Tottori, K. Ymashita, K. Nishimo, L. T. Romano, and S. Sakai, J. J. Appl. Phys. 37, L398 (1998).

[68] D. Cherns, S. J. Henley, and F. A. Ponce, Appl. Phys. Lett. 78, 2691 (2001).

[69] X. H. Wu, L. M. Brown, D. Kapolnek, S. Keller, B. Keller, P. DenBaars, and J. S. Speck, J. Appl. Phys. 80, 3228 (1996).

[70] F. A. Ponce, D. Cherns, W. T. Young, and J. W. Steeds, Appl. Phys. Lett. 69, 770 (1996).

[71] http://www.google.fr/search?q=screw+and+edge+dislocations&source=lnms&tbm=isch&sa=X&ved=0ahUKEwjpn8nFzP_ZAhXCvBQKHTj9DncQ_AUICigB&biw=1280&bih=927#imgdii=UQGhzEGU-4BL2M:&imgrc=OXAqs9FfmZ1aAM.

[72] W. Paszkowicz, R. Cerny, and S. Krukowski, Powder diffraction 18, 114 (2003).

[73] A. R. D Yadira, A Ph.D thesis on “Characterization of A-plane Grown GaN on Sapphire Substrates by Electron Microscopy”, Lausanne, EPFL (2009).

[74] S. Tanaka, R. S. Kern, and R. F. Davis, Appl. Phys. Lett. 66, 1 (1995).

[75] C. D. Lee, Ashutosh sagar, R. M. Feenstra, W. L. Sarney, L. salamanca-riba, and J. W. P. Hsu, Phys. Stat. Sol. (a) 188, 595 (2001).

[76] S. Srinivasan, L. Geng, R. Liu, F. A. Ponce, Y. Narukawa, and S. Tanaka, Appl. Phys. Lett.

83, 5187 (2003).

[77] J. W. Matthews, and A. E. Blakeslee, J. Cryst. Growth 27, 118 (1974).

[78] J. W. Matthews, S. Mader, and T. B. Light, J. Appl. Phys. 41, 3800 (1970).

[79] B. Jahnen, M. Albrecht, W. Dorsch, S. Christiansen, H. P. Strunk, D. Hanser, and R. F. Davis, MRS Internet J. Nitride Semicond. Res. 3, 39 (1998).

[80] J. W. Ortony, and C. T. Foxonz, Rep. Prog. Phys. 61, 1 (1998).

[81] J. Wu, J. Appl. Phys., 106, 011101 (2009).

[82] S. Nakamura, and G. Fasol, The Blue Laser Diode, Springer, Berlin, (1997).

[83] D. B. Nicol, A Ph.D thesis on “A novel solid state general illumination source”, Georgia Institute of Technology (2006).

Chapter 2

Experimental techniques

In this work, the main technique that has been used to investigate the relaxation of the strain in InGaN/GaN heterostructures is Transmission Electron Microscopy (TEM). The nitride materials do not exist as minerals, therefore the active layers are obtained by deposition on various substrates. Up to now, metal organic vapor phase epitaxy has come to dominate the nitride market due probably to many factors such as adequacy to high temperature, scaling up in size which is necessary for mass production, etc. However, in order to apprehend the mechanisms that underlie this relaxation, it was also necessary to investigate samples which have been grown by molecular beam epitaxy. Prior to transmission electron microscopy, all the samples were first analyzed by atomic force microscopy in order to determine their surface structure in correlation with the growth conditions.

In the following, we briefly describe the experimental techniques, starting with the growth methods. The chapter will finish by a short presentation of the atomic force microscopy and the transmission electron microscopy.

2. 1 Metal Organic Vapor Phase Epitaxy (MOVPE)

MOVPE is an efficient method for the growth of group III nitride structures, quantum wells as well as superlattices [1]. This method can produce atomically sharp interfaces. Its good uniformity, high growth rate, large area as well as multiple wafer growth have attracted the nitride industry for mass production of devices.

The basic principle of MOVPE is that precursors made of highly unstable compounds containing desired atoms are driven to a hot substrate surface using carrier gases such as hydrogen and nitrogen. When they touch the hot active surface, they decompose and the epitaxy is expected to take place. Of course the process is complex, and the environment condition will govern the adsorbates on the substrate surface toward the formation of the epilayer. For our samples, the organic precursors were trimethylgallium (TMGa) for Ga, trimethylindium (TMIn) for In and ammonia (NH_3) as nitrogen source. However, triethyls (Ga/In) are also often used. More important, the reaction residues should efficiently be evacuated by the carrier gas in order to obtain extremely high quality epitaxial layers. This is tuned through the optimization of the growth parameters, such as chamber pressure, substrate temperature, reactor design as well as gas flow rate. They have a strong influence on the growth rate, surface morphology as well as electrical properties of the final active layers. For instance, the growth rate and surface morphology are known to be strongly dependent on growth temperature. The layer surface morphology is also affected by the reactor design. It worth to point out that MOVPE requires high growth temperature, because it must satisfy the condition of NH_3 pyrolysis, the enhanced NH_3 decomposition during growth is essential in improving the electrical properties of the active layers.

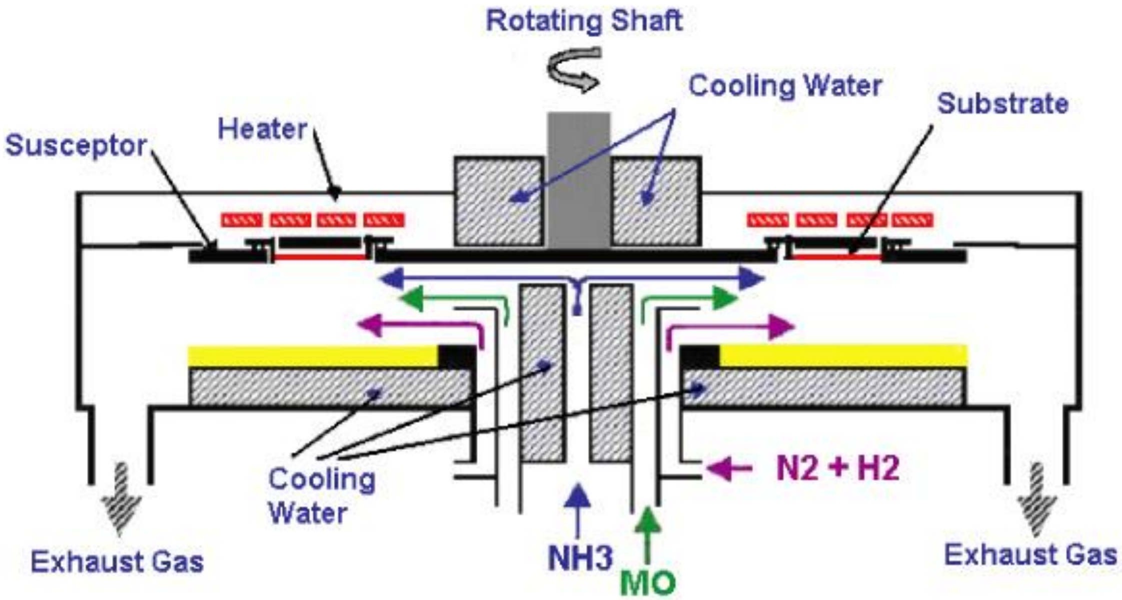

Figure 2.1 Schematics of a MOVPE system that consists of face down multiwafer set-up, gear driven wafer rotation and separated flow of active species [2].

Figure 2.1 shows a schematic representation of an atmospheric-pressure reactor [2]. Various designs may involve up to three separated fluxes, ammonia, metal organics as well as carrier gas. To guarantee thickness and alloy composition homogeneities, the substrates are rotated, either as a whole or in a planetary way inside a multiwafer chamber.

2. 2 Molecular Beam Epitaxy (MBE)

Since A. Y. Cho and J. R. Arthur first used molecular beam epitaxy (MBE) in the late 1960s [3], it has evolved into one of the most widely used techniques for producing high purity epitaxial layers.

MBE is a two-step process carried out in an ultrahigh vacuum environment [4]. As shown in Figure 2.2, the first step is the evaporation of atoms or molecules which are the constituents of the growing materials from solid sources in heated cells. The evaporated particles are then collimated into beams and directed toward a heated substrate. The particles in the beams behave as a molecular flow (thus the name “molecular beam epitaxy”) which is led to deposit on a heated substrate surface. The substrate is rotated to obtain uniform distribution of incoming molecules. In a second step, the deposited species migrate on the surface until their incorporation onto the crystal lattice of the substrate or the growing epitaxial layer. This step determines the morphology of the thin film, which depends on the factors such as reconstruction of the substrate surface, the surface temperature, the evaporation rate and the crystallographic orientation, etc, ...

MBE can provide good uniformity and atomically sharp interfaces even at substantially low growth temperatures, moreover it provides accurate in-situ monitoring capabilities. Therefore, MBE is very suitable for precisely controlling the growth parameters. For the growth of group III nitrides, of course the metal atoms come from solid source, and the main difficulty for the growth of these materials by MBE has for a long time been the nitrogen source. Laterly, Plasma Assisted MBE, which uses a plasma to crack the N_2 molecule, has proved to be a more efficient nitrogen source than NH_3.

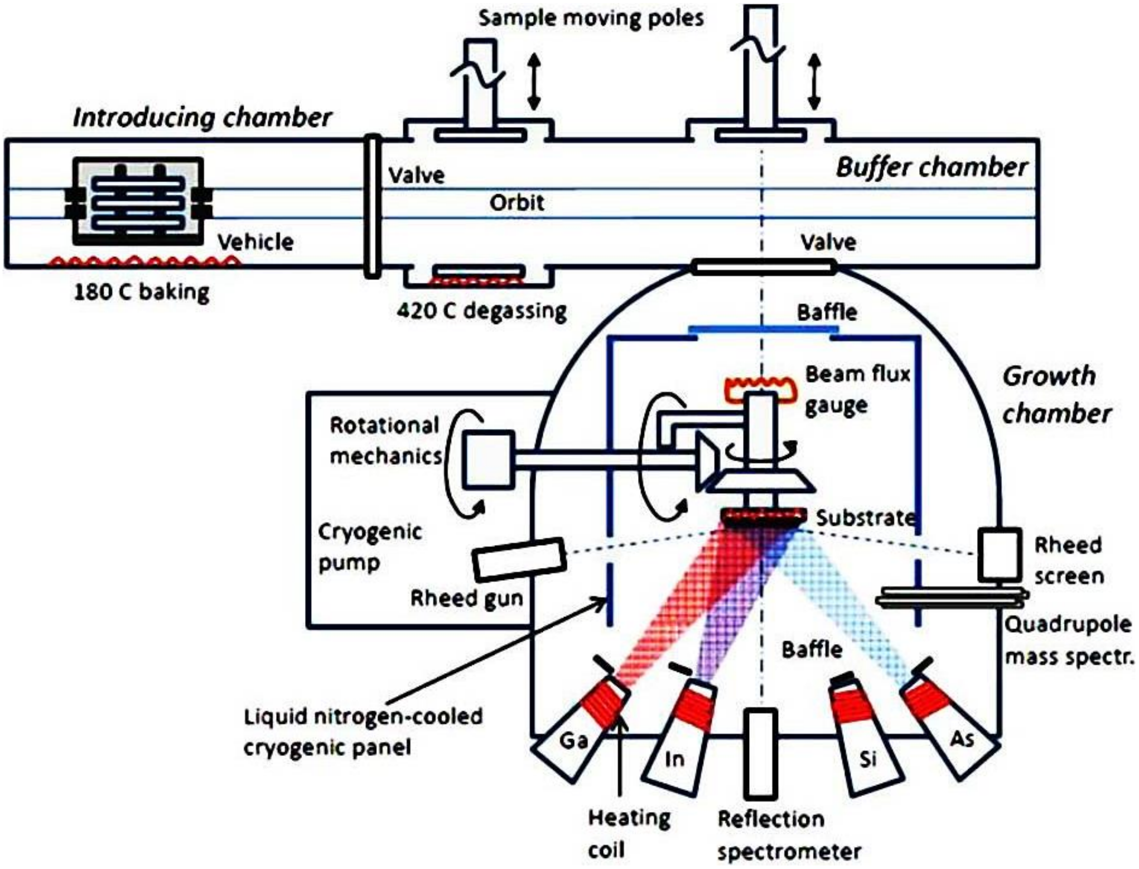

Figure 2.2 Schematic diagram of a MBE system shows the main components of a growth chamber [5].

2. 3 The investigated samples

In this work, the aim being to understand the relaxation of the interfacial strain at the InGaN/GaN interface, we needed to scan through most of the indium composition range. We started by analyzing samples grown by MOVPE at AIXTRON. It rapidly came out that when increasing the indium composition, many issues emerged such us layer morphology. Therefore, we also investigated InGaN layers up to 35% indium, where the layer thickness could be increased up to around 0.5 µm while keeping a relatively good surface morphology. These layers were grown by plasma assisted MBE at INAC Laboratory Grenoble. Whether the main substrate which was used was mainly sapphire, we also had the opportunity to investigate samples grown by MOVPE on free standing GaN substrates in a collaboration with École Polytechnique Fédérale de Lausanne (EPFL), Switzerland. In this instance, our aim was to determine the pure mechanism of strain relaxation, without the possible role of the threading dislocations and other defects that are usually generated at the GaN/sapphire interface. At this interface, not only there is a large lattice mismatch (16%), but also a symmetry difference, and even larger mismatch along the [0001] where possible surface steps often play a critically important role in initiating other types of defects such as inversion domains, basal as well as prismatic stacking faults inside the nitride layer [6].

2. 4 Microscopy techniques

The investigation of our materials went from determining the surface morphology to transmission electron microscopy where the interfacial relationships were analyzed. Therefore, all the samples were first observed using atomic force microscopy.

2. 4. 1 Atomic Force Microscopy (AFM)

AFM is probably the most straightforward technique to determine the surface morphology at atomic resolution as well as to provide a quantitative measurement of the surface roughness of the thin films from the micron down to the nanometer scale [7]. The root mean square (rms) of roughness is a standard deviation of the z values in a given area, it is directly provided through the processing of the acquired images. As shown in Figure 2.3, the AFM consists of a microscale cantilever with a sharp tip mounted at the end of the cantilever and used to scan across the surface of the sample. When the probe is brought into proximity of a specimen surface, forces between the probe and the specimen lead to a deviation of the cantilever. In general, the force between the cantilever and the specimen is a sum of Van der Waals force, magnetic, electrostatic, electrodynamic, chemical bonding and capillary forces, which are compensated by elasticity forces due to the cantilever bending and the specimen deformation. The deviation is measured using a laser spot reflected from the top surface of the cantilever into an array of photodiodes. A feedback mechanism is used to adjust the probe-to-specimen distance to maintain a constant force between the probe and the specimen. The specimen can move in z direction for maintaining a constant force, and x and y directions for imaging the surface in Å scale by three piezo crystal sensors which allows driving very precise specimen movement. There are three scanning modes associated with AFM, namely, contact mode, non-contact mode and tapping mode.

In the contact mode, the probe is brought down onto the specimen surface, then raster-scanned across the specimen in the xy-plane. The probe is static and in contact with the specimen, the image is obtained by repulsive force between the probe and the specimen. This procedure often damages either the probe or the specimen surface.

In non-contact mode, the probe of the cantilever does not touch the specimen surface, the probe oscillates above the surface, and the image is obtained from the attractive forces between the probe and the specimen. The cantilever is instead oscillated at either its resonant frequency (frequency modulation) or just above (amplitude modulation) where the amplitude of oscillation is typically a few nanometers (< 10 nm) down to a few picometers [8]. The Van der Waals forces, which are strongest from 1 nm to 10 nm above the surface, or any other long-range force that extends above the surface acts to decrease the resonance frequency of the cantilever. This decrease in resonant frequency combined with the feedback loop system maintains a constant oscillation amplitude or frequency by adjusting the average probe-to-specimen distance. Measuring the probe-to-specimen distance at each (***x***, ***y***) data point allows to construct a topographic image of the sample surface.

In the tapping mode, the cantilever is driven to oscillate up and down at or near its resonance frequency. This oscillation is commonly achieved with a small piezo element in the cantilever holder, other possibilities include a magnetic field of alternating current (with magnetic cantilevers), piezoelectric cantilevers, or periodic heating with a modulated laser beam. The amplitude of this oscillation usually varies from several nm to 200 nm. In tapping mode, the frequency and amplitude of the driving signal are kept constant, leading to a constant amplitude of the cantilever oscillation as long as there is no drift or interaction with the surface. The interaction of forces acting on the cantilever when the tip comes close to the surface, Van der Waals forces, dipole-dipole interactions, electrostatic forces, etc. cause the amplitude of the cantilever's oscillation to change (usually decrease) as the tip gets closer to the sample. A tapping AFM image is produced by imaging the force of the intermittent contacts of the tip with the sample surface [9].

Although the peak forces applied during the contacting part of the oscillation can be much higher than typically used in contact mode, tapping mode generally lessens the damage done to the surface and the tip compared to the amount done in contact mode. When operating in tapping mode, the phase of the cantilever's oscillation with respect to the driving signal can be recorded as well. This signal channel contains information about the energy dissipated by the cantilever in each oscillation cycle. Samples that contain regions of varying stiffness or with different adhesion properties can give a contrast in this channel that is invisible in the topographic image.

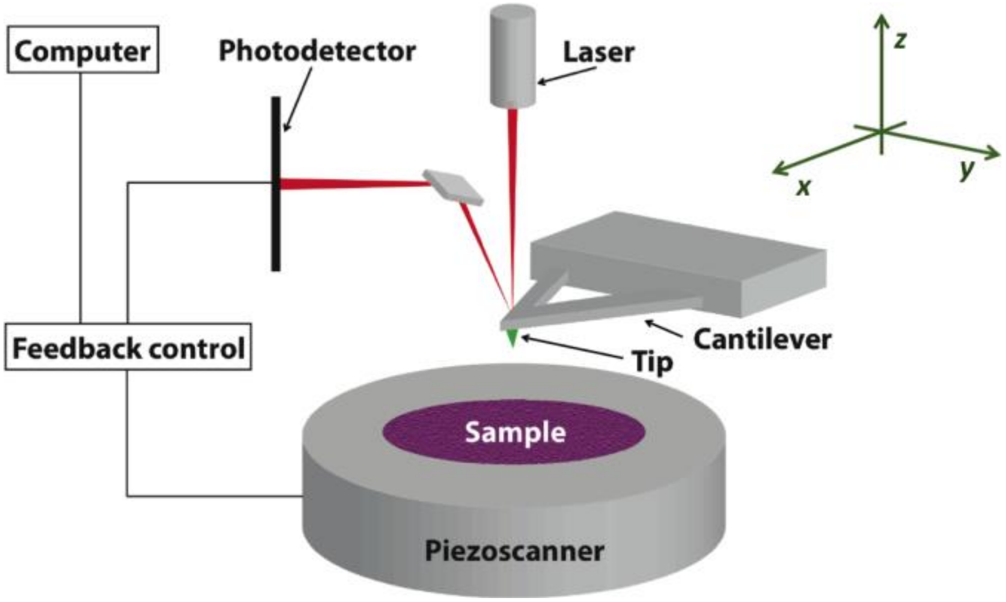

Figure 2.3 Schematic diagram of a AFM with components [7].

All the AFM observations in this work, which will be discussed in the following chapters, were obtained in tapping mode using a nanoscope III AFM from Digital Instruments using silicon tips (10 nm of radius of curvature).

2. 4. 2 Transmission Electron Microscopy (TEM)

In an electron microscope, an electron beam of high energy is used to illuminate the object and a magnified image is produced using electromagnetic lenses [10, 11]. The observations provide a projected pattern for the local structure of the sample in direct space through the images and in the reciprocal space by the diffraction mode. Electron microscopy is possible because the interaction of electrons with matter brings about changes in the electron waves. When an electron beam hits a sample, several signals are generated from this strong interaction as shown in Figure 2.4.

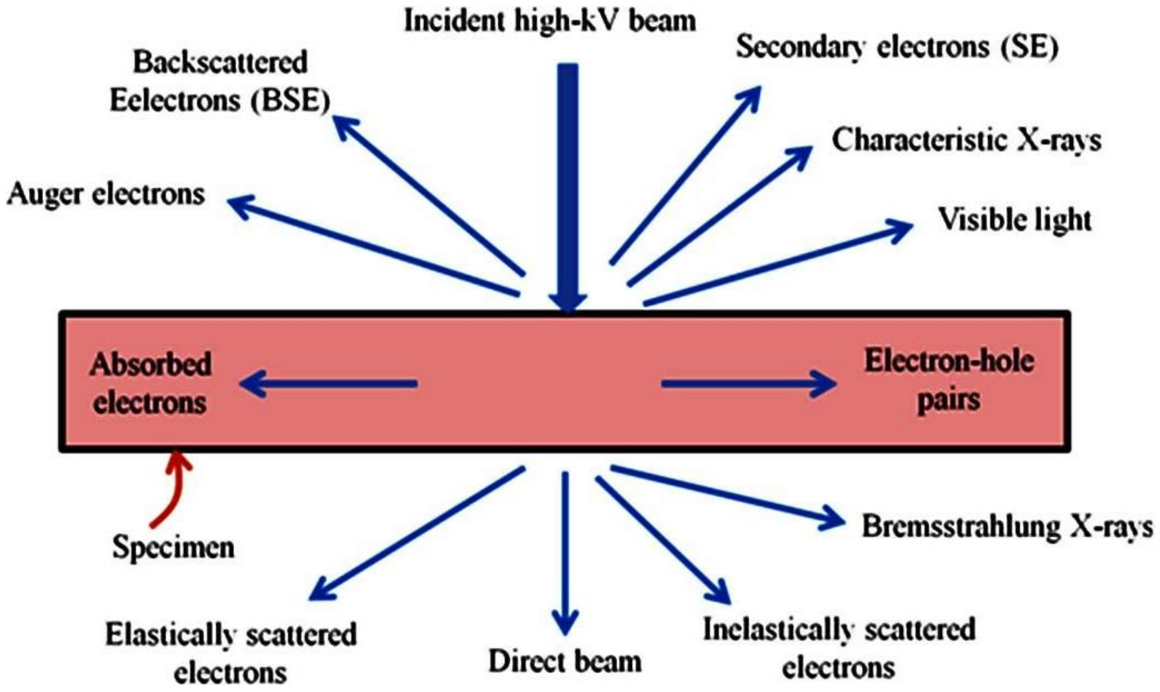

Figure 2.4 Possible signals resulting from the interaction of high energy electron beams with a material [12].

The numerous emitted signals have given rise to the many techniques for local investigation of materials in the TEM. For imaging, one mainly considers the forward scattering geometry which is the most predominant for the high energy electrons (> 80 kV), and this is the basis of transmission electron microscopy, where the exploited signals are in the transmission mode. The electron spectrum as detected past the specimen allows to quantify the energy losses and constitutes along with the spectroscopy of the emitted X rays interesting tools for the analysis of the local composition and electronic structures of the materials. Needless to mention that other signals are also generated all around the specimen and are effectively exploited in the scanning electron microscopy:

(1) the Back Scattered Electrons or reflected electrons which see their wave vector deviate at a 180° angle from the few first layers of the investigated material.

(2) The Secondary Electrons: they are ejected from the investigated material by collisions with the incident beam; their energy is conventionally below 50 eV.

(3) The photons with an extended range of wavelength are produced through the relaxation of the atoms of the sample and can be detected by cathodoluminescence.

Due to this strong interaction of electrons with matter, the electron microscope consists of a column with an electron gun at the top to generate the electron beam which is accelerated at a high voltage (> 20 keV for the transmission mode). Along its propagation, a series of magnetic lenses are used to manipulate it in order to get the necessary information from the materials under investigation. The main features of a TEM are shown in Figure 2.5. First, the condenser lenses are used to shape the electron beam onto specimen (probe size, parallel, and convergence). The objective lens forms the image of the specimens. The intermediate lens is used to magnify the image or the diffraction pattern, which is formed in the focal plane of the objective lens. And finally the projector lens is used to control the magnification of the final image or diffraction pattern which is collected from the sample onto a detector.

The major advantage of electron microscopy is that it deals with mostly coherent beam of electronic light with short wavelengths (200 keV, 2.52 pm). Indeed, with a point source at more than 1m from the object plane, the image in the back focal plane of the objective lens corresponds to the reciprocal space of the object, where a planar section is visible. As a direct consequence the Bragg angles are very small (fractions of mrads) and many atomic lattice planes can simultaneously be in diffracting position in contrast to X ray diffraction where the wavelengths are around 0.1 nm. For materials characterization, this diffraction information is used in different imaging modes, like bright field, dark field, as well as High Resolution TEM.

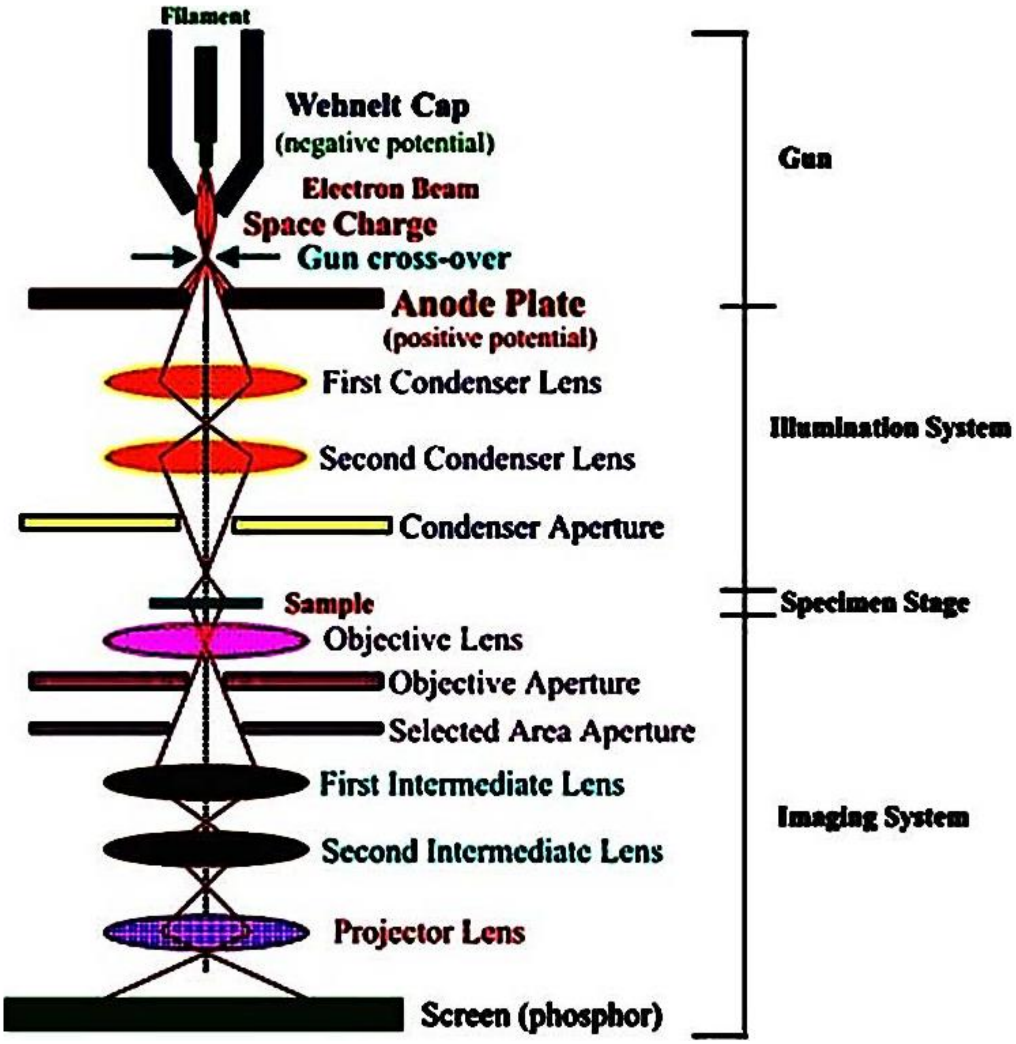

Figure 2.5 Schematic diagram of a TEM consists of electron gun, illumination system (condenser lenses), imaging system (objective and post object lenses) [13].

One beam images: Bright Field (BF) and Dark Field (DF)

BF and DF imaging techniques are employed to form images using the transmitted beam or a diffracted beam as shown in Figure 2.6. When the direct beam is selected by the objective aperture, we form the BF image whereas the selection of diffracted beam gives the DF image. Usually, the DF images are obtained by a slight tilting the incident beam to have the diffracted beam on the optical axis, thus minimizing aberrations.

High Resolution TEM (many beam images)

High Resolution TEM, the contrast in high resolution is due to the interference of the transmitted and diffracted beams, it is called phase contrast, as shown in Figure 2.6. In this process, the interactions of the transmitted and diffracted beams give rise to constructive or destructive interference whose patterns display maxima and minima which may in particular conditions allow the imaging of the local atomic structure of the material under investigation.

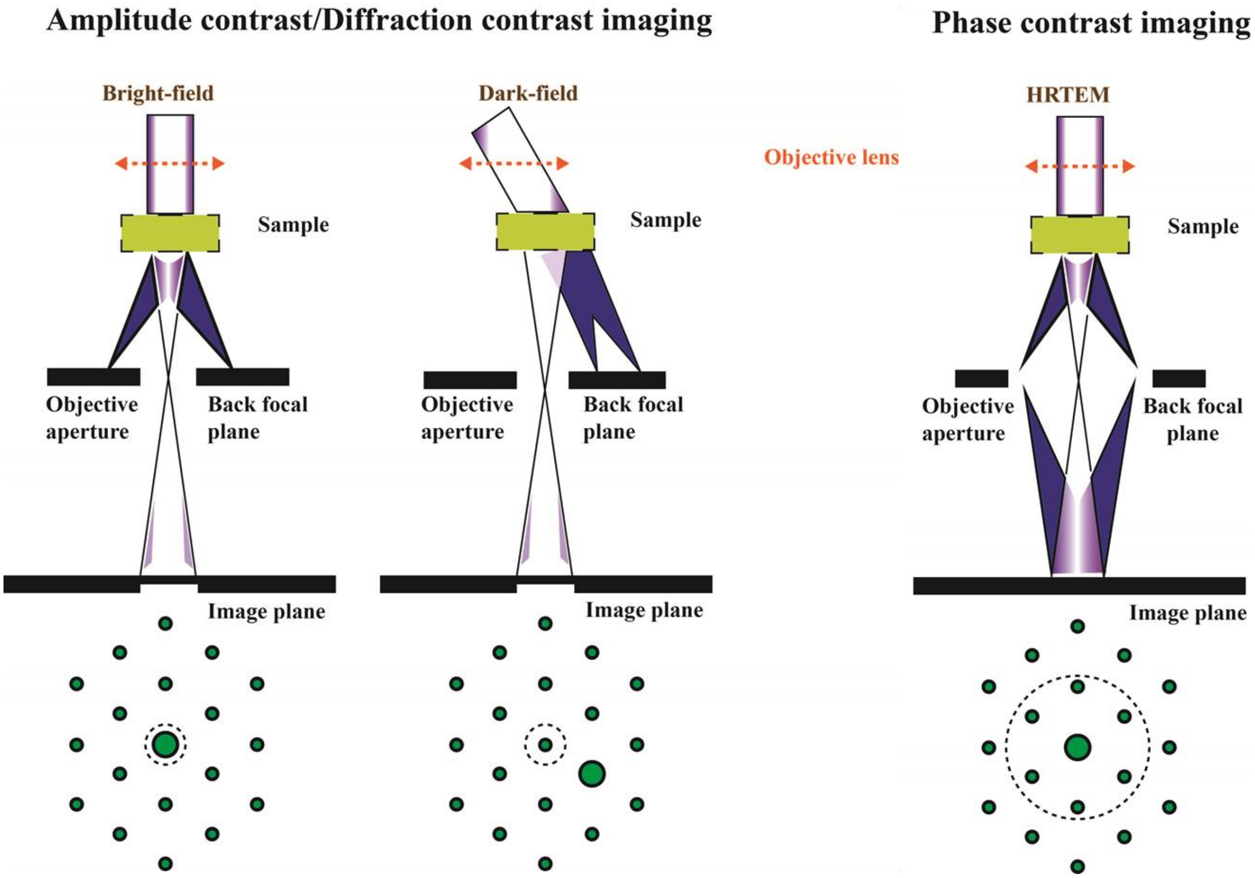

Figure 2.6 Ray diagrams: The image of BF, DF and High Resolution imaging [13].

Dislocation analysis from TEM image

In order to analyze cross-sectional and plan-view dislocation observations, we extract several significant information from TEM images, as indicated in the following:

(1) The direction and the magnitude of the Burgers vector (***b***), perpendicular to the (hkl) diffracting planes.

(2) The direction of the dislocation line and therefore the character of the dislocation (screw, edge or mixed type).

(3) The density of the dislocation.

The visibility criterion uses the diffraction vector ***g*** and the Burgers vector ***b***, when ***g . b*** = 0, there will be no contrast from the dislocation in the image, and therefore it will be invisible in BF or DF image [14]. We have summarized the visibility criteria for the dislocations which are usually observed in group III nitride epitaxial layers (Table 2.1).

Table 2.1 Visibility criteria of the dislocations in wurtzite system.

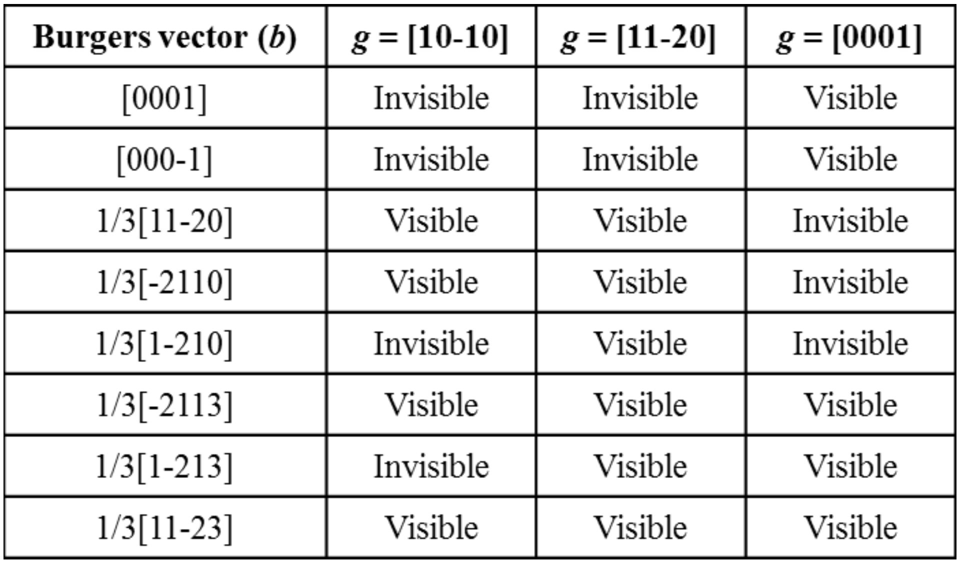

Burgers vector (*b*)	***g* = [10-10]**	***g* = [11-20]**	***g* = [0001]**
[0001]	Invisible	Invisible	Visible
[000-1]	Invisible	Invisible	Visible
1/3[11-20]	Visible	Visible	Invisible
1/3[-2110]	Visible	Visible	Invisible
1/3[1-210]	Invisible	Visible	Invisible
1/3[-2113]	Visible	Visible	Visible
1/3[1-213]	Invisible	Visible	Visible
1/3[11-23]	Visible	Visible	Visible

For our investigation, a major part of TEM was performed by JEOL JEM-2010 operated at an accelerating voltage of 200 kV using a thermoionic lanthanum hexaboride (L_aB_6) source, as shown in Figure 2.7 (a). This TEM is mainly used for conventional observation, for example, low magnification of observation in cross-sectional, plan-view, two beam as well as weak beam. Figure 2.7 (b) gives the shoulder of the sample and the magnification figure of its head.

200 kV High Resolution TEM with a maximum point resolution of 0.19 nm (the $C_s = 1.4$ mm for HRTEM) was also used in our investigation for high resolution imaging. Scanning TEM and X-ray diffraction were used in this study for the crystalline quality and the diffraction peak of the epitaxial layer, respectively.

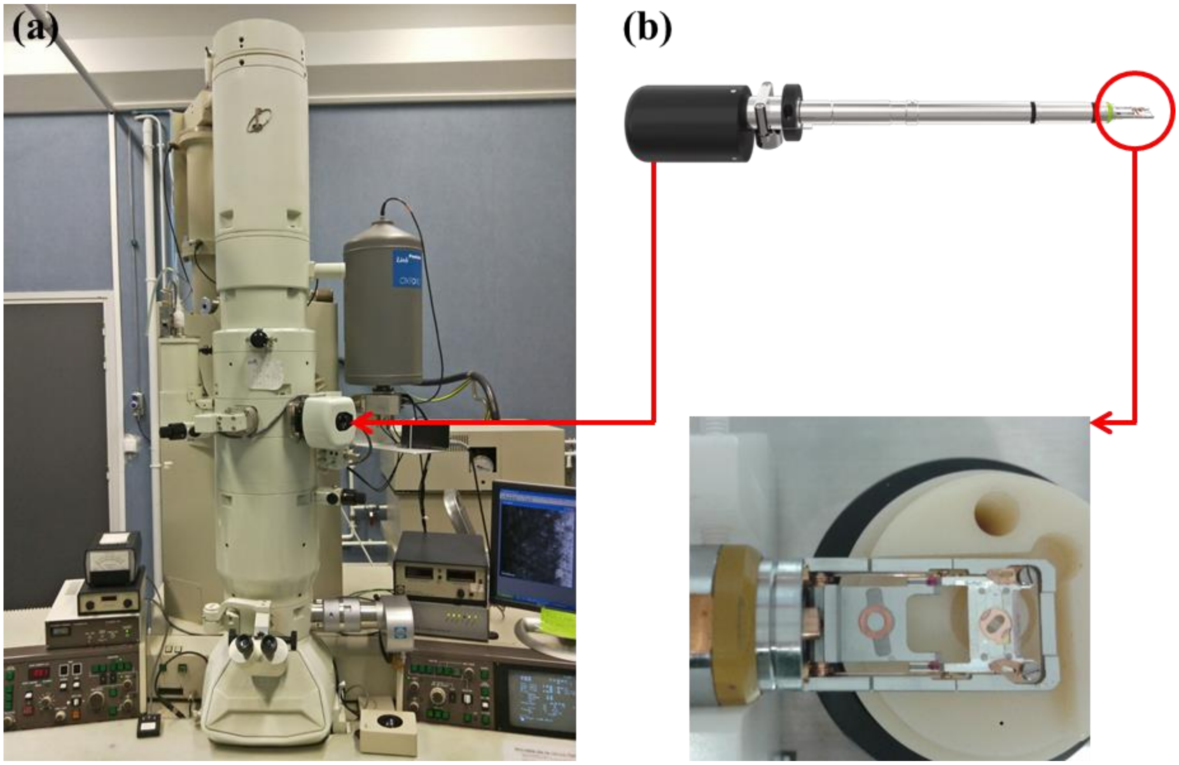

Figure 2.7 (a) The JEOL 2010, (b) TEM sample shoulder and magnification figure of its head.

2. 5 TEM specimen preparation

For TEM investigations, the samples need to be transparent to the electrons, therefore depending on the Z, the thickness of the thin foil should be below 300-500 nm. In this work, the investigations were made on cross section and plan view specimens. In order to attain electron transparency, for both types of samples, specific preparation needs to be undertaken. First of all, the sample holders which are used in the TEM impose to make observation within areas of less or equal to 3 mm in diameter. Therefore the TEM sample preparation procedure requires the three following steps:

2. 5. 1 Shaping the samples

First of all, the samples need to be cut to the correct dimensions, to this end, we use a “Precision Diamond Wire Saw 3242” which allows the operator to position the specimen inside the wire loop for a clear view for positioning and cutting, as shown in Figure 2.8 (a). It has two micrometers, one for accurate positioning of the specimen, the other for setting the depth of a slice. In the process, an adjustable electrical end-switch signals when the desired depth of cut is obtained and the motor is automatically shut off [15].

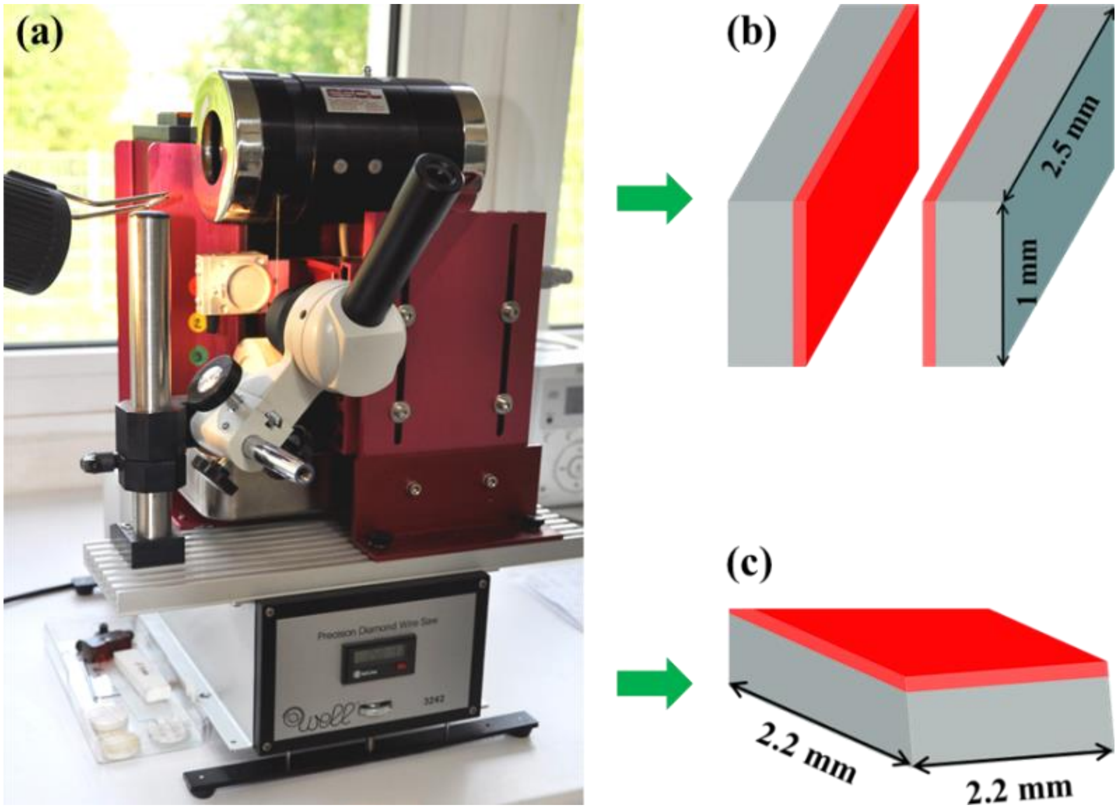

Figure 2.8 (a) The Precision Diamond Wire Saw 3242, (b) the cross-sectional slice of 2.5 × 1 mm^2, and (c) the plan-view slice of 2.2 × 2.2 mm^2.

For the cross-sectional specimens, slices of 2.5 × 1 mm^2 were cut from the substrate along the [11-20] and [10-10] directions (see Figure 2.8 (b)). Then two of such slices were pasted face to face with epoxy glue in order to protect the areas of interest which are quite close to the surfaces. For the plane-view observation, specimens were cut into 2.2 × 2.2 mm^2 (see Figure 2.8 (c)), which is quite large but is still less than the diameter of the sample holder which is 3 mm.

2. 5. 2 Thickness reduction by mechanical polishing

During this step, we have used a “Allied MultiPrep System” which enables precise semiautomatic specimen preparation of a wide range of materials for microscopic evaluation, as shown in Figure 2.9 (a). The main interest for us lies in its capabilities include parallel polishing with accuracy which is well below and may allow to fabricate directly lamellas which are transparent to electron (100 nm) [16]. However, for best reproducible results we preferred to stop this polishing at around 10 μm of the cross-sectional (see Figure 2.9 (b)) and the plan-view (see Figure 2.9 (c)) lamellas with parallel surfaces using a series of polishing papers from 30 μm to 0.5 μm (see the inset in Figure 2.9 (a)). This is easily obtained through dual micrometers (pitch and roll) which allow precise sample tilt adjustments relative to the abrasive plane. Moreover, a rigid Z-indexing spindle maintains the predefined geometric orientation throughout the grinding/polishing process. And digital indicators enable quantifiable material removal, which can be monitored real-time, or preset for unattended operation. Variable speed rotation and oscillation maximize use of the entire grinding/polishing disc and minimize artifacts. Adjustable load control expands its capability to handle a range of small (delicate) to large samples.

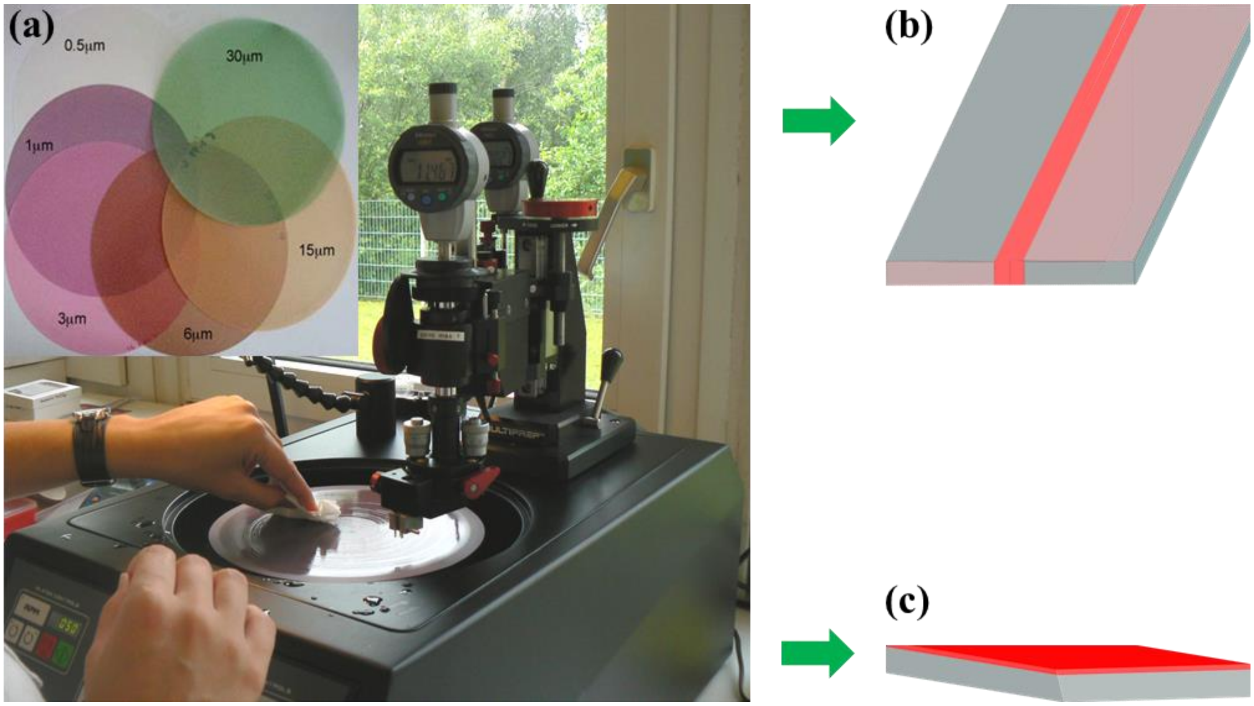

Figure 2.9 (a) The MultiPrep System, the inset shows the polishing papers from 30 µm to 0.5 µm, (b) cross-sectional, and (c) plan-view lamellas of 10 µm thickness after polishing.

2. 5. 3 Ion polishing

Instead of carrying out the mechanical polishing, we have chosen to terminate the preparation of thin lamellas using a PIPS Gatan Ion Polisher which allows the preparation of high-quality planar cross sections from all types of difficult samples, as shown in Figure 2.10 (a). Indeed, our samples needed to be maintained at low temperature (liquid nitrogen) and be finished at low thinning energies (~100 eV). Moreover, this instrument can perform masked broad ion beam milling, also known as “slope cutting”. This surface preparation technique utilizes a large (1 mm) ion beam to strip away an extensive, finely polished area for subsequent microscopy and microanalysis. A solid, sputter-resistant shield blocks half of the ion beam, effectively masking the lower half of the beam and creating a lateral sputtering plane that strips away a thin layer of the sample surface [17]. The resulting surface is very flat and usually free of artifacts. For the

TEM investigation, the samples were prepared by a two-step process: the tripod wedge mechanical thinning of the samples to 10 um, followed by ion milling at –150 ^{o}C and –40 ^{o}C with 5 keV Ar^{+} gun incident at 5° angle to the cross-sectional (see Figure 2.10 (b)) and the plan-view (see Figure 2.10 (c)) samples surface respectively until close to the electron transparency and the voltage was lowered progressively to 100 V toward the electron transparency in order to avoid the ion beam damage.

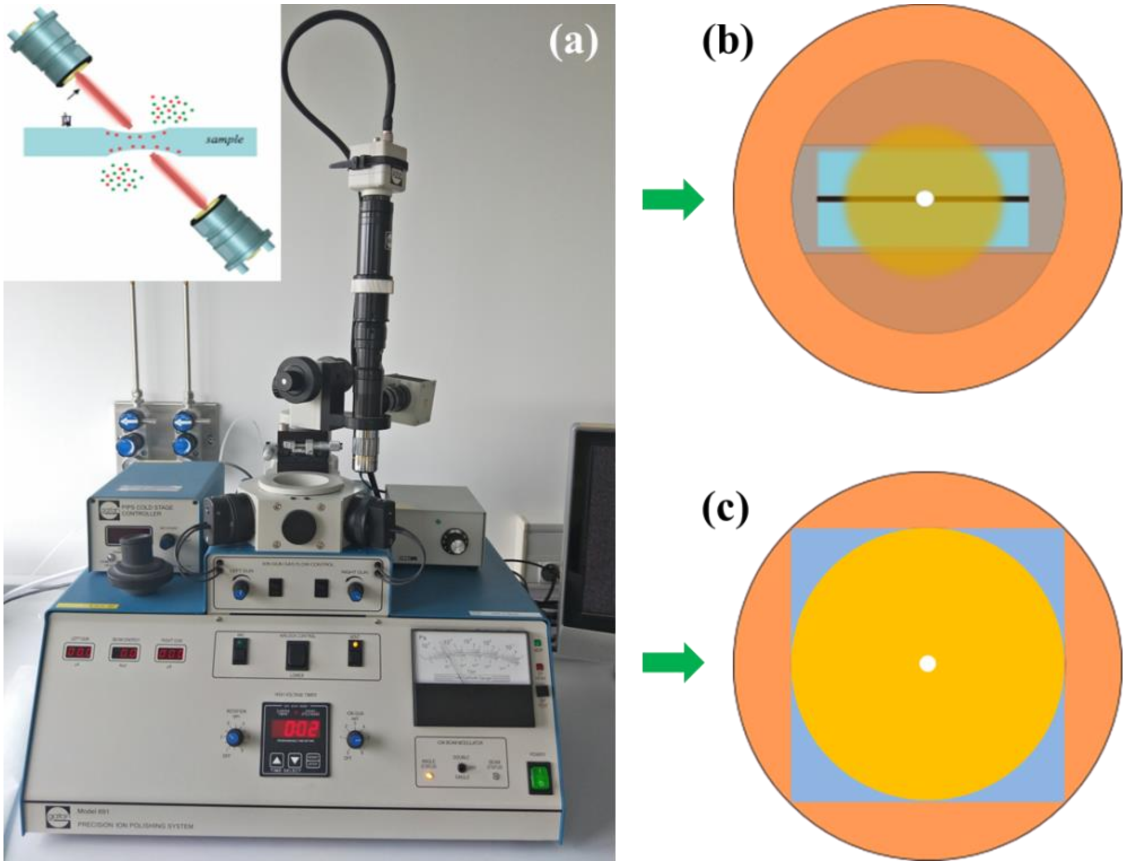

Figure 2.10 (a) The PIPS Gatan Ion Polisher, the inset displays ion beam milling process, (b) cross-sectional, and (c) plan-view specimens of the electron transparency after ion milling.

References

[1] S. Nakamura, T. Mukai, and M. Senoh, Appl. Phys. Lett. 64, 1687 (1994).

[2] P. Gibart, Rep. Prog. Phys. 67, 667 (2004).

[3] A. Y. Cho, and J. R. Arthur, Progress in Solid State Chemistry 10, Part 3, 157 (1975).

[4] M. A. Herman, and H. Sitter, Molecular Beam Epitaxy: Fundamentals and Current Status, 2nd ed. (Springer-Verlag, 1996).

[5] K. T. K. Prianka, M. B. Hosain, Anupama, H. Snigdha, and A. Arefin, Characterization and analysis of quantum-dot PV solar-cells, Chapter 4 (2016).

[6] P. Ruterana, V. Potin, B. Barbaray, and G. Nouet, Phil. Mag. A 80, 937 (2000).

[7] http://amyhallr.wordpress.com/2013/03/15/atomic-force-microscopy.

[8] L. Gross, F. Mohn, N. Moll, P. Liljeroth, and G. Meyer, Science, 325, 1110 (2009).

[9] Geisse, and A. Nicholas, Materials Today, 12, 40 (2009).

[10] http://www.fei.com/introduction-to-electron-microscopy/history.

[11] D. B. Williams, and C. B. Carter: Transmission Electron Microscopy: A Textbook for Materials Science, Ed. Springer (2009).

[12] http://nptel.ac.in/courses/102103044/module3/lec17/5.html.

[13] http://sites.google.com/site/bsatpati/tem.

[14] B. Fultz, and J. M. Howe, Transmission Electron Microscopy and diffractometry of material, Ed. Springer (2009).

[15] http://www.k5.ijs.si/en_US/equipment/nitna-zaga.

[16] http://www.alliedhightech.com/Equipment/multiprep-polishing-system-8.

[17] http://engineering.case.edu/centers/scsam/Gatan%20Ilion%20Ion%20Polisher.

Chapter 3

Metal Organic Vapor Phase Epitaxy of InGaN/GaN heterostructures

3. 1 Introduction

The direct band gap of $In_xGa_{1-x}N$ alloys can be engineered to emit light from ultraviolet to near infrared spectrum by tuning its band gap E_g from 0.65 eV to 3.4 eV through indium concentration of the film. Due to excellent emission properties, they have applications in light emitting diodes (LEDs) and laser diodes (LDs) [1, 2]. Recently, owing to their high absorption coefficient of $\sim10^5$ cm^{-1}, they have also been investigated for multijunction photovoltaics [3, 4]. Though, LEDs and LDs in the blue/ultraviolet represent the most efficient way to convert electrical power into light [5], the realization of LEDs past the green range has not yet been attained. The challenge probably lie within the phase diagram of the binary alloys of InN and GaN where, due to spinodal decomposition of InGaN alloys [6-9], phenomena such as chemical ordering [10], indium pulling [11, 12] and phase separation [13, 14] have been reported. Indeed, not only formation of indium-rich regions and indium dots [15-17], but also the phenomenon of local indium clustering or indium segregation [18, 19] has been observed. In fact, one of the intrinsic problems is also the lattice mismatch between GaN and InN upon the conventional growth along the [0001], where a buildup of the lattice strain is expected to take place. Therefore, the second challenge with the growth of InGaN/GaN heterostructure is the strain at the heterointerface. It should be noticed that the wurtzite structure has a smaller symmetry than the III-V compounds that crystallize in the cubic zinc blende, with reduced possibilities for defect glide in the conventional growth geometry in order to get rid of such strain by interface misfit dislocations.

In this chapter, we investigate the surface morphology and the microstructure of a series of $In_xGa_{1-x}N$/GaN heterostructures with varying indium concentration from a few percent to 100% grown by Metal Organic Vapor Phase Epitaxy (MOVPE) using AFM and TEM.

3. 2 The samples

The investigated samples consisted of $In_xGa_{1-x}N/GaN$ epilayers with varying In concentration ($0.04 < x \leq 1$). They were grown by MOVPE on GaN/sapphire substrates (L series), or on free standing GaN films (C series). The growth temperatures of the InGaN/GaN heterostructures were in the range of 700-730 ^{o}C. In order to control the indium composition, there was an interplay between the growth temperature and the TMIn/TMGa. The nominal In concentration was determined by high resolution X-ray diffraction technique. The nominal thickness of the InGaN epilayer was ~40 nm or ~100 nm for low In concentration of 0.04 to 0.25, and up to ~300 nm for high In concentration of 0.4 to 1. A schematic diagram of $In_xGa_{1-x}N/GaN$ heterostructures is shown in Figure 3.1.

The analytical details of the samples in terms of the thickness, the roughness, V-pit density, and lattice mismatch as calculated using the Vegard's law [20] are summarized in Table 3.1.

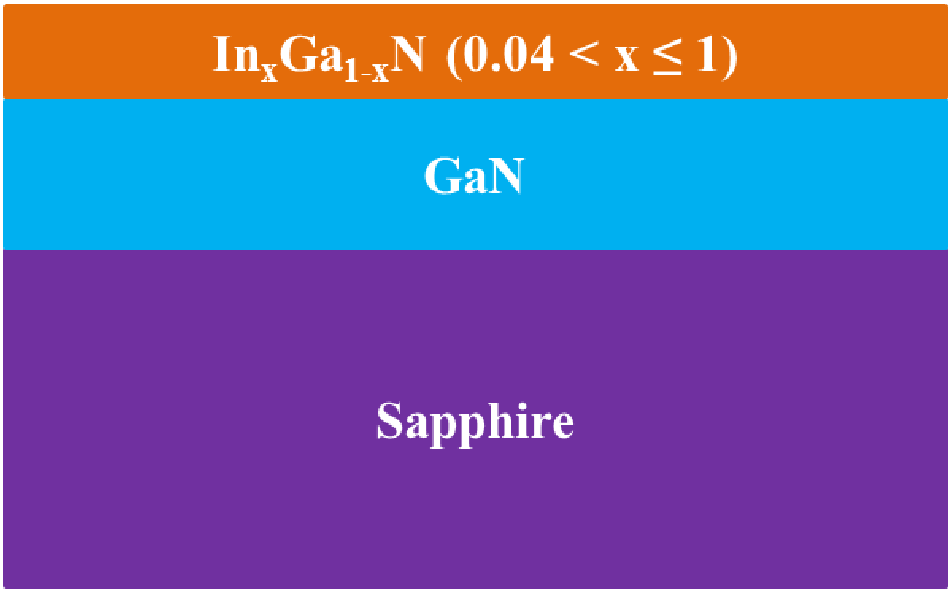

Figure 3.1 The schematic diagram of $In_xGa_{1-x}N/GaN$ heterostructure grown by MOVPE.

Table 3.1 The list of investigated samples, the nominal indium content, the thickness, the roughness, surface V-pit density and calculated lattice mismatch are exhibited.

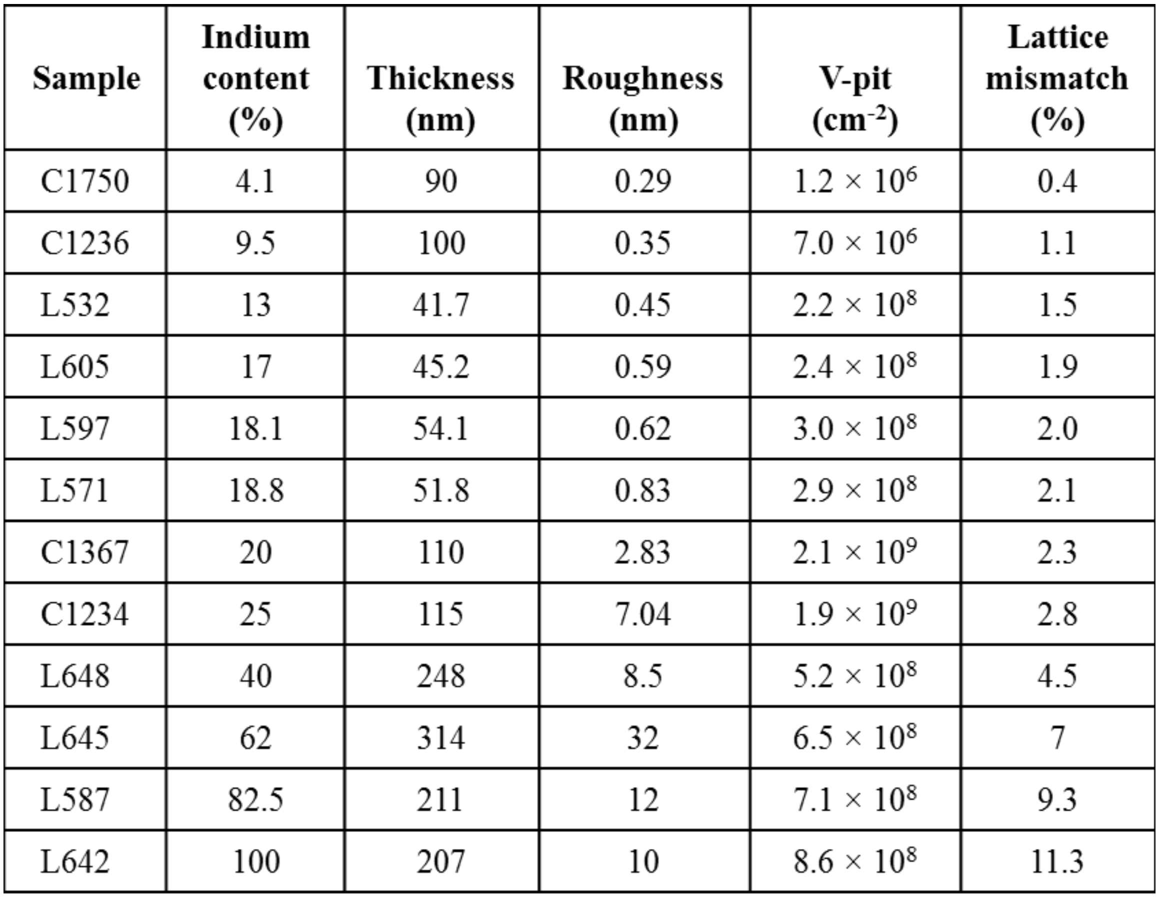

Sample	Indium content (%)	Thickness (nm)	Roughness (nm)	V-pit (cm^{-2})	Lattice mismatch (%)
C1750	4.1	90	0.29	1.2×10^6	0.4
C1236	9.5	100	0.35	7.0×10^6	1.1
L532	13	41.7	0.45	2.2×10^8	1.5
L605	17	45.2	0.59	2.4×10^8	1.9
L597	18.1	54.1	0.62	3.0×10^8	2.0
L571	18.8	51.8	0.83	2.9×10^8	2.1
C1367	20	110	2.83	2.1×10^9	2.3
C1234	25	115	7.04	1.9×10^9	2.8
L648	40	248	8.5	5.2×10^8	4.5
L645	62	314	32	6.5×10^8	7
L587	82.5	211	12	7.1×10^8	9.3
L642	100	207	10	8.6×10^8	11.3

3. 3 Structural analysis of MOVPE layers

All the above samples were first observed by AFM in order to determine the corresponding surface morphology, with possible densities of pinholes or V-pits. Then extensive analysis was carried out by transmission electron to characterize the interfaces and have access to the possible relaxation mechanisms of the misfit strain in relation with the growth conditions.

3. 3. 1 The surface morphology by AFM

Our atomic force microscopy observations point out interesting features that are typical characteristics of the investigated samples and their evolutions which critically depend on the indium composition. These features allow us to clearly distinguish the two series of samples: C-series where the heterostructures are grown on free standing GaN substrates, and L-series where the substrates are sapphire wafers. Therefore, when $x < 0.18$, as can be seen first on samples C1750 ($x = 0.041$) and C1236 ($x = 0.095$) for low indium content ($x < 0.1$), the surfaces exhibit step-terrace morphologies with the step height of ~$\boldsymbol{c}/2$ ($\boldsymbol{c}$ is the lattice constant of hexagonal GaN structure) for C1750 (Figure 3.2 (a)) and C1236 (Figure 3.2 (b)), respectively. Almost no V-shape defects can be seen on both samples, this is in agreement with the fact that the density of threading dislocations in the GaN free standing wafer is very low ($< 10^6$ cm^{-2}). At these 5×5 μm^2 areas, the average roughness of the two samples is also very low ~0.29 nm and ~0.35 nm, respectively.

In sample L532 with In concentration of 13% (L532), as shown in Figure 3.2 (c), the surface structure is completely different. As can be seen the surface exhibits hillocks, where each hillock may be topped with one or more V-pits, leading to a surface roughness around 0.4 nm. The estimated density of V-pits is ~2.2×10^8 cm^{-2}, which is in agreement with the density of the threading dislocations inside GaN templates grown on sapphire. With increasing In concentration to 17% (L605), as shown in Figure 3.2 (d), we observed that the entire surface morphology is mainly dominated by the presence of enlarged three-dimensional (3D) hillock structures. At the same time, we also observed V-pits all over the surface, and the density of V-pits is of ~2.4×10^8 cm^{-2}, which is almost equal to the density of V-pits of L532, its average roughness of the surface is of ~0.59 nm.

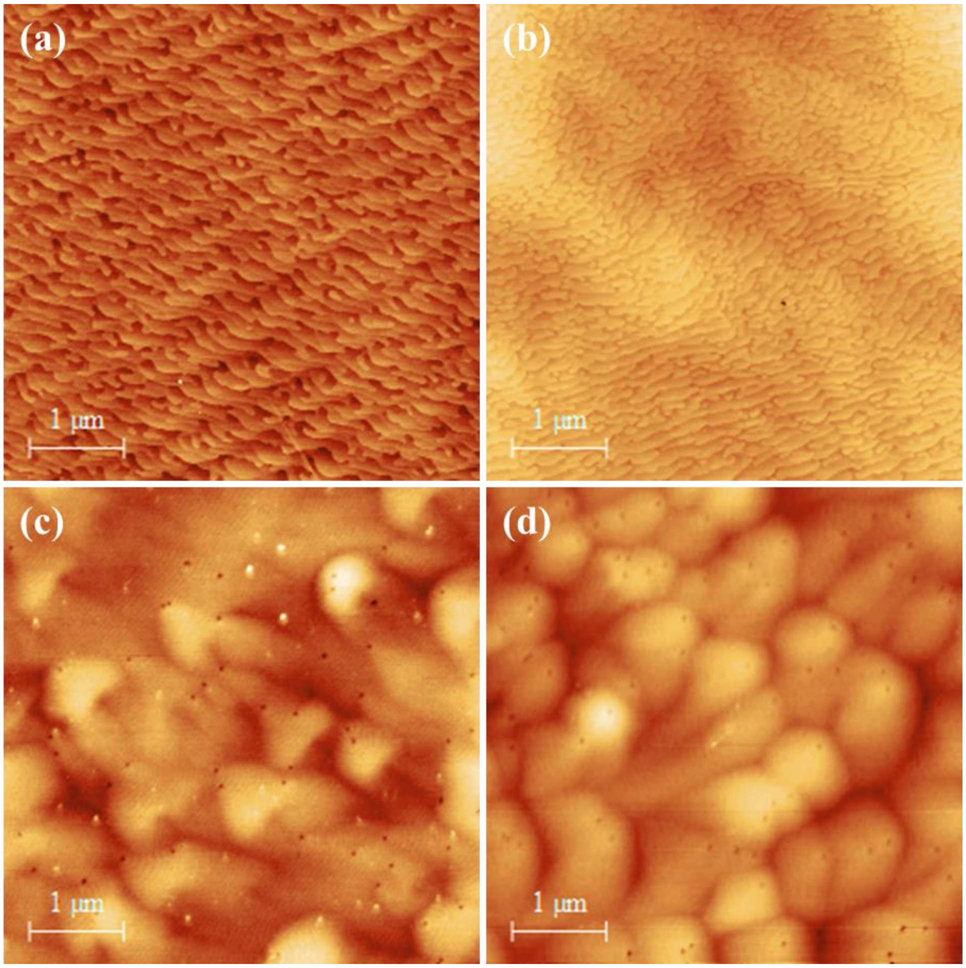

Figure 3.2 5 × 5 µm^2 AFM morphology images consist of (a) C1750 (x = 0.041), (b) C1236 (x = 0.095), (c) L532 (x = 0.13), and (d) L605 (x = 0.17).

Past x = 0.17 up to 0.25, the surface morphology of InGaN/GaN heterostructures changes tremendously. Figure 3.3 exhibits representative 5 × 5 µm^2 AFM images for (a) L597 (x = 0.181), (b) C1367 (x = 0.20) and (c) C1234 (x = 0.25). On top of GaN templates grown on sapphire, as shown in Figure 3.3 (a), the V-pits are always present, and their density is of ~3.0×10^8 cm^{-2} meaning that their density may not have been modified, as well as the average surface roughness which is now around 0.6 nm. The important difference with the above cases is the appearance of linear cross hatched network which make an approximate angle of 60°. In this sample, two families are clearly visible, the spacing between the linear features is irregular varying from

0.265 µm to 1.316 µm. Such features are determined to be along <1010> direction, they originate most probably from the formation of misfit dislocations as studied in reference [21] by cathodoluminescence.

The morphological evolution of the C-series of samples is very different. As can be seen in Figure 3.3 (b) for C1367 (x = 0.20) a high density of V-defects (~2.1×10^{9} cm^{-2}) is now present and this only took place inside the surface InGaN layer as the substrate has a very low density of threading dislocation. Moreover, the surface roughness has tremendously increased (~2.83 nm). The surface structure mainly consists of hillocks with approximate alignments, which probably means that, with increased indium content, the layer structure has been degraded and a three dimensional growth mode has been operating. Subsequently, when the nominal indium concentration is brought to 0.25, sample C1234 which has a similar InGaN thickness, appears to result from an even more pronounced 3D growth mode (Figure 3.3 (c)). In this instance, V-defects are no more visible; in contrast, the layer seems to be made of agglomerated small islands, which contribute to an increased surface roughness of ~7.04 nm. Moreover, the alignment of the island deposition along crystallographic directions is now obvious.

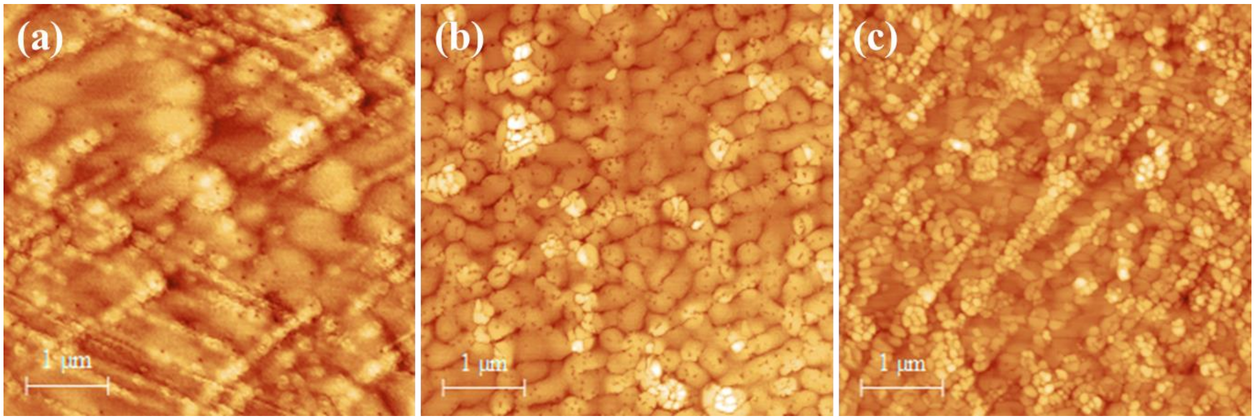

Figure 3.3 5 × 5 μm^2 AFM morphology images of (a) L597 (x = 0.181), (b) C1367 (x = 0.20), and (c) C1234 (x = 0.25).

3. 3. 2 Microstructural analysis

The samples have been extensively investigated by TEM first in the cross section geometry in order to address the formation of defects as well as the growth mode in relation with the indium composition. In the following, we first focus on the above samples with ($0.04 < x \leq 0.25$) and then we shall address those where the indium composition goes as high as 100%.

3. 3. 2. 1 Low and medium indium content InGaN layers

For the C-series with indium fraction below 10% of In content, as can be seen for C1236 (Figure 3.4), the layers exhibit very high crystalline quality, the surface of InGaN epilayer is flat and as expected from the quality of the free GaN substrate, no defects can be seen at this scale.

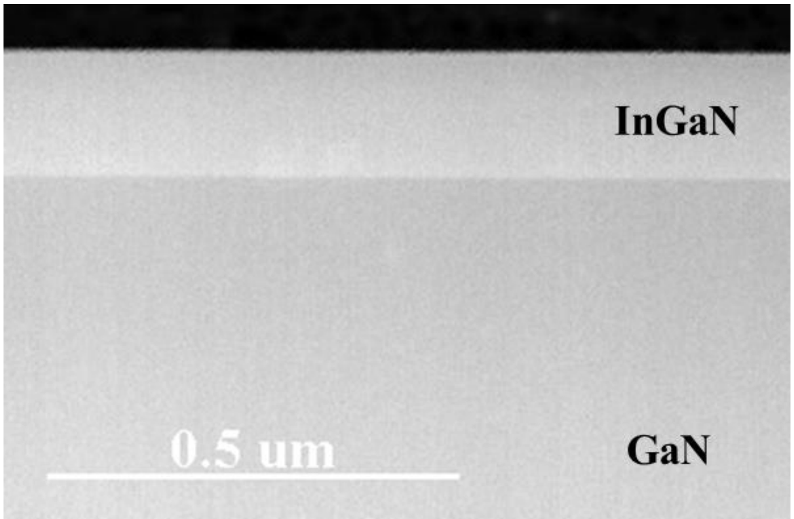

Figure 3.4 A typical low magnification STEM micrograph of C1236 ($x = 0.095$).

Previous reports have indicated that V-shape defects in III-N materials are connected to threading dislocations (TDs) and open up in the InGaN/GaN heterostuctures [22]. These TDs are of screw, edge and mixed type. However, it is not clear which type predominantly leads to the formation of the V-defects in the $In_xGa_{1-x}N$/GaN heterostructures. Therefore, one of our objectives is to determine any existing relationship of the TDs and other possible defects with the variation of In concentration using TEM.

For the above L532 (x = 0.13) and L605 (x = 0.17), it was shown above that their surface exhibit hillocks and V-pits. For instance sample L532 possesses a high density of TDs, as can be observed in Figure 3.5 (a) and (b), '***a + c***' TDs are all terminated by V-defects which systematically start at the InGaN/GaN interfaces. At these indium concentrations, it also can be seen that the surfaces of both InGaN layers are flat from diffraction vectors ***g*** = [10-10] and ***g*** = [0002], which means that the layers have grown in a 2D mode.

In Figure 3.5 (a), ***a***-type TDs are also present as inside this layer, as can be seen, such dislocations do not open up towards the surface as V-pits, instead, they slightly bend at the InGaN/GaN interface and then continue the way to the surface as inclined lines.

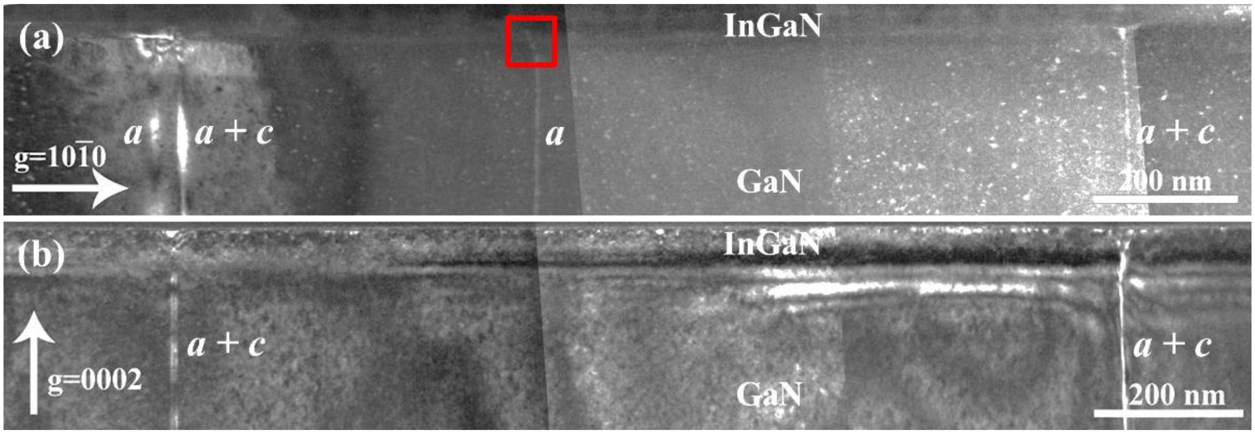

Figure 3.5 Cross-sectional dark field TEM images of L532 (x = 0.13) taken under weak beam diffraction conditions with (a) ***g*** = [10-10], and (b) ***g*** = [0002], the dislocation types have been marked.

When the indium concentration is increased above 18% (L571), as can be seen in Figure 3.6, the structure of the heterostructure contains many more defects than those that are related to the TDs. The ***a***-type TDs continue to give rise to the formation of V-defects at the layer surface. In the displayed weak beam images using diffraction vectors (a) ***g*** = [11-20], (b) ***g*** = [10-10], and (c) ***g*** = [0002], additional dislocations run from the InGaN/GaN interface to the surface (Figure 3.6 (a)). Such dislocations may be connected to misfit dislocations (MDs) (green boxes) which are visible in Figure 3.6 (b). In these samples the MDs do not seem to form a regular array as would be expected for a uniform plastic relaxation inside a strained interface. This in contrast to the case of cubic heterostructures such as SiGe/Si [23] and InGaAs/GaAs [24]. The analysis by diffraction contrast indicates that the MDs have a Burgers vector of ***a***. The non uniform distribution agrees with the above AFM observations of cross hatched which also are non-regularly space. Moreover, their occurrence along <10-10> type directions show that the MDs are of pure edge type and therefore relax a maximum of strain. As shown in Figure 3.6 (c), only residual contrast is visible, confirming the fact that the MDs are of edge type (red marks).

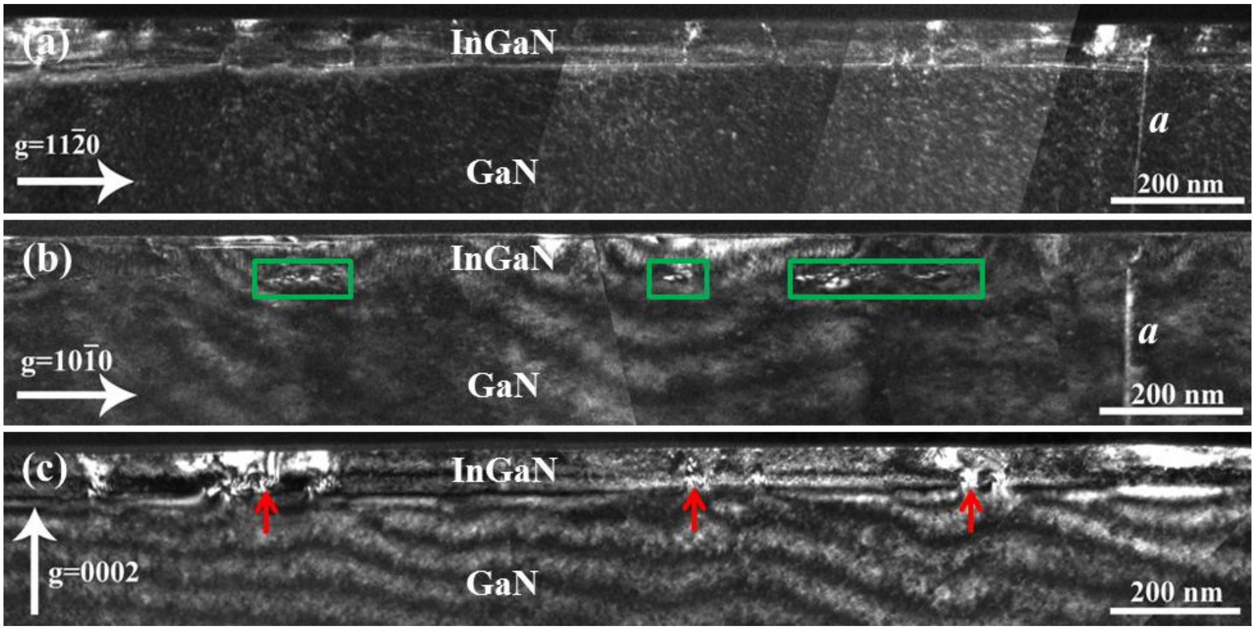

Figure 3.6 Cross-sectional dark field TEM images of L571 (x = 0.188) taken under weak beam diffraction conditions with (a) ***g*** = [11-20], (b) ***g*** = [10-10], and (c) ***g*** = [0002].

For sample C1367 (x = 0.20), the evolution of the microstructure in heterostructures grown on free standing GaN with the increase of indium concentration is extremely interesting. In Figure 3.7, as can be seen, the weak beam image with ***g*** = [11-20] (Figure 3.7 (a)) shows on the left one ***a***-type dislocation going from the interface and opening at the surface, which agrees with the high density of V-defects as observed by AFM. This is confirmed with ***g*** = [10-10] (Figure 3.7 (b)) where four V-defects can be clearly seen in the same area, among which three are generated inside the InGaN layer, as they are not attached to any dislocation. As the ***g*** = [0002] image is only displaying residual contrast, we can conclude that all the defects that are present in this area correspond to ***a***-type dislocations.

In Figure 3.7 (b), as shown in the green rectangles, MDs can be seen at the InGaN/GaN interface, and the MD lines along <10-10> directions have unhomogeneous distribution, which can be further determined by plan-view TEM images in Chapter 5. In the meanwhile, the MDs have a Burgers vector of ***a***. Like L571 (x = 0.188), in order to determine if MDs have ***c***-component, we also give here diffraction vector ***g*** = [0002], as exhibited in Figure 3.7 (c). We can make sure that MDs have no ***c***-component from the image. However, we observed a few bright parts as indicated by the red arrows, this phenomenon is also resulting from residual contrast. This is the case especially inside the interface where a number of ***a***-type misfit dislocations are visible in Figure 3.7 (b) (green boxes) and more are underlined with the residual contrast in Figure 3.7 (c). As can be seen in Figure 3.7 (a), the strain in the InGaN layer has started to relax by the generation of ***a***-type dislocation half loops, which do not reach the interface. As pointed out in AFM, at this indium concentration, the surface roughness has also been compromised due to this strain relaxation, this is clearly visible in Figure 3.7 (b) with ***g*** = [10-10], which not only points out the present defects, but underlines the surface morphology.

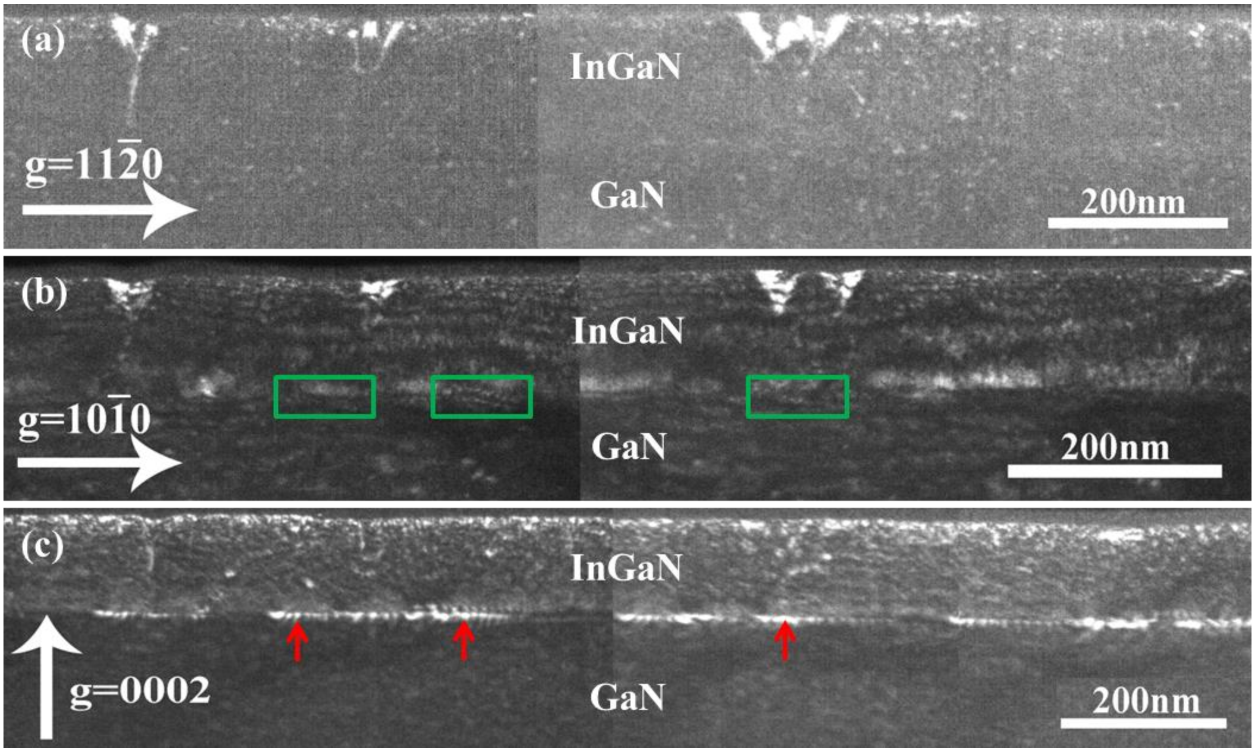

Figure 3.7 Cross-sectional dark field TEM images of C1367 (x = 0.20) taken under weak beam diffraction conditions with (a) ***g*** = [11-20], (b) ***g*** = [10-10], and (c) ***g*** = [0002].

This is even more obvious in sample C1234 where the nominal indium composition was intended to be 25%. In agreement to the large surface roughness (7 nm) which was pointed out in AFM, the InGaN layer appears to have grown in a 3D mode, as can be seen in Figure 3.8, and the local depth of the V-defects is more than the value given by AFM. Moreover, the local structure is more complicated as revealed in this weak beam image recorded with ***g*** = [10-10]. In this area, the MD (see green box) is clearly connected a TD which does not travel to the layer surface in a straight way. Instead, its line ends up in the basal plane connecting to large V-defect (V1). This area exhibits three V-defects (V1-V3) which are seen to contribute to the layer surface roughness, at their base, the stacking sequence of the InGaN is disrupted in a thickness of about 10 nm (see yellow box). Moreover, as can be noticed, the image contrast is quite uniform from the InGaN/GaN interface to the level where the disrupted sequences are located, then towards the surface, there are large changes of contrast in the area with the V-defects. Such changes in the weak beam images could be due to the change in local strain state (orientation, composition, etc.).

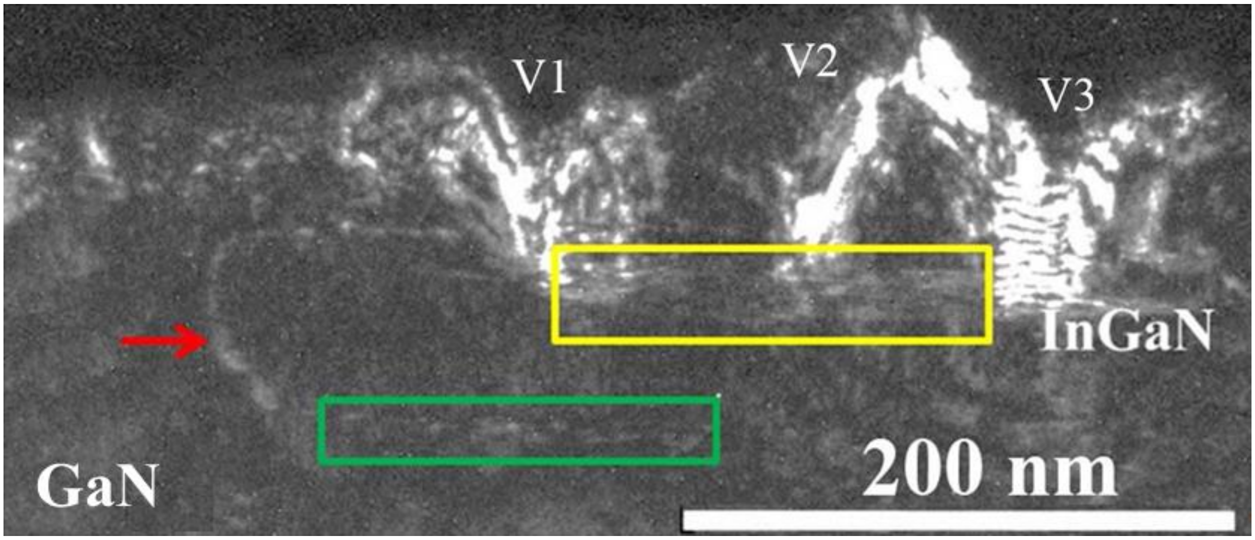

Figure 3.8 The weak beam dark field cross-sectional TEM image of C1234 (x = 0.25) taken under diffraction vector ***g*** = [10-10], misfit dislocation (green box), threading dislocation (red arrow) and a series of stacking faults (yellow box) connecting three V defects.

In order to determine the origin of the strong variation in the image contrast we measured the local indium composition by Energy Dispersive X-ray Spectroscopy (EDS) as shown in Figure 3.9. Going from the GaN template to the alloy surface, the indium concentration is largely different from the intended average nominal value of 25%. Instead, it clearly increases from below this nominal value close to the interface (15-18%) to almost 40% at the surface.

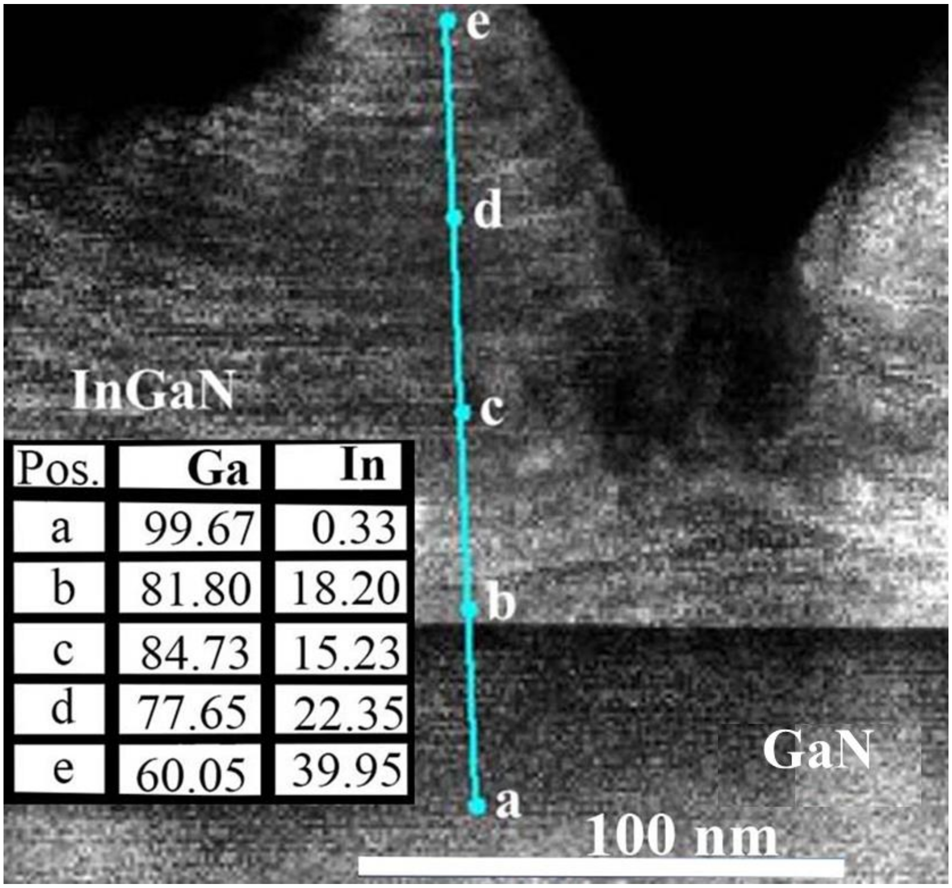

Pos.	Ga	In
a	99.67	0.33
b	81.80	18.20
c	84.73	15.23
d	77.65	22.35
e	60.05	39.95

Figure 3.9 Indium composition measured by EDS, from the interface to the surface in sample C1234, the probe positions are shown as letters (a-e), the inset table exhibits the local composition at the corresponding positions.

3. 3. 2. 2 High indium content InGaN layers

To further understand the growth of InGaN on GaN at higher indium contents we carried out X-ray diffraction (XRD) ω-2θ scans, as shown in Figure 3.10, for a series of high In-content InGaN/GaN heterostructures L598 ($x = 0.20$), L648 ($x = 0.40$), L645 ($x = 0.62$), L644 ($x = 0.765$), L587 ($x = 0.825$), and L642 ($x = 1$). As can be seen, the (0002) peak widens strongly in the intermediate range of indium composition meaning that it is the growth of the alloys itself which leads to the degradation of the crystalline quality of the layers by MOVPE. Indeed, in the same process, the layer quality is well improved when InN is deposited on GaN, although the lattice mismatch is the highest (11.3%).

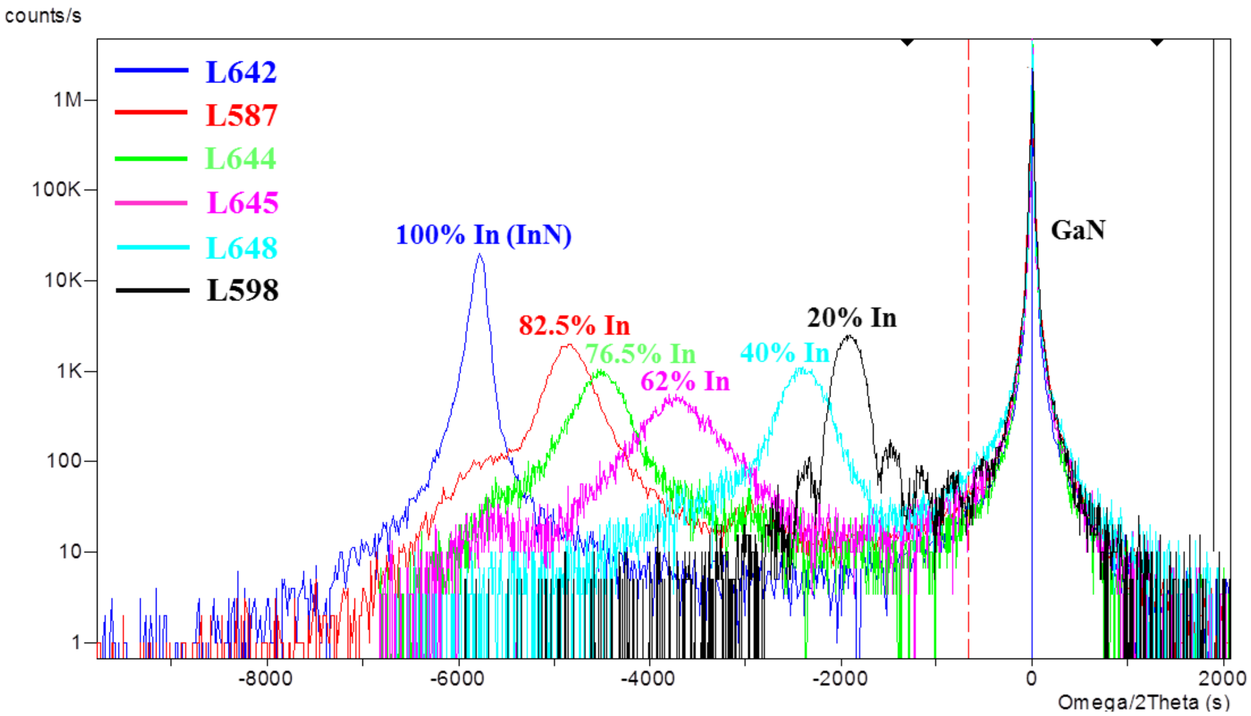

Figure 3.10 The XRD spectra of $In_xGa_{1-x}N$/GaN heterostructures ($0.20 \le x \le 1$).

Subsequently, we carried out TEM images of the four high In-content InGaN/GaN heterostructures with the indium content above C1234, these are L648 ($x = 0.40$), L645 ($x = 0.62$), L587 ($x = 0.825$), and L642 ($x = 1$), respectively. Figure 3.11 (a-c) exhibit bright field TEM images of these samples. As already pointed out in samples C1234 grown on free standing GaN, the first characteristic feature of these indium rich layer is the large surface roughness. The other new common feature is the formation of voids inside the layers, and more particularly at the interface with GaN for all of them. The voids do not have particular shapes for In = 40% (Figure 3.11 (a)) and they are distributed all over the layer which exhibits the lowest quality for In = 62% (Figure 3.11 (b)). They are mainly elongated parallel to the interface for In = 82.5% (Figure 3.11 (c)), and for InN in which the best quality is attained in agreement with the XRD measurement, the voids at the interface are the smallest. We have a 3D growth for all these layers, but in this instance, all the islands are of very good crystalline quality (Figure 3.11 (d)).

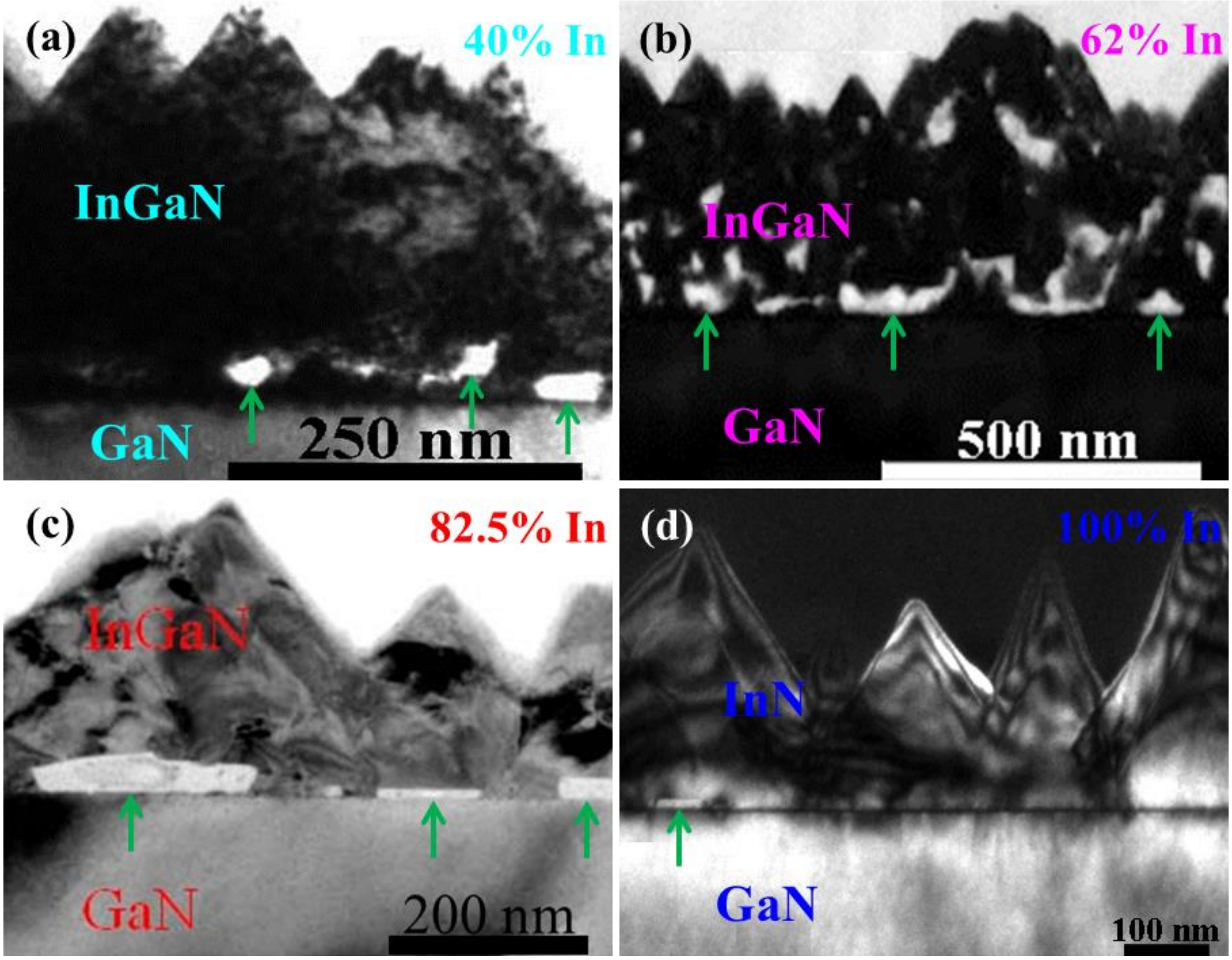

Figure 3.11 Bright field images of (a) L648 ($x = 0.40$), (b) L645 ($x = 0.62$), and (c) L587 ($x = 0.825$). Dark field image of (d) L642 ($x = 1$) taken under two beam diffraction condition with $\boldsymbol{g}$ = [0002].

3. 4 Summary and conclusions

In this chapter, we investigated the $In_xGa_{1-x}N$/GaN heterostructures grown by MOVPE in the range of 0.04 to 1. In this range, the lattice mismatch varies from 0.4% to 11.3%, which mostly would be expected to rapidly lead to the formation of interface MDs above a 1.5% value. The surface morphologies of the low In-concentration InGaN epilayers were investigated by AFM, it is shown that the surface morphology and the roughness are significantly different depending on In concentration. For $x < 0.13$, step-terrace morphology with a very low density of V-pits was observed especially in our layer which had been grown on free standing GaN substrates where the density of residual dislocations is below 10^6 cm^{-2}. Surface morphologies consist of hillocks and V-pits for $0.13 \leq x \leq 0.188$, however, for $x \geq 0.18$, we also observed a cross-hatch pattern, which leads to a roughness of up to 0.83 nm. Above $x = 0.20$, a granular morphology covers the surfaces, however, for $x = 0.25$, formation of growth grains, with an increase of the surface roughness from 2.83 nm to 7.04 nm.

We further studied the microstructure of the samples by TEM diffraction contrast. The results show that there are not any dislocations in the InGaN/GaN heterostructures for the lowest In concentration. For $0.13 \leq x \leq 0.25$, both the TDs and the V-shaped defects can be seen in the heterostructures, MDs were also observed when In concentration is more than 0.18 and the alloys exhibit a strong 3D growth with large V defects and stacking disruption for $x = 0.25$ and beyond. For the highest In concentration ($x \geq 0.40$), XRD, in complete agreement with the TEM observations, indicates a strong crystalline quality degradation of InGaN layers grown by MOVPE, which is the highest at $x = 0.62$. When InN is grown directly on GaN, a substantially good crystalline quality can be attained, although the high lattice mismatch results in small voids formation at the interface as well as 3D growth.

References

[1] S. Nakamura, T. Mukai, and M. Senoh, Appl. Phys. Lett., 64, 1687 (1994).

[2] F. A. Ponce, and D. P. Bour, Nature, 386 , 351 (1997).

[3] J. Wu, W. Walukiewicz, K. M. Yu et al., J. Appl. Phys., 94, 6477 (2003).

[4] O. Jani, I. Ferguson, C. Honsberg, and S. Kurtz, Appl. Phys. Lett., 91, 132117 (2007).

[5] S. Nakamura, S. Pearton, and G. Fasol, Emission Mecha-nisms of LEDs and LDs, The blue laser diode (Springer, Berlin, 2000), p. 279.

[6] I. Ho, and G. B. Stringfellow, Appl. Phys. Lett., 69, 2701 (1996).

[7] S. Y. Karpov, N. I. Podolskaya, I. A. Zhmakin, and A. I. Zhmakin, Phys. Rev. B, 70, 235203 (2004).

[8] T. Takayama, M. Yuri, K. Itoh, and J. S. Harris, J. Appl. Phys., 90, 2358 (2001).

[9] T. Matsuoka, Appl. Phys. Lett., 71, 105 (1997).

[10] P. Ruterana et al., Appl. Phys. Lett. 72, 1742 (1998).

[11] S. Pereira, M. R. Correia, E. Pereira, et al., Phys. Rev. B, 64, 205311 (2001).

[12] M. Hao, H. Ishikawa, T. Egawa et al., Appl. Phys. Lett., 82, 4702 (2003).

[13] D. Doppalapudi, S. N. Basu, K. F. Ludwig, and T. D. Moustakas, J. Appl. Phys. 84, 1389 (1998).

[14] R. Singh, D. Doppalapudi, T. D. Moustakas, and L. T. Romano, Appl. Phys. Lett. 70, 1089 (1997).

[15] Y. T. Moon, D. J. Kim, J. S. Park et al., Appl. Phys. Lett., 79, 599 (2001).

[16] Y. Narukawa, Y. Kawakami, M. Funato et al., Appl. Phys. Lett., 70, 981 (1997).

[17] K. P. O’Donnell, R. W. Martin, and P. G. Middleton, Phys. Rev. Lett., 82, 237 (1999).

[18] P. Ruterana, S. Kret, A. Vivet et al., J. Appl. Phys., 91, 8979 (2002).

[19] H. Lei, J. Chen, and P. Ruterana, Appl. Phys. Lett., 96, 161901 (2010).

[20] F. G. McIntosh, K. S. Boutros, J. C. Roberts, S. M. Bedair, E. L. Piner, and N. A. El-Masry, Appl. Phys. Lett. 68, 40 (1996).

[21] S. Srinivasan, L. Geng, R. Liu, F. A. Ponce, Y. Narukawa, and S. Tanaka, Appl. Phys. Let. 83, 5187 (2003).

[22] M. Shiojiri, C. C. Chuo, J. T. Hsu, J. R. Yang, and H. Saijo, J. Appl. Phys. 99, 073505 (2006).

[23] R. Hull, and J. C. Bean, Appl. Phys. Lett. 54, 925 (1989).

[24] J. M. Bolnar, R. Hull, J. F. Walker, and R. Malik, Appl. Phys. Lett. 60, 1327 (1992).

Chapter 4

Plasma Assisted Molecular Beam Epitaxy of In-rich InGaN/GaN heterostructures

4. 1 Introduction

Taking into account the tunable direct band gap of InGaN alloys, extending the emission to longer wavelengths has been proposed as a potential solution for double-junction tandem solar cells based on III-V materials on silicon [1], with a predicted efficiency limit of 39% under 1 sun and of 42.3% under solar concentration (500 suns). One advantage for device processing is that III-nitrides are similar to silicon in terms of thermal coefficients, which means that the development of a joint InGaN-on-silicon technology could be set up. Indeed, the fabrication of such photovoltaic devices requires a high-quality InGaN junction with an In mole fraction around 30%. However, the synthesis of high-quality high-In-concentration InGaN films is challenging due to the lattice mismatch between InN and GaN (~11%), the composition instabilities over a wide range of indium concentration [2], the relatively high vapor pressure of InN as compared to GaN leading to low indium incorporation [3], and the difference in formation enthalpies for InN and GaN which causes a strong indium segregation on the growth front [4].

In comparison to the MOVPE as seen in chapter 3, Plasma Assisted Molecular Beam Epitaxy (PAMBE) also request deeper investigation as it may operate at lower temperatures and far from the thermodynamic equilibrium and as such it could be expected to allow the synthesis of InGaN in the entire alloy compositional range with layers of better crystalline quality. PAMBE growth of InGaN has been reported following various approaches. Gacevic et al. [5] presented a growth diagram of InGaN with In concentration up to 50% and identified an intermediate metal-rich regime, with 1-2 monolayer thick In adsorption coverage, which provided best InGaN quality in terms of surface morphology.

In this chapter, we investigate the surface morphology and the microstructure of a series of

InGaN/GaN heterostructures with varying thickness of InGaN layers from 7 nm to 500 nm grown by PAMBE using AFM and TEM, and try to address the interplay between In incorporation and strain relaxation. Our interest was to analyze the evolution of the surface morphology and the microstructure versus the thickness in order to pinpoint the dominant mechanism of strain relaxation.

4. 2 PAMBE growth of InGaN layers

The investigated InGaN epilayers were deposited at varying thickness from 7 nm to 500 nm grown on 4-μm-thick GaN/ (0001) sapphire substrates by PAMBE, as shown in Figure 4.1.

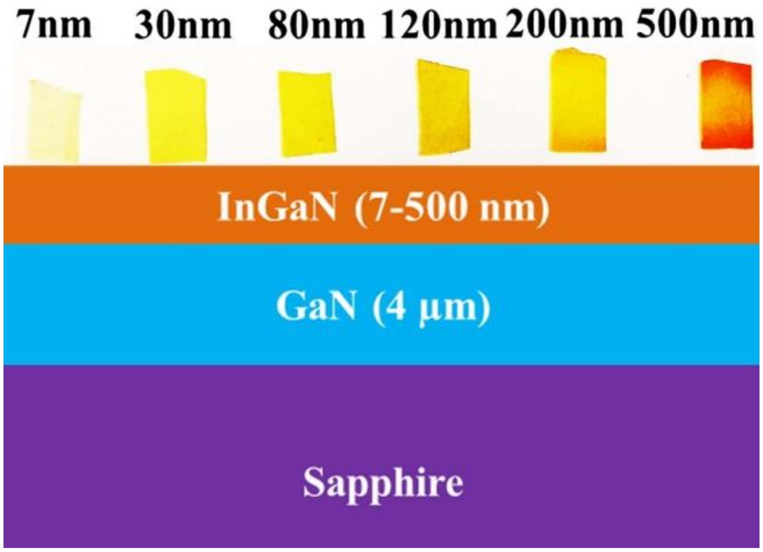

Figure 4.1 The optical images of the 6 samples under investigation along with a schematic layout of the heterostructures.

During the InGaN growth, the active nitrogen flux was fixed at 0.38 ML/s, and the InGaN growth temperature was 670 °C. The growth was monitored in situ by Reflection High Energy Electron Diffraction. For all the layers, the nominal In composition was ~30% as determined by high resolution X-ray diffraction, which leads to a mean lattice mismatch of ~3.4%. As can be seen, the color of the samples goes from almost transparent to quite red which may have a direct relationship with the indium content which thus could be varying from one sample to the next.

The investigated samples are listed in Table 4.1, along with their nominal characteristics such as the layer thickness and the surface roughness.

Table 4.1 The investigated samples, thickness and roughness.

Sample	**Thickness (nm)**	**Roughness (nm)**
E3137	7	0.58
E3139	30	0.61
E3135	80	1.03
E3136	120	1.55
E3138	200	1.72
E3134	500	3.02

4. 3 The surface morphology

We first investigated the surface morphology of all the samples and Figure 4.2 displays that corresponding 10 × 10 μm^2 representative AFM images. As can be seen in Figure 4.2 (a) for the layer E3137 of 7 nm nominal thickness for InGaN, the surface exhibits many step-terraces and a quite low roughness of 0.58 nm. However small particles which may be hillocks or indium droplets are also present at this surface and very few dark spots could also be pinholes. When InGaN thickness is up to 30 nm (E3139), as shown in Figure 4.2 (b), in comparison with the above morphology, its surface structure is different, it exhibits a smoother surface morphology with mainly well identified hillocks, and more pinholes can be observed over the surface. The surface roughness of the sample is ~0.61 nm, which is slightly larger than that of E3137.

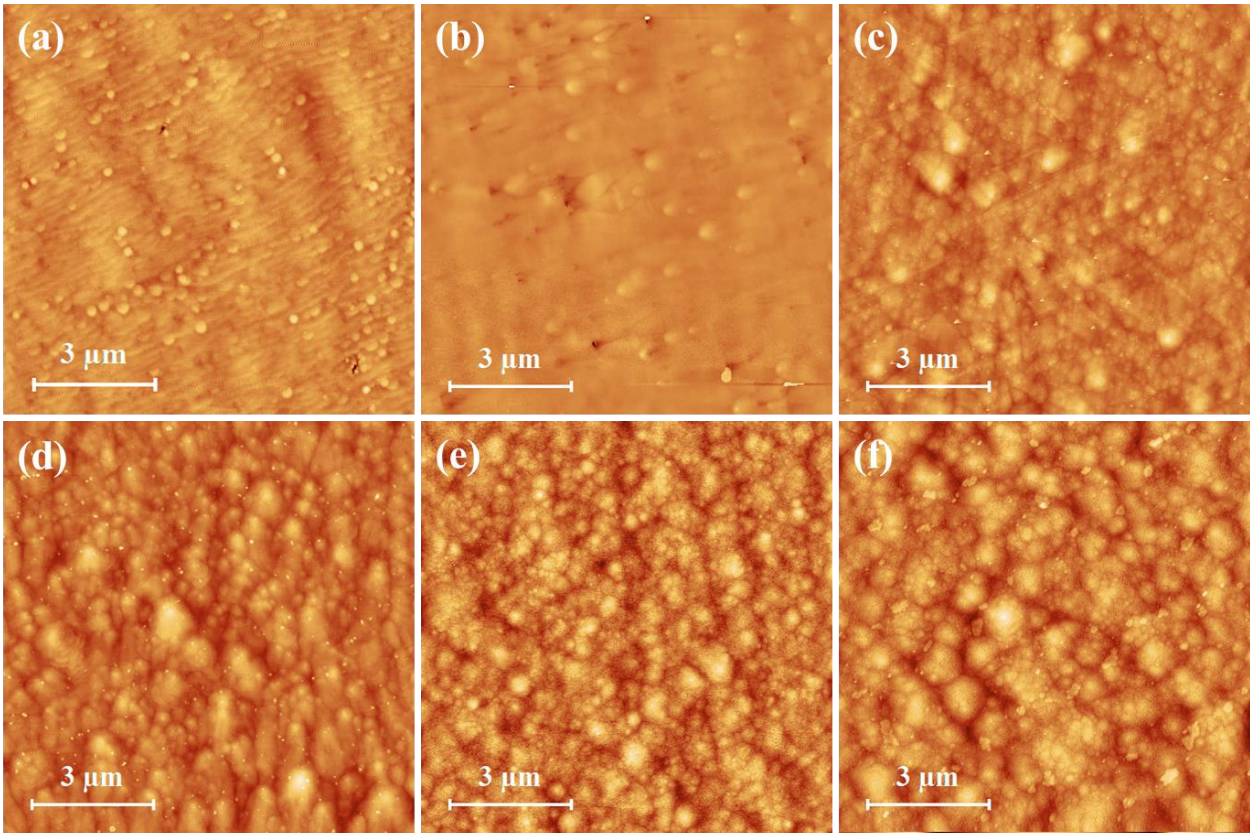

Figure 4.2 10 × 10 μm^2 AFM morphology images of the studied samples (a) E3137 (7 nm), (b) E3139 (30 nm), (c) E3135 (80 nm), (d) E3136 (120 nm), (e) E3138 (200 nm), and (f) E3134 (500 nm).

From 30 nm to 80 nm (E3135), the evolution of the surface morphology with increasing layer thickness is striking (Figure 4.2 (c)), the surface morphology is now dominated by hillocks. Moreover, this structure now coexists with cross-hatch pattern of faint elongated lines with apparent hexagonal symmetry. It is worth noting that, there are no more pinholes at this layer thickness. The average roughness of this sample is ~1.03 nm. When the layer thickness is increases past 100 nm, the surface morphology is even more dominated by a distribution of hillocks as can be seen in Figure 4.2 (d) (E3136 120 nm) which becomes more and more non uniform (Figure 4.2 (e)) in size as the InGaN nominal thickness is increased to the maximum of 500 nm (Figure 4.2 (f)). The direct effect is the increase in the surface roughness which tops up at a value of 3.02 nm for sample E3134 which is more than 6 times than that of the thinnest layer E3137.

4. 4 The microstructure analysis

The above six samples have been investigated by TEM in the cross section in order to determine the microstructure versus the increase in thickness and the possible ways for the relaxation of the quite large misfit strain in these layers where the nominal indium composition was intended to be around 30 %.

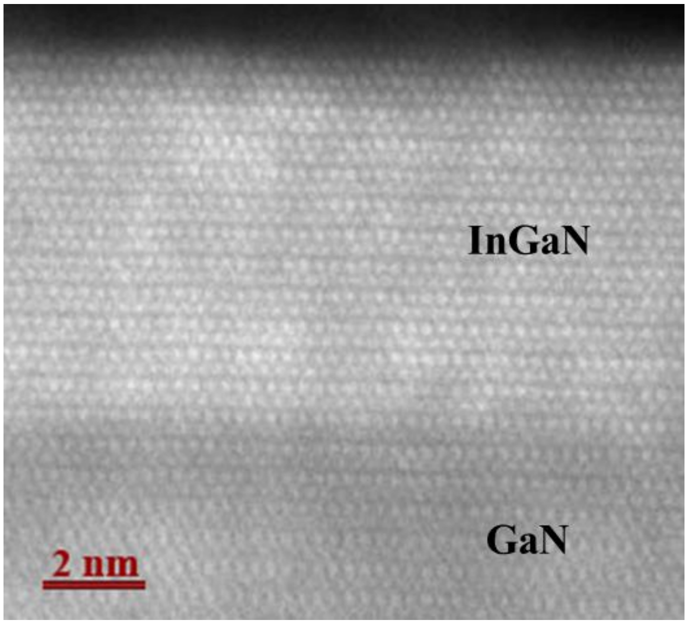

Figure 4.3 The high resolution STEM HAADF image shows the high crystalline quality of InGaN layer of E3137 (7 nm).

For the smallest thickness sample E3137, it was not possible to characterize it by conventional transmission electron microscopy, therefore we studied it by high resolution STEM High Angle Annular Dark Field (HAADF) with atomic resolution imaging. As can be seen in Figure 4.3, the InGaN layer thickness is 7.2 nm, which identical to the nominal value. Moreover, no defects are observed in the InGaN/GaN interface, which is a strong indication that the InGaN layer is elastically strained on the underlying GaN template.

Although the InGaN layer appears to exhibit a good crystalline quality, it is interesting to determine if its composition has any direct relationship which the intended indium content of 30%, therefore we systematically carried out EDS analysis. Due to the small thickness of sample 3137, we acquired spectra as shown in Figure 4.4, going from the GaN template to the InGaN layer surface. As can be seen the indium composition is not uniform, thus we measured 22%, 16%, 35% and 22% indium at probe positions 2 to 5, which shows that the composition is not uniform inside the InGaN layer.

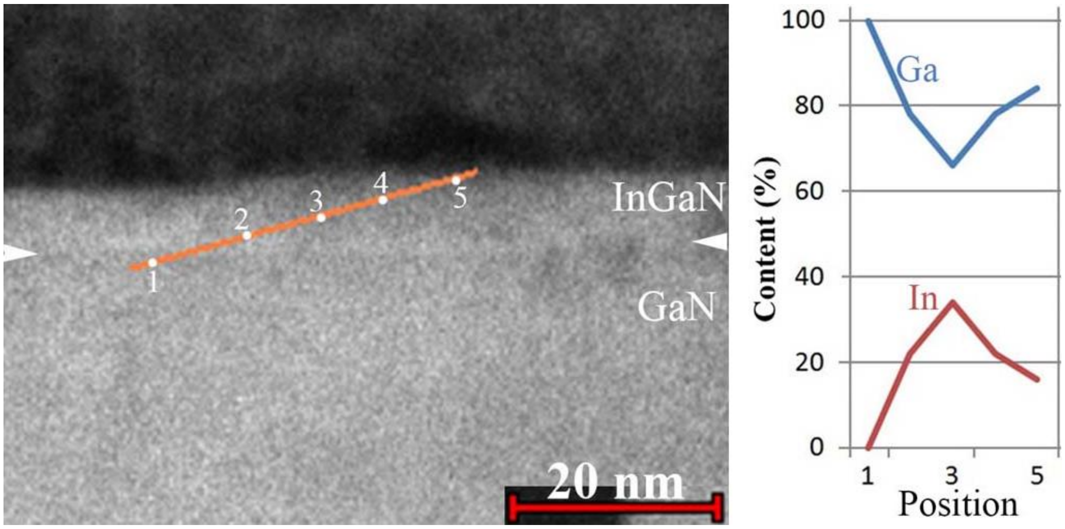

Figure 4.4 EDS analysis of samples E3137, the probe position for spectra acquisition are shown by white dots, the corresponding composition is also exhibited going from GaN to the layer surface.

When the thickness of the InGaN layer increases to 30 nm (E3139), a large number of defects forms starting in the interfacial area and propagating inside the InGaN layer. As shown in the dark field images of Figure 4.5 (a) recorded with ***g*** = [10-10], such defects are either stacking faults, or dislocations with an ***a*** component as they are not visible in Figure 4.5 (b) taken with ***g*** = [0002]. As can be seen inside the green rectangles, the strain is mainly spread in the vicinity of the InGaN interface, however some localized offshoot take place in the pyramidal plane as indicated by the red arrows.

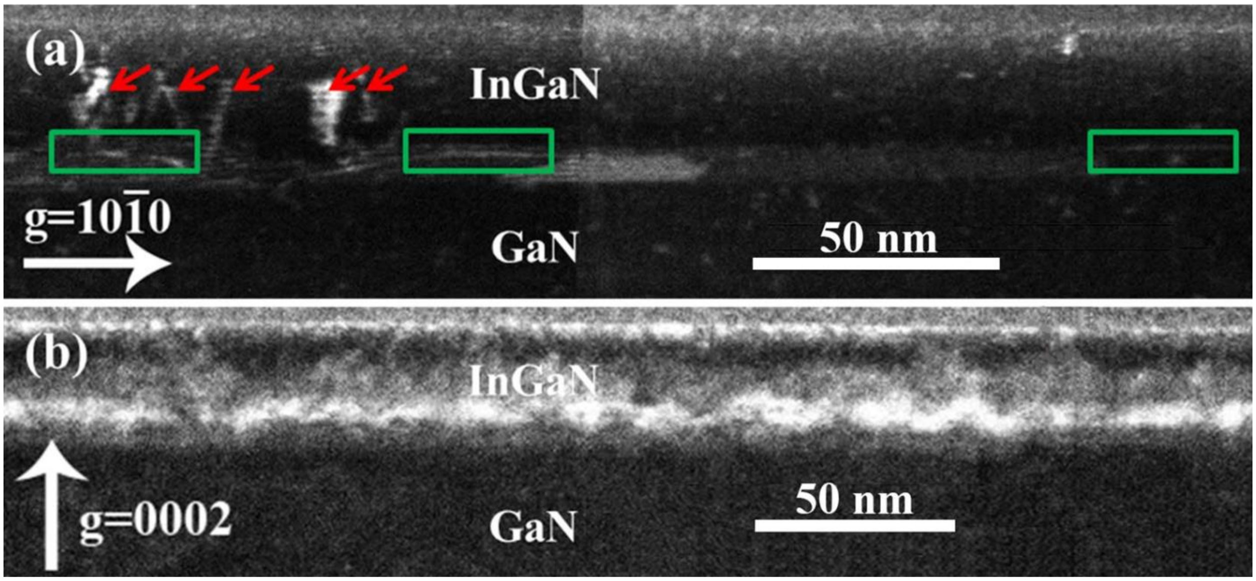

Figure 4.5 Cross-sectional dark field TEM images of E3139 (30 nm) taken under weak beam diffraction conditions with (a) ***g*** = [10-10], and (b) ***g*** = [0002].

In this case, the composition was also analyzed by EDS in the STEM and Figure 4.6 shows a dotted profile along the growth direction of this layer. Again the measured composition fluctuates quite a lot going from 10% to 30% along the 9 positions. Interestingly, the projected image of this layer does not show a noticeable roughness.

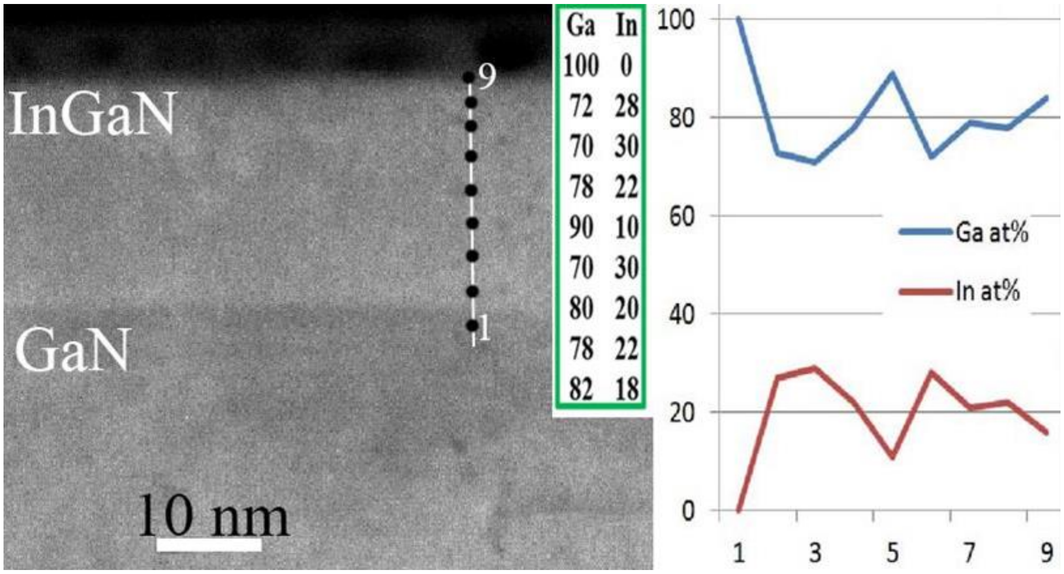

Ga	In
100	0
72	28
70	30
78	22
90	10
70	30
80	20
78	22
82	18

Figure 4.6 E3139 STEM image showing the positions for EDS analysis, the quantitative In composition as well as the corresponding chemical profiles of Ga and In.

The increase of the layer thickness to 80 nm generates new important defects in the GaN interface as well as inside the InGaN layer, as can be seen in Figure 4.7. The two weak beam images ((a) with ***g*** = [10-10], and (b) with ***g*** = [0002]) show clearly the misfit dislocations inside the InGaN/GaN interface. The second type of defect that is stacking faults which show up as horizontal features inside the basal planes (see yellow box). Most interestingly, new features are now present, they are pyramidal half loops which are coming from the surface of InGaN and probably aiming to go to the interface (see blue boxes). As these half loops are visible in both images they have ***a*** and ***c*** components.

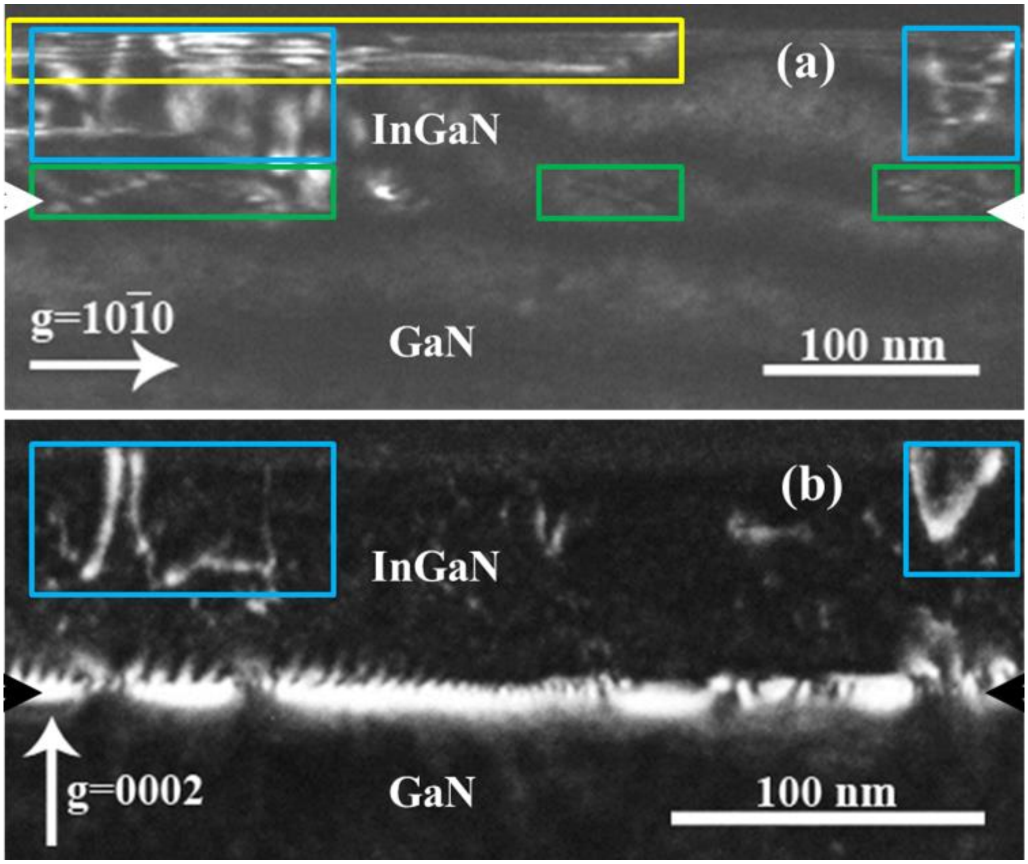

Figure 4.7 Cross-sectional dark field TEM images of E3135 (80 nm) taken under weak beam diffraction conditions with (a) ***g*** = [10-10], and (b) ***g*** = [0002]. The InGaN/GaN interface is marked by white arrows in (a), and black arrows in (b).

This is clearly confirmed at the thickness of 120 nm (E3136), indeed as can be seen in Figure 4.8, the misfit dislocations have clearly settled at the InGaN interface (green rectangles) and the stacking faults are now of high density towards the surface of the layer (yellow rectangles). Above all, the '**a** + **c**' half loops (blue rectangles) have now been generated all over the layer and they almost reach the interface, therefore constituting one of the predominant mechanisms which become available for the strain relaxation inside these layers.

Still, as can be seen in Figure 4.9, the indium composition in the InGaN layer fluctuates with amplitudes of more than 10% without a clear trend along the growth direction.

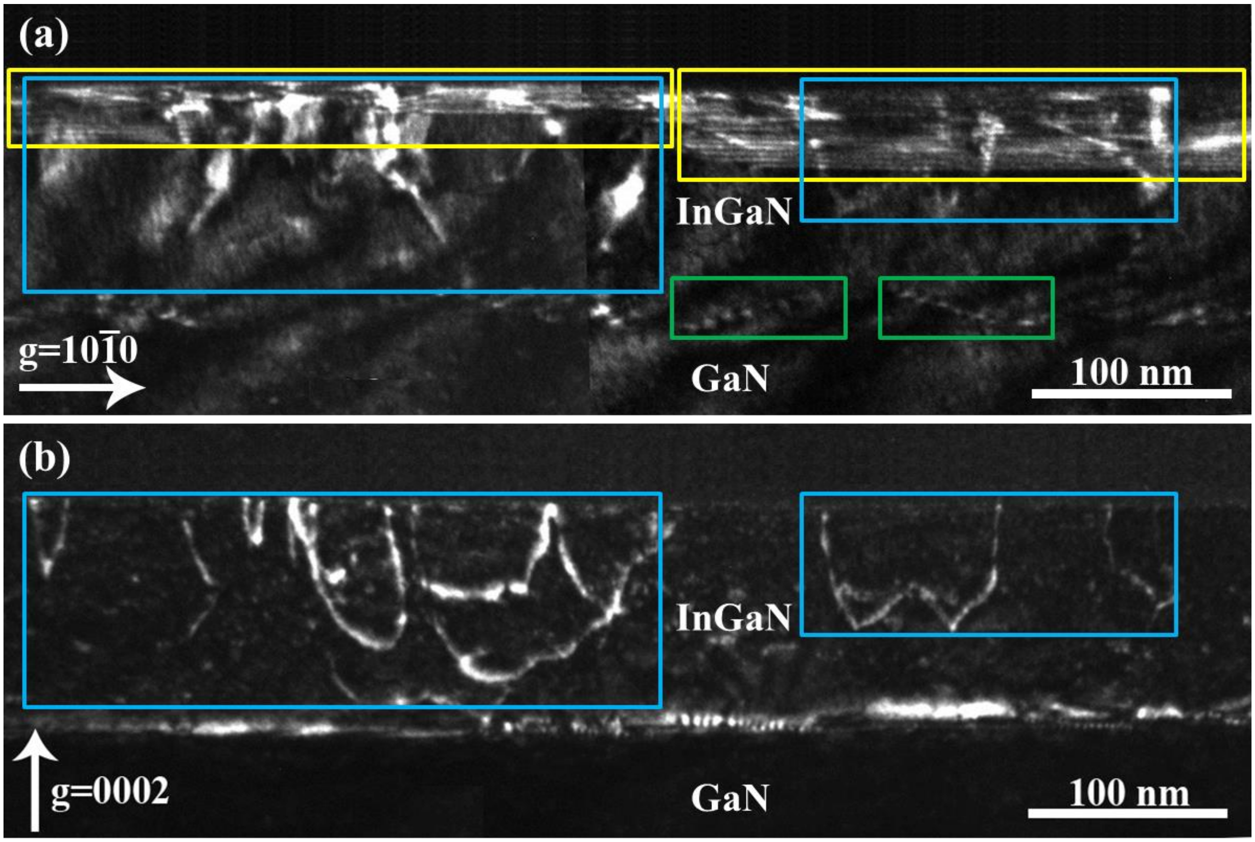

Figure 4.8 Cross-sectional dark field TEM images of E3136 (120 nm) taken under weak beam diffraction conditions with (a) ***g*** = [10-10], and (b) ***g*** = [0002].

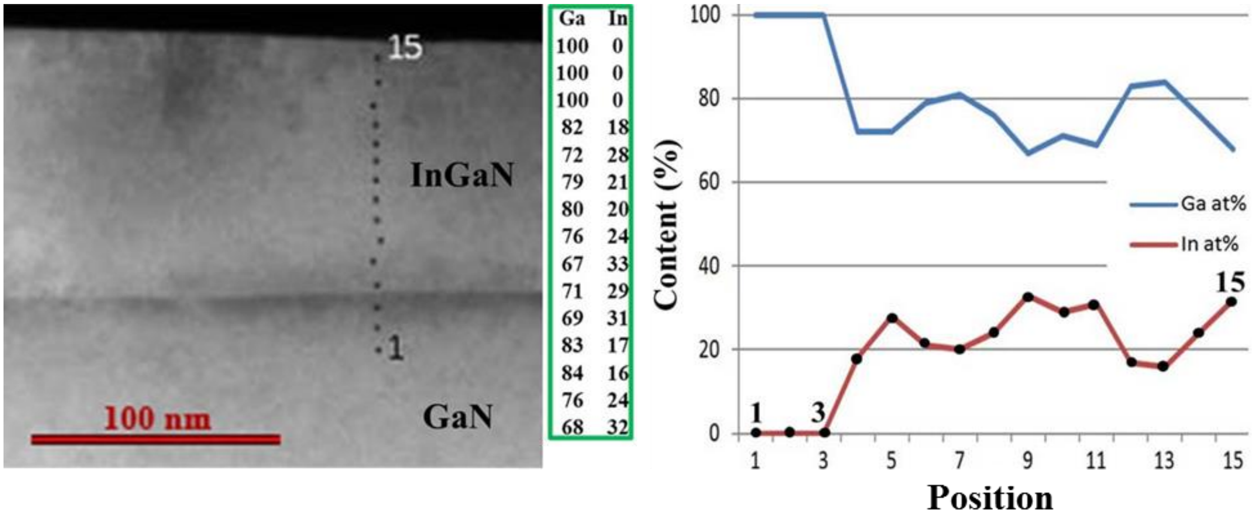

Ga	In
100	0
100	0
100	0
82	18
72	28
79	21
80	20
76	24
67	33
71	29
69	31
83	17
84	16
76	24
68	32

Figure 4.9 The HAADF image of E3136 showing probe positions for EDS analysis, along with the corresponding composition and profile.

Within the two thickest layers, the above microstructural features are completely settled and reproduced which means that the possible strain relaxation mechanisms during this PAMBE growth involves three predominant mechanisms: (1) the formation of misfit dislocations, which could be pure ***a*** type edge dislocations; (2) the glide of '***a*** + ***c***' type dislocations from the surface to the interface to contribute to a further relaxation of the misfit strain; (3) the generation of stacking faults which accumulate toward the top of the InGaN layer. Moreover, it seems that when the growth is carried out for larger thickness, not only the microstructures become well established, but the indium distribution attains some equilibrium. We discuss the case of the thickest sample (E3134, 500 nm), but this is also valid for sample E3138 (200 nm). From EDS analysis, as can be seen in Figure 4.10, the indium composition is not random, but almost gradually increases from the interface to a maximum at the surface.

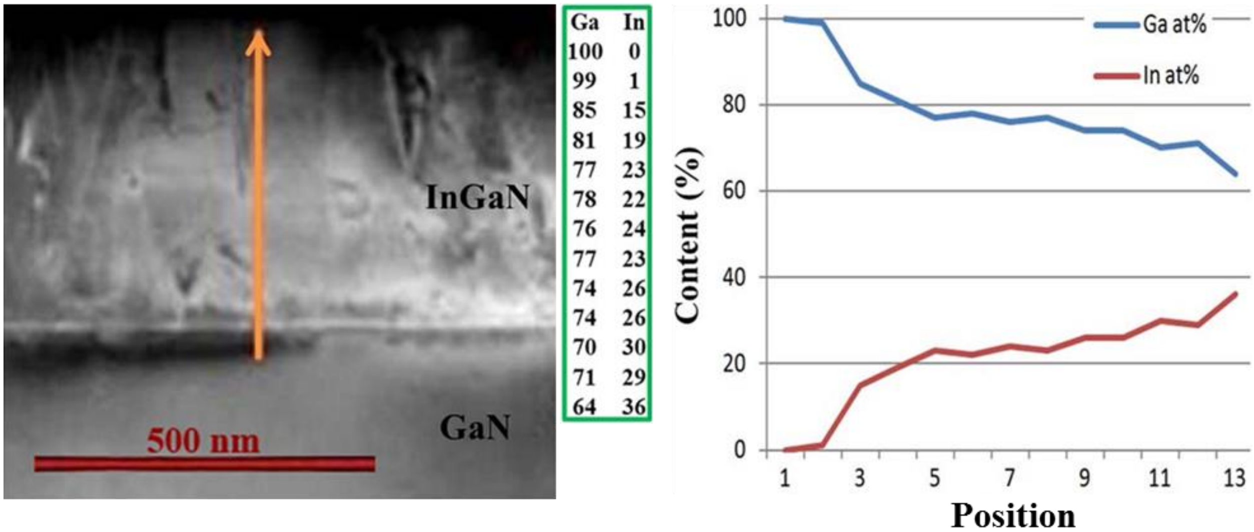

Ga	In
100	0
99	1
85	15
81	19
77	23
78	22
76	24
77	23
74	26
74	26
70	30
71	29
64	36

Figure 4.10 HAADF image of E3134 recorded during EDS acquisition along the growth direction at 13 probe positions, with the corresponding concentration of Ga and In, and the composition profile.

The structural relaxation process is clearly underlined in Figure 4.11, the interfacial ***a*** type misfit dislocations are clearly pointed out in Figure 4.11 (a) recorded with ***g*** = [10-10] along with the mixed type threading dislocations and the stacking faults. Interestingly, the stacking faults and much of the contrast due to the interfacial misfit dislocations disappear in the Figure 4.11 (b) recorded with ***g*** = [0002]. This allows noticing the dislocations that have already reached the interface in order to release the misfit strain, and those which are still in the form of half loops. Moreover, the two figures show that the formation of the stacking faults takes place all along the growth, and that as can be seen in Figure 4.11 (a), the formation of the highest density stacking faults is irregularly set up towards the layer surface.

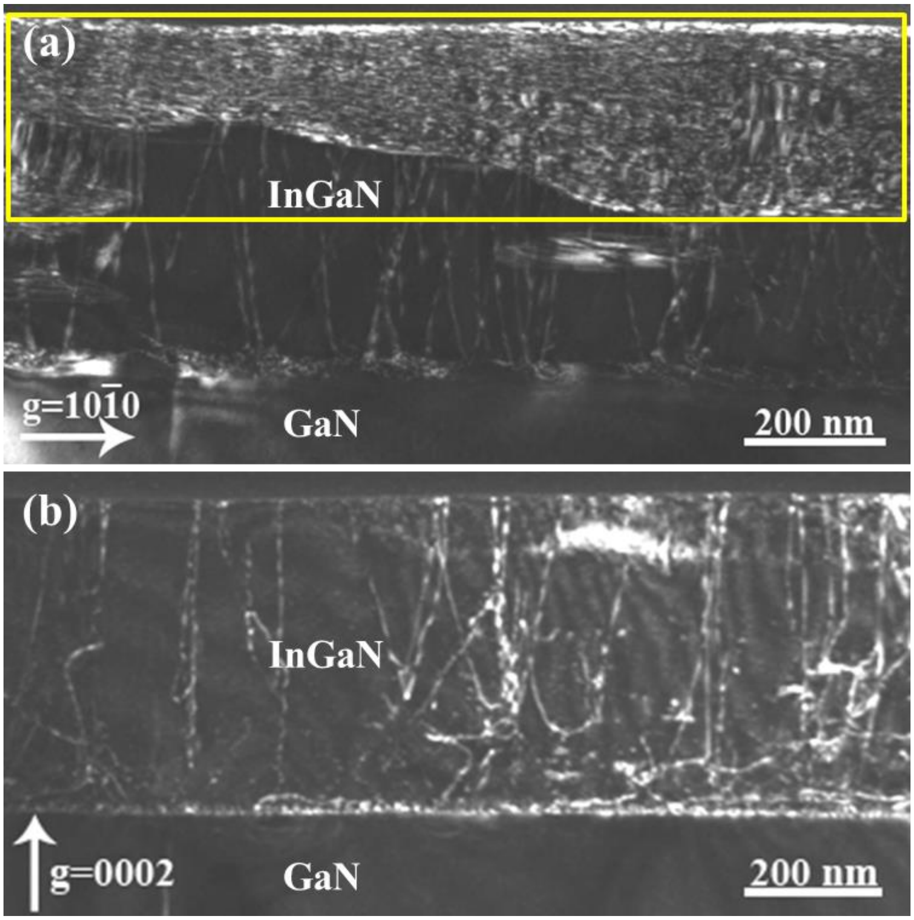

Figure 4.11 Cross-sectional dark field TEM images of E3134 (500 nm) recorded under weak beam conditions with (a) ***g*** = [10-10], and (b) ***g*** = [0002].

From the large extension of the stacking faults areas in sample 3134 as seen in Figure 4.11 (a), the question was to try to determine if any of the known stacking faults of the wurtzite structure could be preferentially formed during this type of growth and be active in the relaxation of the local strain. Therefore, we carried out high resolution TEM observations and as can be seen in Figure 4.12 along with the inserted corresponding Fourier transform, the presume stacking fault area does correspond more to a strong disruption of the stacking sequences along the growth direction, not to the formation of particular stacking faults.

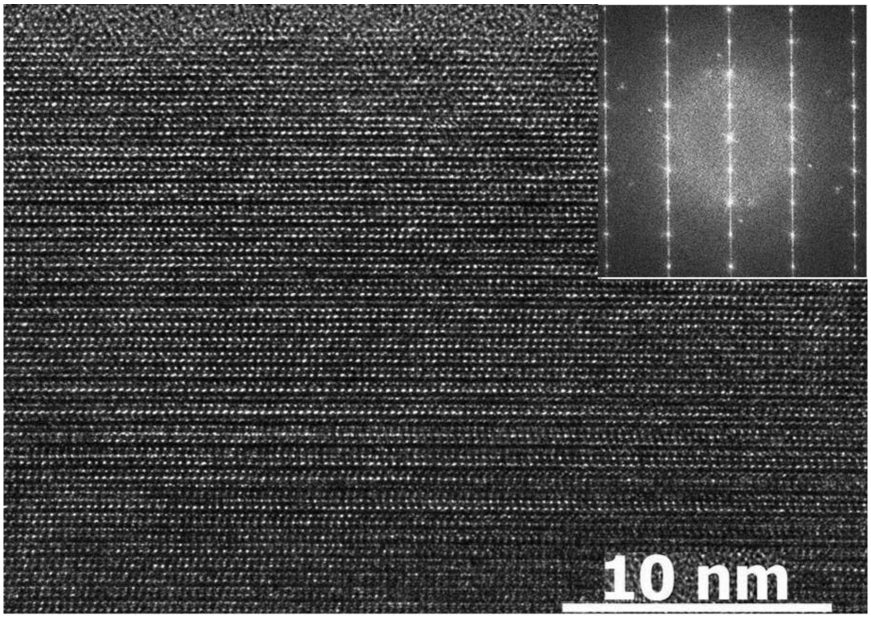

Fig. 4.12 HRTEM micrograph of sample E3134, in the stacking faults area.

4. 5 Discussion and Conclusion

In this chapter, we investigated the InGaN layers with the thickness from 7 nm to 500 nm grown on GaN by PAMBE. Surface morphologies of the InGaN layers were investigated by AFM, we find that the surface morphology and the roughness are slowly evolving versus the layer thickness. At the lowest thickness, the surface morphology consists of step-terrace features, and the surface roughness is quite small ~0.58 nm, quite close to the ***c*** parameter at 0.53 nm for $In_{0.3}Ga_{0.7}N$. When the layer thickness increases to 500 nm, the roughness is limited to ~3.02 nm. Like previous works [6, 7], we further investigated microstructure of the samples by TEM diffraction contrast, the results show that the surfaces of the InGaN layers are all flat, which mean that 2D growth mode of the layers during the growth. In contrast to the above works [6, 7] which focused on the misfit dislocations, this detailed study allows to point out three different and probably complementary processes which are shown to participate in the strain relaxation. They are: (1) the generation of misfit dislocation with ***a*** edge type; (2) a strong disruption of the stacking sequence which is reinforced toward the layer surface at the largest InGaN thicknesses, and (3) the generation of '***a*** + ***c***' dislocation half loops which propagate from the surface to the InGaN/GaN interface. This is rather different than the case of MOVPE where the 3D growth appears to dominate the strain relaxation process at similar intermediate In composition, coming mainly in addition to the formation of the misfit dislocations.

References

[1] L. Hsu, and W. Walukiewicz, J. Appl. Phys. 104, 024507 (2008).

[2] I. Ho, and G. B. Stringfellow, Appl. Phys. Lett. 69, 2701 (1996).

[3] T. Nagatomo, T. Kuboyama, H. Minamino, and O. Omoto, Jpn. J. Appl. Phys. 28, L1334 (1989).

[4] N. Yoshimoto, T. Matsuoka, T. Sasaki, and A. Katsu, Appl. Phys. Lett. 59, 2251 (1991).

[5] Z. Gacevic, V. J. Gomez, N. Garcia Lepetit, P. E. D. Soto Rodriguez, A. Bengoechea, S. Fernandez-Garrido, R. Notzel, and E. Calleja, J. Crystal Growth 364, 123 (2013).

[6] E. Bellet-Amalric, C. Adelmann, E. Sarigiannidou, J. L. Rouvière, G. Feuillet, E. Monroy,

and B. Daudin, J. Appl. Phys. 95, 1127 (2004).

[7] J. Smalc-Koziorowska, C. Bazioti, M. Albrecht, and G. P. Dimitrakopulos, Appl. Phys. Lett. 108, 051901 (2016).

Chapter 5

The interface dislocations in the InGaN/GaN heterostructures

5. 1 Introduction

Theoretical investigations and experimental observations point out that any substantial lattice mismatch between an epitaxial layer and its substrate should be accommodated by plastic deformation via the gliding of misfit dislocations (MDs) beyond a critical thickness (h_c) [1, 2]. However, the wurtzite III-nitride layers grown on (0001) substrates suffer from the lack of primary gliding planes (basal and prismatic) due to the absence of resolved shear stress, and possible plastic strain relation needs to activate secondary glide planes (pyramidal). Although, MDs at the interface have been reported in AlGaN/GaN [3] and InGaN/GaN [4, 5] heterostructures, no unified mechanism for their nature and formation mechanisms has been proposed until now.

The origin of the MDs has been ascribed to internal and external factors such as growth surface steps [6, 7], use of high crystalline quality epitaxial lateral overgrown GaN templates [4] or from pre-existing threading dislocations in the substrate as proposed by Mathews et al. [1, 8-10]. In this case, theoretical models based on force-equilibrium [11] or energy-balance equations [12, 13] account for the formation of MDs via the glide process leading to large values of h_c. However experimental reports show that in InGaN/GaN heterostructures, for In content of 10%, h_c could be around ~10 nm, and should decreases drastically with increasing In content, reaching 4 nm when the indium content is close to 20% [12] which falls in the quantum wells domain. Importantly, in order to release efficiently the lattice strain, the MDs should be of pure edge type, i.e. ***a*** = 1/3 [11-20] with their line along <10-10> directions. However, as seen in chapter 2, the available glide systems should bring '***a* + *c***' mixed type dislocations at the interface, where the ***c*** components could bring additional crystallographic problems such as local tilt and rotation [14].

In this work, we have extensively used plan-view TEM in the heterostructures grown by

MOVPE as well as PAMBE, with a wide range of indium composition and layer thickness, in order to determine the nature and possible formation mechanisms for the misfit dislocations inside the InGaN/GaN interface. It is assumed that this understanding could be critical for the growth of optimized quality layers and fabrication of highest performance devices such as LEDs and LDs.

5. 2 Low misfit (In < 10%)

The analysis of the misfit dislocations was systematically carried out on all the samples during this work. At the lowest indium content C1750 (In = 4.1%), where lattice mismatch is calculated within the Vegard law to 0.4%, almost no defects such as dislocations and basal plane stacking faults were observed. However, starting with C1236 (In = 9.5%) with a lattice mismatch of 1.1%, the plan view image shows the most interesting features, as can be seen in Figure 5.1 (a), which is just a bright field image along the zone axis [0001], the interface exhibits a complex network of dislocations.

Close observation shows that all the straight lines of the dislocations are parallel to the <11-20> directions (see Figure 5.1 (b)). Contrast analysis reveals that these dislocations are ***a*** type screw dislocations. On top of these low density TDs from free standing GaN substrates, it is not clear if extrinsic sources could be present for the emission of such a dense network of interface dislocations.

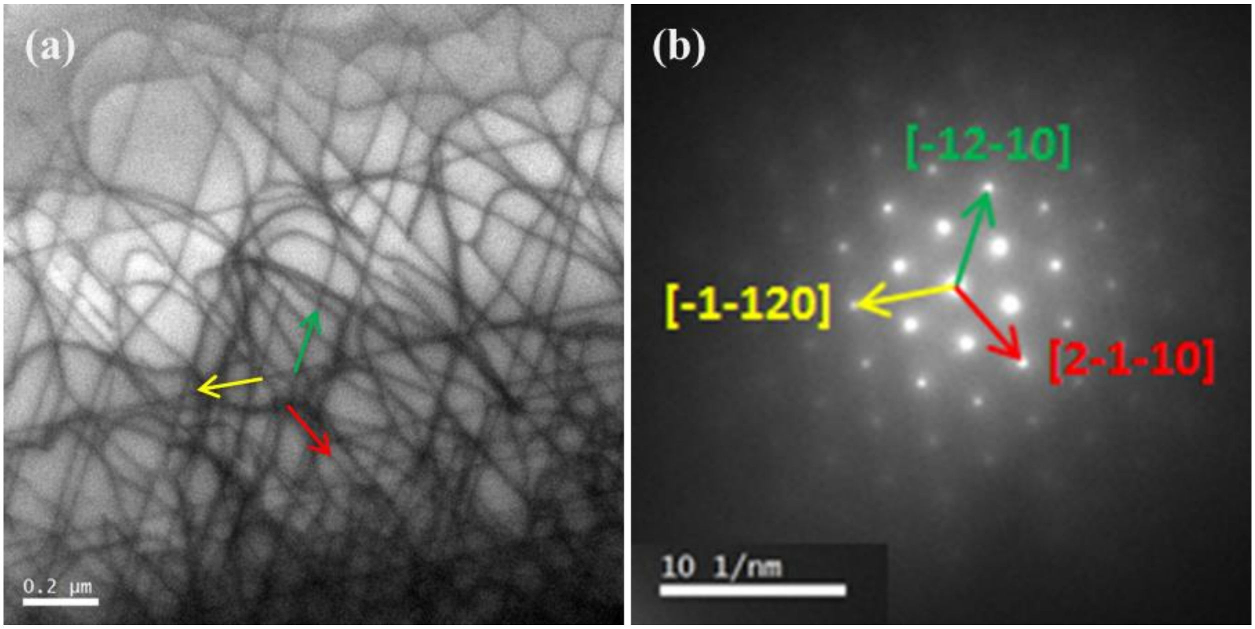

Figure 5.1 (a) The weak beam bright field image of sample C1236 (In = 9.5%), (b) along with the corresponding diffraction pattern where the hexagon basis direction have been marked.

5. 3 Intermediate (In ~ 13%)

In addition to the three sets of screw dislocations as in sample C1236, which are now clearly with their lines along the <11-20> directions, as can be observed in Figure 5.2 (a), a few ***a*** type edge dislocations have their lines along the [0-110] direction (see blue arrows) inside the InGaN/GaN interface in this plan-view image of sample L532. In this instance, the lattice mismatch estimated from the Vegard's law is 1.5% which is slightly more than the 1% in sample C1236 (In = 9.5%) where only screw type dislocations are observed.

The formation of screw dislocations is still prevailing in sample L605 in which the nominal indium composition is 17%, three sets of dislocations are clearly visible in the bright field image (see Figure 5.3 (a)). In this instance the nominal lattice mismatch is just below 2% (1.9%), but only two sets of edge dislocations are visible in this particular area.

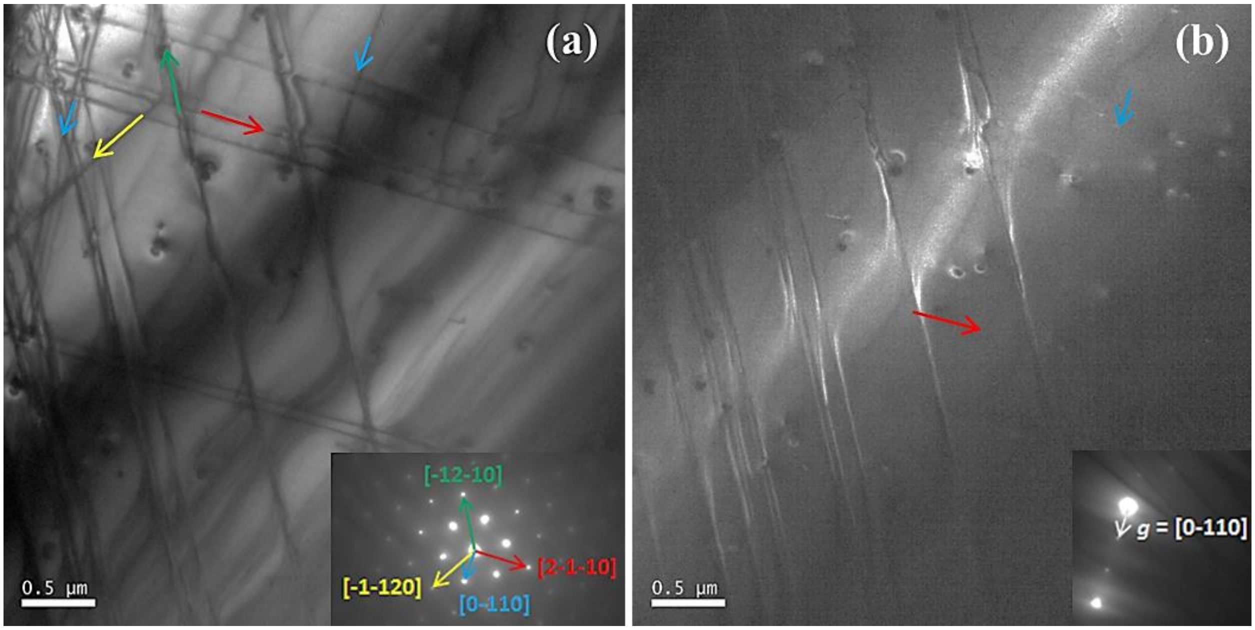

Figure 5.2 Plan-view TEM micrographs of L532 (In = 13%) (a) The weak beam bright field image, with the corresponding diffraction pattern showing the dislocation line directions, (b) the weak beam dark field image with ***g*** = [0-110] with one network of ***a*** screw dislocations visible.

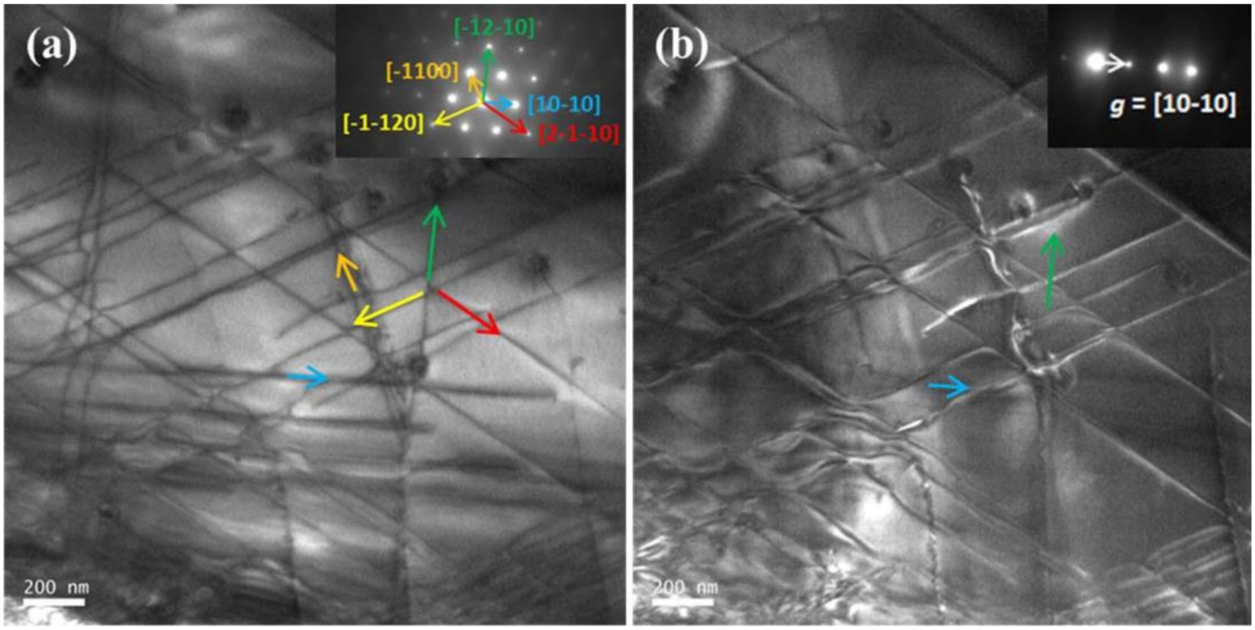

Figure 5.3 Plan-view TEM of sample L605 (In = 17%) (a) The weak beam bright field image, along with the corresponding diffraction pattern, (b) the dark field image with ***g*** = [10-10].

5. 4 Medium misfit (In ≥ 18%)

The configuration of the interfacial dislocation network is completely different in sample L597 where the nominal indium content is 18.1%. As can be seen in Figure 5.4, only a hexagonal network of ***a*** type edge dislocations is now present at the InGaN/GaN interface. The three sets of dislocation lines are along the <10-10> directions as assessed from the inserted [0001] zone axis diffraction pattern as shown in Figure 5.4 (a). The corresponding lattice mismatch is 2.0%. Still, the dislocation network does not show strong periodicity and the inter-dislocations spacing shows variation from 200 nm to 500 nm.

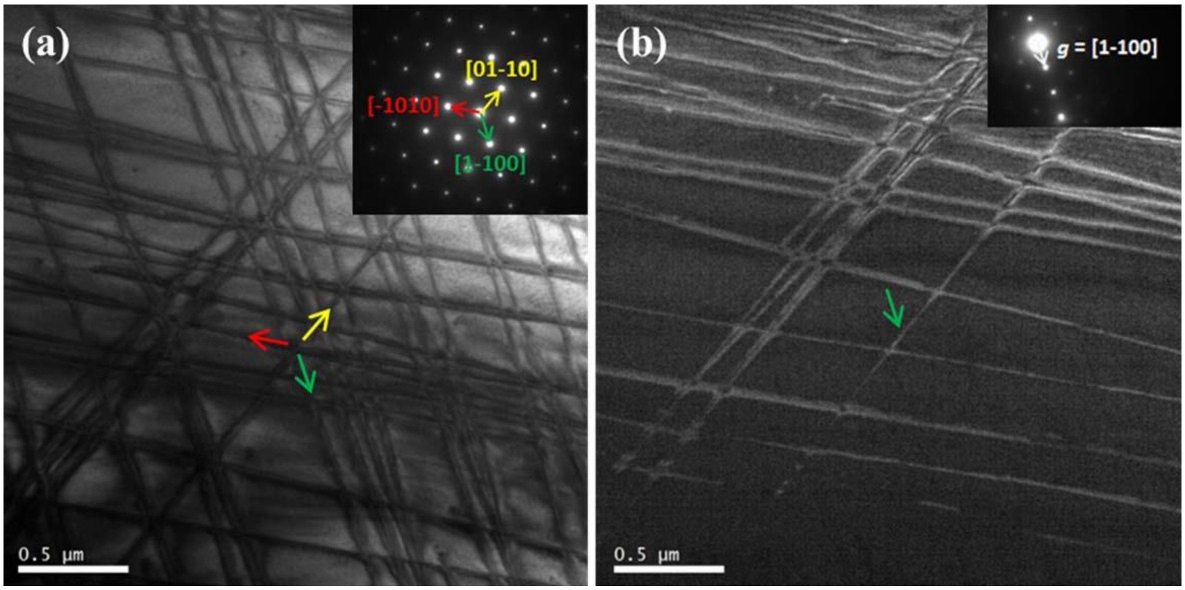

Figure 5.4 Plan-view TEM micrographs of sample L597 (In = 18.1%) (a) The bright field image, with inset the corresponding diffraction pattern along the zone axis [0001], (b) the dark field image with ***g*** = [1-100].

5. 5 High misfit (In ~ 30%)

As seen in chapter 3, when the indium content becomes high, MOVPE grown layers undergo a strong structural degradation. Therefore, in order to attain some understanding on the formation of interface dislocations in high indium content heterostructures, we discuss the results obtained on PAMBE samples where the nominal indium content was intended to be around 30%. As discussed in chapter 4, in these layers, the same structural features become predominant starting at a thickness of 80 nm, this concerns the formation of MDs, dislocation half loops and stacking sequences disruption. However, at 80 nm thickness, the stacking sequences disruption is not yet predominant, therefore, we used this sample to examine the MDs. As can be seen in Figure 5.5, a dense network of MDs lines is present; the dislocation lines extend all over the observed area. As in the MOVPE samples, the line spacing of the dislocations is not periodic, it varies from several tens to several hundreds of nanometers, with an average spacing of 250 nm. As in the sample with indium content above 18%, the three sets of dislocation lines are along the <10-10> directions, therefore, only MDs are present at this interface.

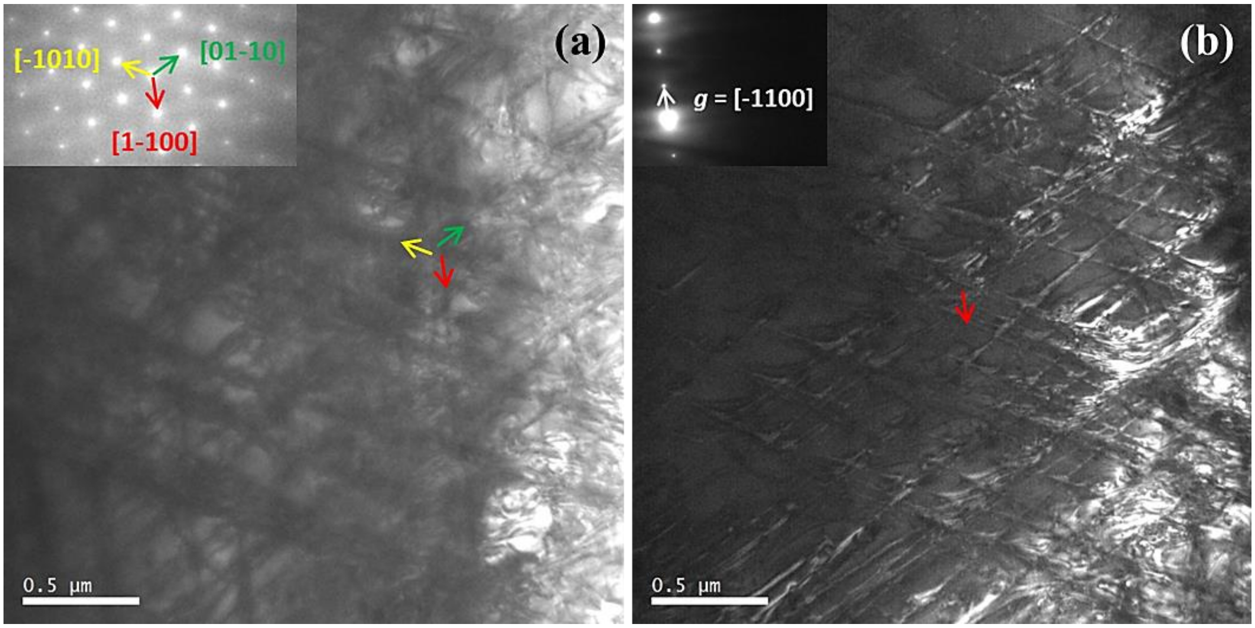

Figure 5.5 Plan-view TEM micrographs of E3136 (80 nm) (a) The bright field image with the corresponding diffraction pattern, (b) the dark field image recorded with ***g*** = [-1100].

5. 6 Discussion

The occurrence of MD is a conventional phenomenon in hetero-epitaxy when the thin layer is growing on a substrate with significantly different lattice parameters. In such cases, below a specific layer thickness, known as the critical thickness, the heteroepitaxial film grows pseudomorphologically on the substrate. Subsequently, the relaxation of the misfit strain takes place for thicker layers ($h > h_c$) and the straightforward mechanism for plastic relaxation is through the formation of MDs. Theoretical models have been reported to calculate the h_c in isotropic materials, and as expected they were shown to reasonably account for the strain relaxation in cubic systems [11, 12]. So far, two reports have been issued for InGaN. Holec et al. [13] took into account the hexagonal symmetry and used the {11-22}<11-23> slip system, their theoretical calculations of h_c within the energy-balance model was reported to give lower values by some 20% than isotropic model. It was possible to agree with their TEM observations where MDs were shown to form starting at an indium concentration of 20% at thicknesses of 3 nm. However, within the error bar of experimental data from X-ray diffraction and ellipsometry, Leyer et al. [15] were able to fit their data on InGaN thin layers using the isotropic model proposed by Fisher et al. [12]. It should be pointed out that the h_c which has been calculated for a particular slip system, {11-22}<11-23> does not take into account other relaxation mechanisms such as formation of threading dislocations, V-shape dislocation half loops or trenches etc. As seen above, we clearly observed '***a* + *c***' half loops dislocation gliding in the pyramidal planes towards the InGaN/GaN interface, especially in our PAMBE layers. Therefore, we also can report our data as shown in Figure 5.6 for a comparison with the different models, in the same Figure, we also show the in-plane strain ε_{xx} along the whole indium concentration (right axis), The TEM measured thicknesses of all our samples ($4.1\% \leq \text{In} \leq 100\%$) are included. As can be clearly seen, apart from sample C1750 which falls quite close to the theoretical curves, all the other should be expected to have undergone a plastic strain relaxation and contain MDs at the interface with GaN.

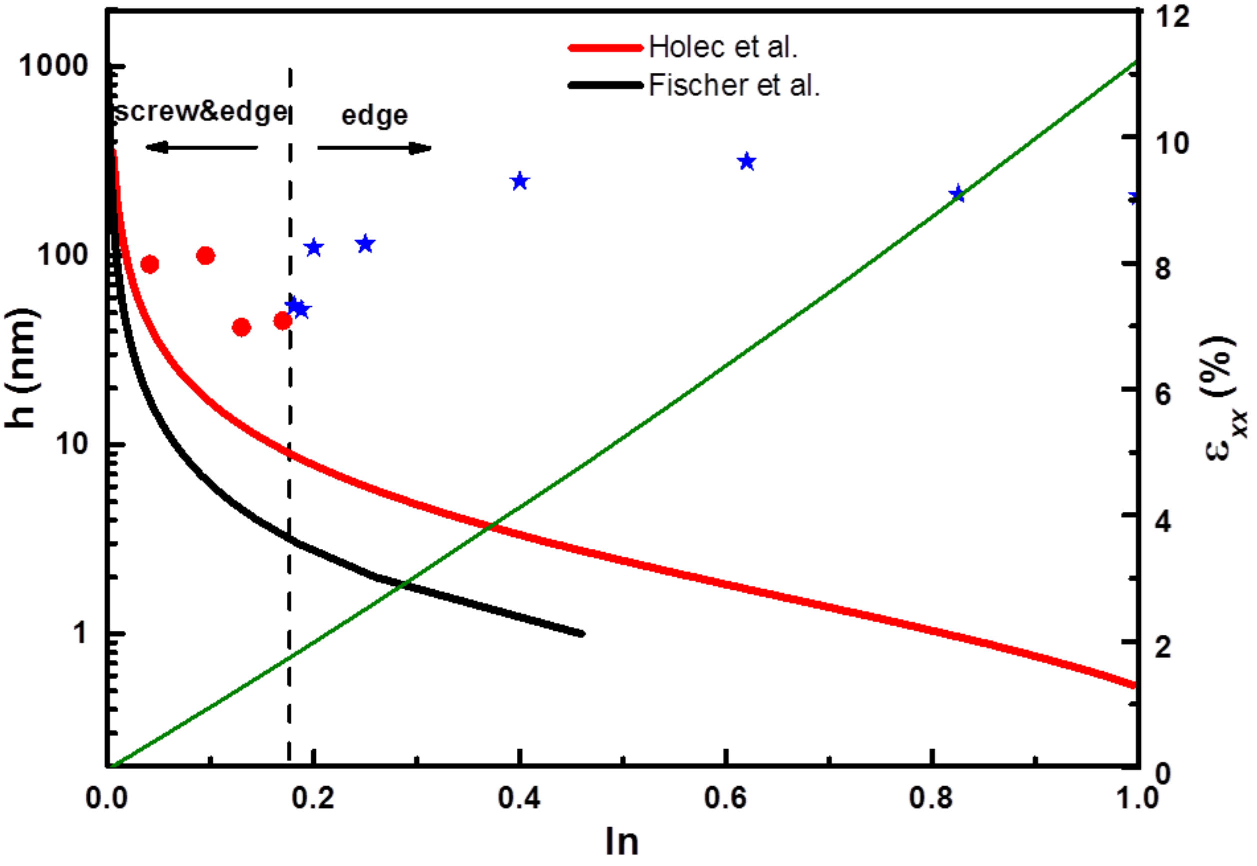

Figure 5.6 Critical thickness of $In_xGa_{1-x}N$ grown on GaN by MOVPE for 4.1% ≤ In ≤ 100%. The continuous lines are calculations of the critical thickness following Fischer et al. [12] (black curve) and Holec et al. [13] (red curve). Red circles represent samples with very few misfit dislocations and blue stars represent samples with high density misfit dislocations. The green curve represents the biaxial strain for a fully strained InGaN layer on GaN.

Early reports in cubic semiconductor alloys have reported that for lattice mismatch of more than 2%, the misfit strain should be relaxed through the formation of pure edge Lomer dislocations, whereas for less than 2%, the 60° MDs which exhibit a screw component would constitute the majority of the dislocations at the interface [16, 17]. For our samples we have used the red circles for the samples with indium composition ≤ 18% and blue stars to those with more than 18%, which is separation point for the presence of screw dislocation at the interface. It may then be concluded that, for InGaN/GaN in wurtzite structure, the ε_{xx} higher than 1.5% is required for the formation of MDs beyond the h_c.

Apart from the glide to the interface through the crystallographic slip system, it is worth to mention another mechanism which was proposed for the formation of MD in InGaN/GaN heterostructures and name as punch-out mechanism of Liu et al. [5]. This was subsequent to the observation of opposite-sense steps at the surface by TEM cross section analysis. As can be seen in the schematic diagram in Figure 5.7 (a) along with the TEM image (see Figure 5.7 (b)), the slip planes {11-22} along <11-23> may also lead to a net displacement of $\boldsymbol{c}$ along [0001] direction and $\boldsymbol{a}$ along <11-20> directions, resulting in a surface step. This mechanism needs to involve a simultaneous slide in $\boldsymbol{a} + \boldsymbol{c} = (1/3)$<11-23> directions on two oppositely inclined planes with a crossing at the interface, moreover, the Burgers vectors of the two gliding dislocations must have opposite $\boldsymbol{c}$-component as illustrated, as a result of the slip, the MD is formed at the interface, and its Burgers vector is of $(\boldsymbol{a} + \boldsymbol{c}) + (\boldsymbol{a} - \boldsymbol{c}) = 2\boldsymbol{a}$.

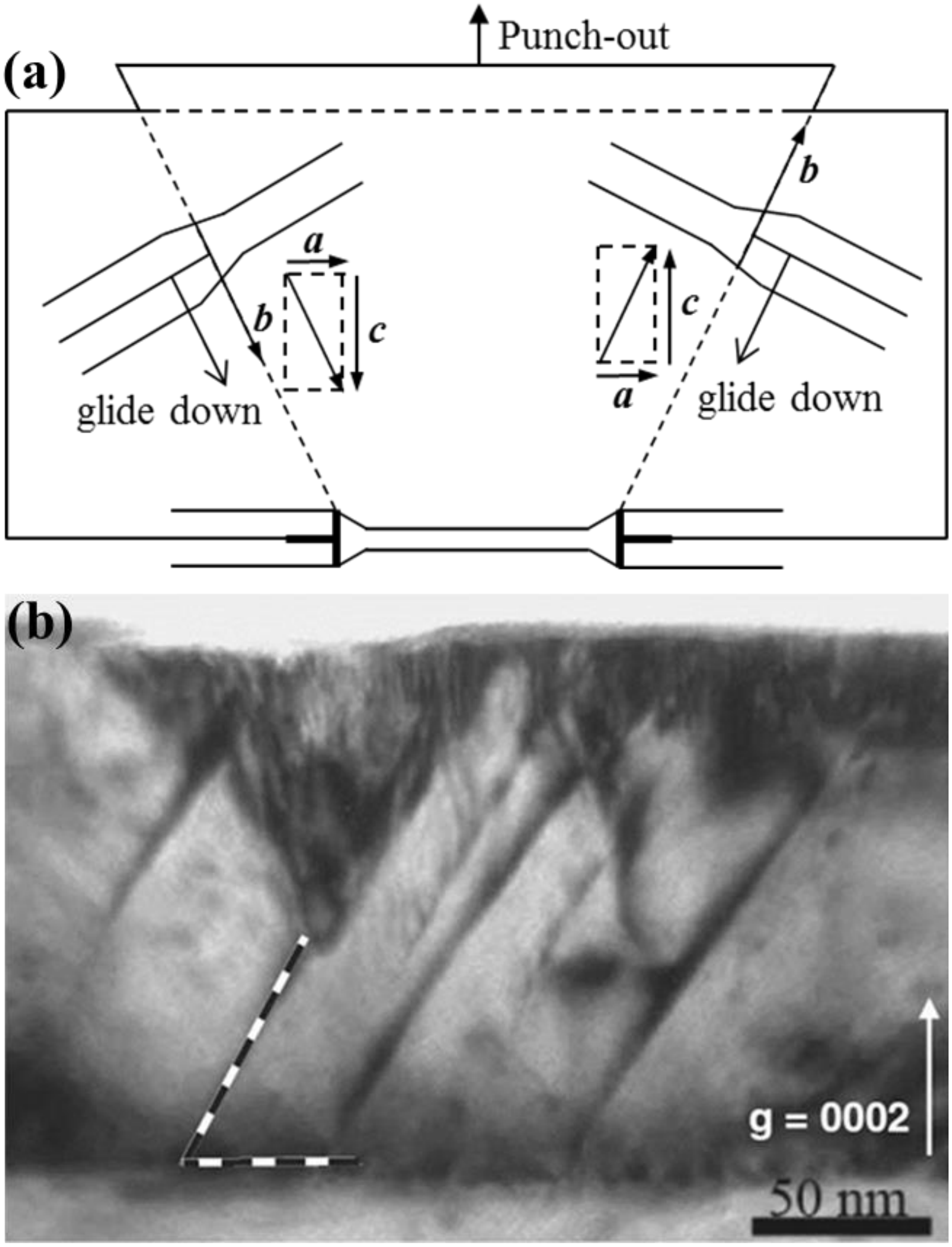

Figure 5.7 (a) Schematic diagram illustrating plastic relaxation via the punch-out relaxation process involving formation of misfit dislocations along two oppositely inclined slip planes which contain Burgers vectors ***a*** ± ***c***, (b) cross section TEM image recorded with ***g*** = [0002] [5].

Whether such a mechanism has been under operation in our samples, our extensive observations have not been able to point it out. For instance in the PAMBE samples where the dislocation half loops were systematically investigated, no similar features as shown in Figure 5.7 have been observed, which is an indication that if present, this behavior was not predominant in our samples.

5. 7 Summary

In particular, the growth along the [0001] direction limits the glide of dislocations on only a few lattice plane families. This work allows showing that the strain relaxation in InGaN/GaN heterostructures also goes through the generation of misfit dislocation at the interface. It is pointed out, that below the in-plane strain of 1.5% (In < 10%), the screw dislocations coexist with the misfit dislocations above the critical thickness. Beyond this strain, only ***a*** type edge dislocations form at the interface, however, their spacing is not regular as often reported in cubic materials, this is probably due to the fact that the strain relaxation in this growth geometry goes through secondary slip system, and as we have seen in the other chapters, additional defects also intervene into the strain relaxation process.

References

[1] J. W. Matthews, and A. E. Blakeslee, J. Cryst. Growth 27, 118 (1974).

[2] J. H. van der Merwe, Surf. Sci. 31, 198 (1972).

[3] J. A. Floro, D. M. Follstaedt, P. Provencio, S. J. Hearne, and S. R. Lee, J. Appl. Phys. 96, 7087 (2004).

[4] S. Srinivasan, L. Geng, R. Liu, F. A. Ponce, Y. Narukawa, and S. Tanaka, Appl. Phys. Lett. 83, 5187 (2003).

[5] R. Liu, J. Mei, S. Srinivasan, H. Omiya, F. A. Ponce, D. Cherns, Y. Narukawa, and T. Mukai,

Jpn. J. Appl. Phys. 45, L549 (2006).

[6] M. Ichimura, and J. Narayan, Mater. Sci. Eng. B 31, 299 (1995).

[7] A. M. Andrews, A. E. Romanov, J. S. Speck, M. Bobeth, and W. Pompe, Appl. Phys. Lett. 77, 3740 (2000).

[8] W. Lü, D. B. Li, C. R. Li, and Z. Zhang, J. Appl. Phys. 96, 5267 (2004).

[9] P. S. Hsu, E. C. Young, A. E. Romanov, K. Fujito, S. P. den Baars, S. Nakamura, and J. S. Speck, Appl. Phys. Lett. 99, 081912 (2011).

[10] M. A. Hossain, M. M. Hasan, and M. R. Islam, Int. J. Appl. Phys. Math. 2, 49 (2012).

[11] R. People, and J. C. Bean, Appl. Phys. Lett. 47, 322 (1985).

[12] A. Fischer, H. Kühne, and H. Richter, Phys. Rev. Lett. 73, 2712 (1994).

[13] D. Holec, P. M. F. J. Costa, M. J. Kappers, and C. J. Humphreys, J. Cryst. Growth 303, 314 (2007).

[14] F. A. Ponce, MRS Bulletin 22, 51 (1997).

[15] M. Leyer, J. Stellmach, C. Meissner, M. Pristovsek, and M. Kneissl, J. Cryst. Growth 310, 4913 (2008).

[16] R. E. Mallard, P. R. Wilshaw, N. J. Mason, P. J. Walker, and G. R. Booker, Inst. Conf. Ser. 100, 331 (1989).

[17] A. Vilà, A. Cornet, J. R. Morante, M. Loubradou, R. Bonnet, Y. González, L. González, and P. Ruterana, Philos. Mag. A. 71, 85 (1995).

Chapter 6

Conclusions and perspectives

Conclusions

The indium composition of the InGaN layers grown by MOVPE from a few percent (4.1%) to pure indium nitride has been studied, the main results of this study are:

(1) When In < 13%, we have observed step-terrace morphology with a very low density of V-pits. For 13% ≤ In ≤ 18.1%, the surface morphology consists of hillocks and V-pits, moreover at around 18%, the surface is covered with hexagonal cross-hatch linear structures.

(2) Above In = 20%, a granular morphology covers the surface. However, for In = 25%, there appears an agglomeration of particle shape at the surface, which means that the growth mode undergoes a clear transition from 2D to 3D, this comes with a sudden increase of the surface roughness.

(3) For the highest In content (In ≥ 40%), XRD analysis shows the largest diffraction peak and TEM observations confirm the 3D growth mode of the InGaN layers with highly deteriorated crystalline quality and even formation of porous structure.

(4) For the PAMBE samples with a nominal indium composition of 30%, it is shown that the increase in thickness plays an important role and the relaxation of the strain evolves with it. Indeed, up to 120 nm thickness, the layer composition fluctuated almost in a random way and the strain relaxation comes through the formation of misfit dislocations by glide of '***a*** + ***c***' half loop dislocations from the surface to the interface. At larger thicknesses, it is shown that high density of threading dislocations are presented inside the layer with Burgers vectors of ***a*** and ***a*** + ***c***, meaning that the maximum of '***a*** + ***c***' half loops has been able to reach the InGaN/GaN interface. Moreover, there is a strong disruption of the hexagonal stacking sequence which settles close to the surface where indium composition pulling takes place.

Perspectives

At the end of this work, many points still require work in order to completely explain our observations towards a better understanding of the growth of InGaN/GaN heterostructures, some of them are listed as follows:

(1) Although, we have been successful to observe the ***a*** type screw dislocations, it is still unclear what can be its formation mechanism. Moreover the transformation of screw dislocations into misfit dislocation needs further investigation to be understood.

(2) The other concern is the stacking sequence disruption with the increase in indium content. It is clear that this effect would need even theoretical investigation in order to provide an explanation.

(3) We have clearly observed the glide of the '***a*** + ***c***' dislocation towards the InGaN/GaN interface towards the formation of the misfit dislocations. In our PAMBE samples, the half loops cannot imply two ***c*** dislocation with opposite sign and the punch-out mechanism as proposed by the Arizona State University cannot be applied in this case. The next step in our samples will be therefore to determine what becomes of the ***c*** component during the formation of the misfit dislocations.

Relaxation des contraintes dans les hétérostuctures InGaN/GaN

Résumé:

Dans ce travail, nous avons étudié la relaxation de couches d'hétérostructures InGaN/GaN obtenue par épitaxie en phase vapeur aux organométalliques (EPVOM) et épitaxie aux jets moléculaires (EJM) principalement par microscopie électronique en transmission (MET). Pour ce faire, nous avons fait varier la composition de l'indium de 4.1% au nitrure d'indium pur, ce qui correspond lors de la croissance sur GaN à un décalage paramétrique allant de 1% à 11.3%. Le travail a porté sur des couches dont l'épaisseur allait de 7 nm à 500 nm. A partir d'une composition en indium voisine de 10%, nous mettons en évidence la formation d'un réseau de dislocations vis dont la ligne se promène dans l'interface, avec de très longues sections droites le long des directions <11-20>. Ces dislocations coexistent avec un réseau de dislocations coins qui commence à se former vers 13%, il disparait complétement autour d'une composition en indium de 18%. Le réseau de dislocation vis se densifie de plus en plus au-delà. Outre ces dislocations de décalage paramétrique, d'autres mécanismes qui contribuent à la relaxation de la contrainte dans ces hétérostructures InGaN/GaN ont été mis en évidence. Ainsi, au-dessus d'une composition d'indium supérieure à 25%, de nombreux phénomènes se produisent simultanément. (1) Formation des dislocations de décalage paramétrique à l'hétérointerface; (2) une composition de la couche qui s'enrichit en indium vers la surface; (3) des fortes perturbations de la séquence hexagonale conduisant à un empilement aléatoire; (4) croissance à trois dimensions (3D) pouvant même conduire à des couches poreuses lorsque la composition en indium est comprise entre 40% et 85%. Cependant, on met en évidence qu'il est possible de faire croître de l'InN pur de bonne qualité cristalline s'améliore grâce à la formation systématique d'une couche 3D.

Mots clés: EPVOM; EJM; MET; InGaN; GaN; dislocations vis; dislocations de décalage paramétrique; relaxation des contraintes; mécanisme de formation; hétéroïnterface.

Strain relaxation in InGaN/GaN heterostuctures

Abstract:

In this work, we have investigated the strain relaxation of InGaN layers grown on GaN templates by MOVPE and PAMBE using TEM. To this end we varied the indium composition from 4.1% to pure indium nitride and the corresponding mismatch was changing from less than 1% to 11.3%, the thickness of the InGaN layers was from 7 nm to 500 nm. When the indium composition is around 10%, one would expect mostly elastically strained layers with no misfit dislocations. However, we found that screw dislocations form systematically at the InGaN/GaN interface. Moreover, below 18% indium composition, screw and edge dislocations coexist, whereas starting at 18%, only edge dislocations were observed in these interfaces. Apart from the edge dislocations (misfit dislocations), other mechanisms have been pointed out for the strain relaxation. It is found that above an indium composition beyond 25%, many phenomena take place simultaneously. (1) Formation of the misfit dislocations at the heterointerface; (2) composition pulling with the surface layer being richer in indium in comparison to the interfacial layer; (3) disruption of the growth sequence through the formation of a random stacking sequence; (4) three dimentional (3D) growth which can even lead to porous layers when the indium composition is between 40% and 85%. However, pure InN is grown, the crystalline quality improves through a systematic formation of a 3D layer.

Key words: MOVPE; PAMBE; TEM; InGaN; GaN; screw dislocations; misfit dislocations; strain relaxation; formation mechanism; heterointerface.